University of California
Santa Barbara

Efficient Field Theoretic Simulations of Branched and Network Polymers

A dissertation submitted in partial satisfaction
of the requirements for the degree

Doctor of Philosophy
in
Chemical Engineering

by

Daniel L. Vigil

Committee in charge:

Professor Glenn H. Fredrickson, Chair
Professor Rachel Segalman
Professor M. Scott Shell
Professor Carlos García-Cervera

June 2022

The Dissertation of Daniel L. Vigil is approved.

DocuSigned by:
Rachel Segalman
42901C0602F34B9...

Professor Rachel Segalman

DocuSigned by:
M. Scott Shell
B63ED449DF9945D...

Professor M. Scott Shell

DocuSigned by:
Carlos Garcia-Cervera
A18619B5D7B747F...

Professor Carlos García-Cervera

DocuSigned by:
Glenn Fredrickson
2F038D1A2AAF440...

Professor Glenn H. Fredrickson, Committee Chair

May 2022

Efficient Field Theoretic Simulations of Branched and Network Polymers

by

Daniel L. Vigil

Acknowledgements

I am deeply indebted to many people, without whom my journey through grad school would not have been possible nor enjoyable. Chief among these are Glenn Fredrickson who has been a patient mentor who has given me great freedom to explore what interests me, even if it may not be "productive". I am also deeply grateful to Kris Delaney who has taught me a lot about scientific computation and software and answered many dumb questions. The other members of my committee have also been great resources, especially regarding career planning, while simultaneously leading their departments through a worldwide pandemic. Additionally, there are many professors to whom I owe thanks for being incredible classroom instructors, including Mike Doherty, Baron Peters, Michael Chabinyc, and Chris Bates. I would also like to thank Chris Bates for being a wonderful collaborator in my years at UCSB. My work would also not have been possible without the support of Paul Weakliem and Fuzzy Rogers who do a splendid job managing the computational resources I used.

I have also had the joy of learning from and also mentoring many other students and postdocs at UCSB. Many current and former members of the Fredrickson group have been instrumental to my thinking and work, including Josh Lequieu, Doug Grzetic, Kevin Shen, Jimmy Liu, Scott Danielsen, Jan García, Carol Tsai, Kimberley Keithley, Tim Quah, Dan Sun, Amy Zhang, Charles Li, Tony Cooper, My Nguyen, Ethan McGarrigle, Doug Tree, Debbie Audus, and Mike Villet. Outside the UCSB campus I have also had the pleasure of interacting with many wonderful people who engage with me in a variety of activities including basketball, hiking, backpacking, fantasy football, poker, and trivia. I am grateful for all of you who gave me these outlets to blow off steam.

Finally I would like to thank my family, including my parents, Susan and Dennis, who have been wonderful caretakers, teachers, and role models for all my life. I am

also thankful for my brother David who has helped me resist my parents best intentions whenever possible. My extended family has also been great support and has encouraged me on every step of my journey to where I am today.

Daniel Vigil

Curriculum Vitæ

Daniel L. Vigil

Education

2022	Ph.D. in Chemical Engineering, *University of California, Santa Barbara.*
2017	B.S. in Chemical Engineering, *University of Wisconsin-Madison*

Research Experience

2022-	Postdoctoral Associate, *Sandia National Laboratories*
2017-2022	Graduate Student Researcher, *University of California, Santa Barbara*
2013-2017	Research Assistant, *University of Wisconsin-Madison*
2015	Research Assistant, *Colorado Center for Biorefining and Bioproducts*
2014	Intern, *Renewable Energy Group*

Awards & Fellowships

2022	Frank J. Padden Jr. Finalist
2017	Eugene Cota-Robles Fellowship
2017	NSF Graduate Research Fellowship
2016	Kowalke-Harr Teamwork Award
2015	Hilldale Research Fellowship
2013	UW-Madison Chancellor's Scholarship

Publications

Daniel L. Vigil, Amy Zhang, Kris T. Delaney, and Glenn H. Fredrickson. Phase separation, reaction equilibrium and self assembly in binary telechelic homopolymer blends. (in preparation)

Daniel L. Vigil, Timothy Quah, Dan Sun, Kris T. Delaney, and Glenn H. Fredrickson. Self-Consistent Field Theory Predicts Universal Phase Behavior for Linear, Comb, and Bottlebrush Diblock Copolymers. *Macromolecules* **2022** (accepted)

Daniel L. Vigil, Kris T. Delaney, and Glenn H. Fredrickson. Quantitative Comparison of Field-Update Algorithms for Polymer SCFT and FTS. *Macromolecules* **2021** *54* (21), 9804-9814

Cheng Zhang, **Daniel L. Vigil**, Dan Sun, Morgan W. Bates, Tessa Loman, Elizabeth A. Murphy, Stephanie M. Barbon, Jung-Ah Song, Beihang Yu, Glenn H. Fredrickson, Andrew K. Whittaker, Craig J. Hawker, and Christopher M. Bates. Emergence of Hexagonally Close-Packed Spheres in Linear Block Copolymer Melts. *Journal of the American Chemical Society* **2021** *143* (35), 14106-14114

Cheng Zhang, Morgan W. Bates, Zhishuai Geng, Adam E. Levi, **Daniel L. Vigil**, Stephanie M. Barbon, Tessa Loman, Kris T. Delaney, Glenn H. Fredrickson, Christopher M. Bates, Andrew K. Whittaker, and Craig J. Hawker. Rapid Generation of Block Copolymer Libraries Using Automated Chromatographic Separation. *Journal of the American Chemical Society* **2020** 142 (21), 9843-9849

Daniel L. Vigil, Carlos J. Garca-Cervera, Kris T. Delaney, and Glenn H. Fredrickson. Linear Scaling Self-Consistent Field Theory with Spectral Contour Accuracy. *ACS Macro Letters* **2019** *8* (11), 1402-1406

Selected Presentations

2022	APS March Meeting, Chicago, IL Padden Award Symposium
2021	AIChE Annual Meeting, Boston, MA
2021	UCSB Graduate Student Symposium, Santa Barbara, CA
2021	Graduate Simulation Seminar Series, Santa Barbara, CA
2021	APS March Meeting, Virtual
2019	APS March Meeting, Boston, MA

Abstract

Efficient Field Theoretic Simulations of Branched and Network Polymers

by

Daniel L. Vigil

I demonstrate how to conduct efficient field theoretic simulations (FTS) and self-consistent field theory (SCFT) calculations for a variety of polymer models, including comb-like and bottlebrush diblock copolymers, binary blends of heterobonding telechelic homopolymers, and end-linking star polymers in solution. I develop field theory models in both the auxiliary field (AF) framework and coherent states (CS) framework, which are well suited to unreactive and reversibly-bonding polymers, respectively. Numerical methods for both types of models are developed and compared for SCFT calculations, and also for FTS of AF models. I demonstrate that depending on whether the system is on average disordered or inhomogeneous affects which choice of algorithm performs best. Additionally, the CS representation can conduct simulations more efficiently than AF for SCFT, but is disadvantaged for FTS.

I apply these numerical methods to study trends in phase behavior of both reactive and unreactive polymers. I examine the effect of architecture, including side-chain length and grafting density, on the stability of Frank-Kasper sphere phases for comb-like and bottlebrush diblock copolymers. I show that the effect of architecture is related to conformational asymmetry in linear polymers, and a universal phase diagram that combines all these effects into a single parameter.

I then shift my focus to reactive polymers, where I use the CS models and algorithms to simultaneously compute phase stability and reaction equilibrium in self-assembled blends of reactive homopolymers. Although these blends produce wide distributions of

products, they can be well approximated with simple blends of unreactive block copolymers and homopolymers. Exotic trends in phase behavior, such as reentrance are also observed, but are explained via the temperature dependence of the reaction equilibrium and phase segregation strength.

Finally, I apply the CS approach to polymer networks formed from star polymers. The mean field analysis of this model is consistent with classical Flory-Stockmayer theory and predicts that spinodal decomposition can only occur after the system has undergone gelation. Including fluctuation effects accounts for loop and ring formation, which is not accounted for in Flory-Stockmayer theory and creates strong corrections to the mean field picture for dilute polymers.

Contents

List of Figures

Chapter 1

Introduction

Polymers are present in a wide array of materials and industries, including in biology via proteins and DNA, in formulated solutions for consumer products, and in melts and blends as plastic components. Due to these varied applications and the multitude of underlying chemistries, the ability to model and predict properties of polymers has become crucial to quick and efficient investigation of polymeric materials. In particular, theoretical models and numerical simulations can allow for much more rapid and cost effective investigation of polymers than is possible experimentally and can also provide mechanistic information not available in experiments. As such, modeling tools have become critical to modern polymer physics.

One important class of models are field-based representations of polymers [1,2]. While it is natural to think of a molecule based on the positions of various atoms, one must then address the immense multi-body physics issue of all the possible interactions between particles. This quickly becomes prohibitive for dense melts of long polymers composed of many monomers. Field based representations take these particle based models and decouple all the multi-body physics from different molecules and introduce auxiliary fields defined over all of space to mediate these interactions [1]. One then only has to evaluate

how an individual molecule interacts with the field. Such an approach may be familiar from the study of electrostatics and magnetism, where a charge interacts with the electric field created by all the other charges in the system.

Although these Auxiliary Field (AF) models have removed the many-body problem associated with the different molecules in a system, they are typically still too complicated to evaluate exactly. Historically they have been evaluated using approximate analytical techniques to make predictions about the excluded volume effect [3] and critical phenomenon [4]. In recent years these approximations, have been relaxed as numerical interrogation of the theories is tractable. This has spawned an entire approach known at Field Theoretic Simulation (FTS), wherein particle models are converted to a field representation then subjected to numerical discretization schemes [1]. There are some mathematically subtleties present that put restrictions on which particle models can be transformed to the field representations, however. Nonetheless, these restrictions are well documented and understood [5–7]. Within these restrictions, it has been shown that FTS can be used to efficiently model a wide variety of polymer phenomenon, including nematic ordering [8], phase separation and self assembly [9], and polyelectrolyte complexation [10].

One strength of FTS is that the resolution of the calculation can be adjusted at will based on the length scale of interest. One such area is self-assembly where many molecules coordinate into patterns with length scales much greater than that of the individual molecules. Another property of FTS, is that for very long polymers or very concentrated systems, each polymer interacts with many other molecules, leading to each molecule experiencing a highly averaged field over all possible states. In such systems a mean field approximation becomes highly accurate. When such a mean field approximation is applied to FTS it is referred to as self-consistent field theory (SCFT) [11,12]. The simulation is reduced to finding the mean-field state that is consistent with the distribu-

tion of polymers where each molecule experiences the same average field. This approach has found particular success for melts of block copolymers that self assemble into various patterns.

For both FTS and SCFT, a wide array of numerical methods have been developed to conduct efficient simulations [7, 13–26]. Notably, most SCFT and FTS approaches make use of spectral approximations to the spatial domain to make accurate numerical approximations to the full theory. In particular, the community has settled on a pseudo spectral approximation with periodic boundary conditions to represent bulk phases [1]. The other important numerical decision for FTS and SCFT is how to iterate the simulation. For SCFT the task is to identify the mean field configuration as quickly and cheaply as possible. The problem can be posed as either a root-finding task or an optimization problem, which lead to different numerical algorithms [1,13,17,18]. While both approaches have their own merits, they have not been compared quantitatively, leading to some ambiguity on when to use which approach. In chapter 2 we help address this uncertainty by comparing both approaches, as well as an array of individual algorithm choices, when applied to a model system of a linear diblock melt. We are able to clearly delineate the strength and weaknesses of each approach and demonstrate how to properly calibrate each algorithm.

For FTS, the task is quite different. Rather than search for a single state, the object is to importance sample a distribution of states, consistent with the probability associated with each, then compute average properties about the system. Monte Carlo algorithms are a conventional approach for this task and have been quite successful for particle simulations [27]. Unfortunately, field based models are complex valued and suffer from the sign problem when MC approaches are used [1]. An alternative approach is to use Langevin dynamics to importance sample the system, either with approximations to yield a real-valued model [28], or with fully complex valued Langevin dynamics (CL) [29,30]. In

this work we will focus on the latter as it has been validated over a larger class of models [26]. A number of different algorithms have been developed to perform CL simulations, both in the context of polymers and other applications [21,31,32]. Often these algorithms were tested on simple model systems that are homogeneous on average, however. In chapter 2 we also evaluate an array of algorithms for CL simulations when applied to an inhomogeneous three dimensional simulation of a diblock copolymer. We are able to show that depending on the system of study and the availability of accurate linear response information, different algorithms perform best. Another critical issue for FTS simulations, especially in ordered systems is the limit of stability of the algorithms. We introduce an adaptive time stepping algorithm to polymer simulations which dramatically increases the stability of the method. Finally, we comment on some unresolved challenges with FTS, including unphysical saddle points which can bias results.

The model considered in chapter 2 of a linear AB diblock has been an important platform for theoretical investigation due to it's simplicity, but has already been significantly studied. There are a wide variety of other architectures, however, that are poorly studied by comparison that exhibit novel behavior [33–35]. Examples of novel architectures include comb and bottlebrush polymers which consistent of a backbone with many side chains grafted onto it. It has been shown that these polymers can form domains with large size [36, 37] compared to linear chains and also self assemble into exotic structures, including Frank-Kasper sphere packings [38]. These exotic phases have also been found in linear AB diblocks by carefully selecting the chemistry to create conformational asymmetry [39], where one block wants to form a much tighter coil compared to the other. There have been theoretical studies that attempt to map the idea of conformational asymmetry to the architecture variations of branched polymers and are able to collapse the behavior of the polymers using approximate analytical techniques [40, 41]. In chapter 3, we carry these ideas forward and perform full numerical SCFT calculations using the algorithms

from chapter 2 to study linear, comb-like, and bottlebrush self assembly and the effect of architecture and conformational asymmetry. We show that the theoretical relations still hold and a universal phase diagram can be plotted. Unfortunately, however, we show that SCFT is not able to capture bottlebrush polymers due to computational limits on polymer length.

Chapters 2 and 3 demonstrate how to efficiently apply SCFT and FTS to an AF model to obtain physical insights. While this approach works well for polymers with finite length and simple topology, it cannot be extended to another class of polymers: reactive polymers. In the AF approach one must enumerate the interactions of each type of molecule present in the system with the fields [1]. This makes it efficient for dense systems with many identical models, but for wide distributions of molecules that are produced in reactive polymers systems this task becomes intractable. Fortunately, recent theoretical developments have enabled a theory that is mathematically equivalent to AF models but is more tractable theoretically and numerically for reactive systems where bonds can form reversibly [42, 43]. These Coherent States (CS) theories invoke creation and annihilation operators to build up all the possible products in a polymer assembly with reversible reactions, rather than trying to explicitly enumerate all the products. While there has been some preliminary work to validate these models and explore their applications [42], there has been little other work with them.

The remainder of this work is devoted to developing CS theories into full numerical tools and using them to explore two model systems. In chapter 4 we develop numerical methods for the CS theories at the SCFT level and benchmark them against the previously described approaches from chapter 2. We show that these new models can be evaluated more much quickly and efficiently than the AF approach, in part due to more efficient representation of polymer chains in the CS version. We again use the standard linear AB diblock model to compare algorithms.

In chapter 5 we then apply the algorithm to a binary blend of telechelic polymers. This system is able to self-assemble, phase separate, and form arbitrarily long linear polymers. This combination of phenomenon has previously been intractable to full numerical simulation in the AF approach [44]. The telechelic model also serves as a simplified model of thermoplastic polyurethanes (TPUs) which are a large industrially segment with a variety of applications, from abrasion resistant coatings to medical devices [45]. TPUs are formed from diisocyanates and diol molecules which reflect the terminal bifunctional motif of telechelics. They are also able to undergo reversible bond dissociation analogous to the telechelic model considered here [46–48]. Using the CS telechelic model, we are able to build full phase diagrams, examine the reaction equilibrium and distribution of products, and examine the structure of self assembled phases. We show strongly varying behavior depending on the relative strength of bond formation and chemical incompatibility, and explain the underlying mechanism based on interplay between these thermodynamic factors. Although this system showcases a wide variety of phenomena, it can only form linear reaction products and is unable to percolate into a network and undergo gelation.

As a final task we study a network-forming system in chapter 6. We consider star homopolymers in solution that are able to link at their ends and form networks. There are numerous experimental examples of this system, frequently in hydrogels [49]. Although a mean field picture of gelation due to Flory and Stockmayer has been well known for decades [50, 51], this mean field picture has a number of unrealistic assumptions. Chief among these is that loop and ring like structures are completely neglected, and only hyper-branched molecules are possible. This is a quite unphysical picture of gels, however, as hyper-branched molecules cannot become macroscopic in size unlike real gels. Additionally, gelation and phase separation can often occur simultaneously which leads to confusion on whether they are related [52]. This problem is exacerbated with irre-

versible reactions as equilibrium is often inaccessible. Our models on the other hand are completely equilibrium and are not limited by transient phenomenon so we can exactly determine the underlying equilibrium behavior. We use them to explore the relationship between gelation and phase separation at both the mean field level and also with fluctuations. We leave to future work the inclusion of dynamical phenomena to build upon this equilibrium picture [53].

1.1 Permissions and Attributions

Parts of this dissertation are reproduced and adapted in part or in full with permission from:

1. Daniel L. Vigil, Carlos J. Garca-Cervera, Kris T. Delaney, and Glenn H. Fredrickson. Linear Scaling Self-Consistent Field Theory with Spectral Contour Accuracy. *ACS Macro Letters* **2019** *8* (11), 1402-1406

2. Daniel L. Vigil, Kris T. Delaney, and Glenn H. Fredrickson. Quantitative Comparison of Field-Update Algorithms for Polymer SCFT and FTS. *Macromolecules* **2021** *54* (21), 9804-9814

3. Daniel L. Vigil, Timothy Quah, Dan Sun, Kris T. Delaney, and Glenn H. Fredrickson. Self-Consistent Field Theory Predicts Universal Phase Behavior for Linear, Comb, and Bottlebrush Diblock Copolymers. *Macromolecules* **2022** (accepted)

4. Daniel L. Vigil, Amy Zhang, Kris T. Delaney, and Glenn H. Fredrickson. Phase separation, reaction equilibrium and self assembly in binary telechelic homopolymer blends. (in preparation)

Chapter 2

Field Update Algorithms for Polymer SCFT and FTS

2.1 Introduction

Field theory has been a prominent tool in polymer physics for the last fifty years. Pioneering work by Edwards, de Gennes, Leibler and many others used analytical approximations to understand critical phenomena [54], phase separation [4], and more [3, 55]. In the last thirty years numerical treatment of field theories has become possible, which has allowed the relaxation of approximations such as strong or weak segregation used in earlier work. Numerical solutions of self-consistent field theory (SCFT), which is a mean-field approximation to the full field theory, are now routine and have enabled simulation of full phase diagrams for broad classes of block copolymers and polymer blends [1, 56–58]. It is also possible to conduct simulations of the exact field theory without the mean-field approximation in so-called "Field Theoretic Simulations" (FTS) [1, 16, 59]. FTS has enabled study of phenomena not accessible to SCFT, such as fluctuation-corrected phase diagrams in neat and salt-doped diblock melts [9, 60, 61], polyelectrolyte complex-

ation [10,62,63], nematic ordering [8], ternary microemulsions [64–66], and novel "bricks & mortar" emulsion phases [67].

There are multiple equivalent formalisms that can be used to construct a field theory for an assembly of polymers, but the most mature and numerically tractable is the so-called Auxiliary Field (AF) framework, which decouples pairwise non-bonded interactions between chain segments via a set of fields. There are then two primary tasks in evaluating an AF theory: 1) computing the single-molecule partition functions with fixed field configurations; and 2) generating new realizations of the fields. For polymer models the first task is non-trivial due to the correlations between different segments on the backbone. Previous authors have written about how to evaluate single-polymer partition functions accurately and efficiently, and we refer readers to those works [14,15,19,20,25]. In this work we focus on the task of generating new iterations of a field. In SCFT the goal is to identify saddle-point field configurations that represent the most-probable state at equilibrium. Mathematically, the saddle-point nature of this configuration can be stated as:

$$\left.\frac{\delta H[w]}{\delta w(\boldsymbol{r})}\right|_{w=w^*} = 0 \tag{2.1}$$

Here H is the effective Hamiltonian of the field theory, w is an auxiliary field, and w^* is the saddle-point configuration. The task of generating new fields then reduces to searching for the saddle-point most quickly from a given initial guess. There are multiple approaches to solving the SCFT saddle-point equations (eq 2.1). The first treats the task as a non-linear root-finding problem and historically used quasi-Newton approaches to find the saddle-point [68]. More recently the task has been posed as a fixed-point problem, which has led to Anderson mixing (AM) and other "Jacobian-free" approaches that require significantly less memory than quasi-Newton type methods [18,22,24,69].

An alternative approach involves a fictitious dynamics with the saddle-point configu-

ration as a fixed point. The dynamical system is then evolved in fictitious time until the fixed point is reached. Mathematically this can be expressed as

$$\frac{\partial w(\boldsymbol{r},t)}{\partial t} = -\frac{\delta H[w]}{\delta w(\boldsymbol{r})} \tag{2.2}$$

where H and $w(\boldsymbol{r})$ are generally complex, corresponding to a gradient descent towards saddle points in the complex plane. This approach allows the use of a wide variety of algorithms developed for solving differential equations, a number of which are described in the Methods section. Our first goal in this paper is to compare the various algorithms available for SCFT to determine which algorithms perform best and under what conditions.

There is a significant amount of work in the literature comparing numerical methods for SCFT, but these largely focus on algorithms for computing single-chain partition functions and chain propagators. In particular, many debate the relative merits of spectral and pseudospectral approximations [19, 22–25]. With few exceptions [70], the polymer SCFT community has largely settled on using pseudospectral methods, which we adopt in this work. There are few direct comparisons of different field-update methods, and those that do only consider a small subset of algorithms [17,18]. In this work we consider seven different algorithms for conducting SCFT field updates and provide the first direct comparison of the AM algorithm with fictitious dynamics algorithms. Additionally, we demonstrate how to calibrate each algorithm to obtain optimal performance and provide some heuristics for choosing numerical parameters.

For a fully fluctuating FTS, the goal of generating new field iterations is quite different. Instead of searching for saddle-point field configurations, the goal is to generate a sequence of decorrelated field configurations that allow for importance sampling of average field operators that describe physical properties of the system. Examples of impor-

tant operators are the chemical potential and pressure. Because field theories are usually complex-valued, the averaging process can suffer from a "sign-problem" where a phase present in the complex statistical weight that is extensive with system size produces wild oscillations and leads to difficult averaging when attempting to use conventional methods such as Monte Carlo sampling.

One approach to overcome the sign-problem is a partial-saddle-point approximation that renders the Hamiltonian purely real, enabling traditional Monte Carlo and real Langevin simulations [64, 71–74]. This approach has been successful for studying fluctuations in AB-type polymer systems, including microemulsions of diblock-homopolymer ternary blends and shifts in the order-disorder transition [61, 64–66]. It is not clear how to extend the approach to multicomponent and multispecies systems, however.

A more general approach to overcome the sign-problem is the complex Langevin (CL) method, which has been used in single-component systems, binary, ternary and quarternary mixtures [8, 26]. Because of its broader applicability, we focus solely on the CL method in this work. For CL simulations, the sampling scheme follows the dynamical equation

$$\frac{\partial w(\boldsymbol{r},t)}{\partial t} = -\frac{\delta H[w]}{\delta w(\boldsymbol{r})} + \eta(\boldsymbol{r},t) \tag{2.3}$$

where $\eta(\boldsymbol{r},t)$ is a real-valued Brownian random force. This equation is nearly identical to eq 2.2, only differing by the addition of Brownian noise. However, eq 2.3 is not a conventional "real" Langevin dynamics since $H[w]$ is complex, leading to field trajectories $w(\boldsymbol{r},t)$ that are not restricted to real values. Nonetheless, the similarities between eqns 2.2 and 2.3 imply that SCFT algorithms relying on fictitious-time relaxation can be readily adapted to CL. The complex Langevin approach also permits use of various algorithms from the stochastic differential equation literature. Our second goal in this paper is to compare algorithms for CL simulations and determine which perform best in terms of

stability and efficiency.

There are multiple previous works that compared different algorithms for CL simulations [7, 21, 25, 26]. Unfortunately, these works were limited to either a subset of algorithms [21, 25], models with no microphase self-assembly [7], or small parameter ranges [26]. In this work we consider eight different algorithms for CL simulations, including adaptive time steppers that have not been used previously in polymer systems. We show that these adaptive time steppers significantly improve stability in inhomogeneous systems, especially at strong segregation and low polymer densities. These advances allow CL simulations at conditions that were intractable with previous algorithms. Finally, we explain the mechanism by which algorithms become unstable in CL and how adaptive time stepping avoids failure.

2.2 Theory

We use an AB diblock copolymer melt in the canonical ensemble as a test system for this study. We treat the diblocks as continuous Gaussian chains with segment mass distributed over a Gaussian packet [6] to regularize the field theory, and include both A-B segmental interactions and a Helfand compressibility penalty in the model. The model

equations for this system are [9]

$$Z(n,V,T) = Z_0 \int \mathcal{D}w_+ \int \mathcal{D}w_- \, \exp(-H[w_+,w_-]) \tag{2.4}$$

$$\begin{aligned} H[w_+,w_-] = {} & \frac{C}{\chi N}\int d\boldsymbol{r}\,(w_-(\boldsymbol{r}))^2 + \frac{C}{\chi N + 2\zeta N}\int d\boldsymbol{r}\,(w_+(\boldsymbol{r}))^2 \\ & - \frac{2iC\zeta N}{\chi N + 2\zeta N}\int d\boldsymbol{r}\, w_+(\boldsymbol{r}) - C\bar{V}\ln(Q[w_+,w_-]) \end{aligned} \tag{2.5}$$

$$Q[w_+,w_-] = \frac{1}{\bar{V}}\int d\boldsymbol{r}\, q(\boldsymbol{r},1) \tag{2.6}$$

$$q(\boldsymbol{r},0) = 1 \tag{2.7}$$

$$\partial_s q(\boldsymbol{r},s) = \nabla^2 q(\boldsymbol{r},s) - w(\boldsymbol{r},s)q(\boldsymbol{r},s) \tag{2.8}$$

$$w(\boldsymbol{r},s) = \begin{cases} \Gamma * (iw_+(\boldsymbol{r}) - w_-(\boldsymbol{r})) & s \in (0,f] \\ \Gamma * (iw_+(\boldsymbol{r}) + w_-(\boldsymbol{r})) & s \in (f,1] \end{cases} \tag{2.9}$$

$$\Gamma * w(\boldsymbol{r}) = \frac{1}{(2\pi a^2)^{3/2}}\int d\boldsymbol{r}' \exp\left(-\frac{1}{2a^2}|\boldsymbol{r}-\boldsymbol{r}'|^2\right) w(\boldsymbol{r}') \tag{2.10}$$

Here χ is the Flory interaction parameter, ζ is the Helfand compressibility parameter, N is the polymer contour length, f is the volume fraction of species A, $C = nR_g^3/V$ is the dimensionless chain density, with n the number of polymers and V the volume of the box, and Z_0 is a reference partition function containing ideal-gas contributions and normalizing denominators. $Q[w_+,w_-]$ represents the partition function for a single polymer chain interacting with the fields w_+ and w_- and is computed from the propagator $q(\boldsymbol{r},s)$, which represents the field-based random walk statistics of the polymer starting from a free end. For all calculations we set $f = 0.34$ unless otherwise specified. In this model, the monomer density has been smeared with a Gaussian kernel, Γ, with a range a. All lengths have been non-dimensionalized in units of the unperturbed polymer radius of gyration $R_g = b(N/6)^{1/2}$ and the contour variable $s \in [0,1]$ has been scaled by $1/N$. All spatial integrals are over the scaled volume $\bar{V} = V/R_g^3$.

For SCFT calculations we assume that the melt is incompressible, $\zeta N \to \infty$, and that the density is unsmeared $a = 0$. The incompressible, unsmeared version of the model displays pathological ultraviolet divergences that make the model undefined when conducting fully fluctuating CL simulations [5, 7]. These pathologies can be removed by using finite values for both ζN and a in CL simulations. Unless otherwise specified, we set $\zeta N = 100$ and $a = 0.2\, R_g$ for CL calculations. All calculations are conducted in a fixed-size cubic box with periodic boundary conditions.

For SCFT calculations, the free energy is equal to the effective Hamiltonian, H, and must be purely real valued. This implies that $w_+(\boldsymbol{r})$ must be purely *imaginary* at the saddle-point, despite the fact that the functional integral is over real-valued functions. The argument of the functional integral is analytic, which allows the path of integration to be deformed off the real axis to include the purely imaginary saddle-point [1]. For fluctuating CL simulations this is accomplished automatically via the complexification of the fields. Nevertheless, for SCFT calculations it is convenient to absorb a factor of i into $w_+(\boldsymbol{r})$ and constrain the search path to purely imaginary fields to render the effective Hamiltonian purely real throughout the search space. Such a change of variables constitutes a so-called "Wick rotation".

2.3 Numerical methods

Pseudospectral numerical methods for computing the propagator, $q(\boldsymbol{r}, s)$, have been explored elsewhere [14, 15, 19, 20, 25]. Based on these results, for SCFT calculations we use the RQM4 algorithm with a contour step of $\Delta s = 0.01$ [20]. For CL calculations we use the RK2 algorithm with $\Delta s = 0.01$ [14, 15]. The overall evaluation of the force $G(\boldsymbol{r}; [w]) = -\delta H / \delta w(\boldsymbol{r})$ requires evaluating both the forward and reverse propagators, and evaluating such objects has a computational cost that scales like $\mathcal{O}(N_s M \ln(M))$,

where $N_s = 1/\Delta s$ is the number of contour samples along the polymer backbone, and M is the number of sample points in space. A single field has M elements and typically requires $\mathcal{O}(M)$ operations to update, so for each field configuration generated during the simulation, evaluating the force is significantly more expensive than updating the fields and usually represents the majority of computation time in SCFT and FTS. Minimizing the number of field updates and force evaluations is thus critical to reducing computation time. All SCFT calculations were conducted in a box of size $L_x = L_y = L_z = 9\,R_g$ with $M = 64^3$ sample points, while CL calculations used the same size box with $M = 48^3$, unless otherwise specified.

For field-update schemes, we first briefly review the Anderson mixing algorithm. Anderson mixing is typically used for fixed-point-iteration type problems of the form $w(\boldsymbol{r}) = E(w(\boldsymbol{r}))$, where E is a nonlinear function. The deviation of a particular value of $w(\boldsymbol{r})$ is defined by $d(\boldsymbol{r}) = E(w(\boldsymbol{r})) - w(\boldsymbol{r})$. If one has already iterated through a number, n_h, of fields $w_i(\boldsymbol{r}), w_{i-1}(\boldsymbol{r}), \ldots, w_{i-n_h}(\boldsymbol{r})$ then one can compute an optimized guess for the next iteration, $w_{i+1}(\boldsymbol{r})$, by finding coefficients $\alpha_i, \ldots, \alpha_{i-n_h}$ that minimize $\int d\boldsymbol{r}\, \left(\sum_{j=i-n_h}^{i} \alpha_j d_j(\boldsymbol{r})\right)^2$ subject to the constraint $\sum_{j=i-n_h}^{i} \alpha_j = 1$. Determining these coefficients is a linear optimization problem that requires at least $\mathcal{O}(n_h^2 M)$ operations. Details on efficient implementation of the AM algorithm and initialization strategies can be found elsewhere [18, 22].

The fictitious dynamics algorithms attempt to solve the partial differential equation

$$\partial_t w(\boldsymbol{r}, t) = -\frac{\delta H}{\delta w(\boldsymbol{r})} + \eta(\boldsymbol{r}, t) = G(\boldsymbol{r}; [w]) + \eta(\boldsymbol{r}, t) \tag{2.11}$$

where for SCFT $\eta = 0$, and for CL η is the Brownian force. From here on we refer to the deterministic term $G(\boldsymbol{r}; [w]) = -\delta H/\delta w(\boldsymbol{r})$ as the "force" on a field, w. The simplest

approximation to solve eq 2.11 is the Euler-Maruyama (EM1) approximation

$$w^{j+1}(\boldsymbol{r}) - w^{j}(\boldsymbol{r}) = \Delta t\, G(\boldsymbol{r}; [w^{j}]) + R^{j}(\boldsymbol{r}) \tag{2.12}$$

Here the superscript j represents a discrete-time index and R^{j} is a random variable with zero mean and variance $\langle R^{j}(\boldsymbol{r}) R^{k}(\boldsymbol{r}')\rangle = 2\Delta t\, \delta_{jk}\delta(\boldsymbol{r} - \boldsymbol{r}')$. We continue to use this definition for $R^{j}(\boldsymbol{r})$ when describing other algorithms, unless otherwise specified. Any noise distribution with these first two moments can be used, however we exclusively use normally distributed noise in this work. Although simple to implement, the EM1 algorithm has poor stability and accuracy compared to other algorithms.

Another class of algorithms splits the force into a linear and a non-linear contribution

$$-\frac{\delta H}{\delta w(\boldsymbol{r})} = G(\boldsymbol{r}; [w]) = -c * w(\boldsymbol{r}) + F(\boldsymbol{r}; [w]) \tag{2.13}$$

where $c * w$ is a convolution that represents the linear contribution to $\delta H/\delta w(\boldsymbol{r})$ and F represents all non-linear contributions. For polymer models it is typically most convenient to express the kernel function c in Fourier space where it is diagonal and positive definite [17] and the linearized force convolution $c*w$ can be computed via simple multiplication. The linearized force $c * w$ typically is derived from a linear response analysis about the translationally invariant disordered phase of the system and thus constitutes an approximation to the true linear force that is only accurate for weak perturbations about the disordered state. The explicit kernel functions for the diblock model considered in this work are given in Appendix A.

After splitting the force into linear and non-linear parts, semi-implicit algorithms can be devised in order to stabilize the algorithm. One such algorithm is a first order

semi-implicit scheme (SI1), which is defined by

$$w^{j+1}(\boldsymbol{r}) - w^{j}(\boldsymbol{r}) = \Delta t \left(-c * w^{j+1}(\boldsymbol{r}) + F(\boldsymbol{r}; [w^{j}]) \right) + R^{j}(\boldsymbol{r}) \tag{2.14}$$

Another similar algorithm that uses linearized force information is the first-order exponential time differencing ETD1 method, [31, 75] which is derived by using c as an integrating factor over the time interval $t \to t + \Delta t$.

$$\hat{w}^{j+1}(\boldsymbol{k}) - \hat{w}^{j}(\boldsymbol{k}) = \frac{1 - e^{-\hat{c}(k)\Delta t}}{\hat{c}(k)} \hat{G}(\boldsymbol{k}; [w^{j}]) + \left(\frac{1 - e^{-2\hat{c}(k)\Delta t}}{2\hat{c}(k)\Delta t} \right)^{1/2} \hat{R}^{j}(\boldsymbol{k}) \tag{2.15}$$

here the equation has been transformed from real space, $\boldsymbol{r}$, to Fourier space, $\boldsymbol{k}$, with hats over symbols indicating Fourier transforms $\hat{w}(\boldsymbol{k}) = \mathcal{F}_{\boldsymbol{r} \to \boldsymbol{k}}(w(\boldsymbol{r}))$. Note that the linear response kernel $\hat{c}(k)$ is a function of the magnitude of the Fourier mode $k = |\boldsymbol{k}|$.

All of the fictitious dynamics algorithms discussed so far have first-order accuracy with respect to time step. In the stochastic case with $R \neq 0$, this is first-order accuracy in the weak sense. To achieve higher-order accuracy we employ predictor-corrector algorithms. These algorithms perform an initial "predictor" time step, then use this predicted field to more accurately evaluate the force over the time step interval for a subsequent improved corrector step. These algorithms must evaluate the force two times per iteration, but have second-order accuracy (in the weak sense) in fictitious time. The simplest of these is the Euler-Maruyama predictor corrector (EMPEC2) method

$$\bar{w}(\boldsymbol{r}) - w^{j}(\boldsymbol{r}) = \Delta t \, G(\boldsymbol{r}; [w^{j}]) + R^{j}(\boldsymbol{r}) \tag{2.16}$$

$$w^{j+1}(\boldsymbol{r}) - w^{j}(\boldsymbol{r}) = \frac{\Delta t}{2} (G(\boldsymbol{r}; [w^{j}]) + G(\boldsymbol{r}; [\bar{w}])) + R^{j}(\boldsymbol{r}) \tag{2.17}$$

It is important to use the same noise realization $R^{j}(\boldsymbol{r})$ in both the predictor and corrector steps in order to fully cancel the leading-order weak error of the algorithm. The noise

statistics here are the same as for the EM1 method.

There are also variants of this algorithm that use linearized force information, such as an algorithm due to Petersen and Öttinger (PO2) [21, 76]. We also introduce here an ETD type algorithm that is similar to the predictor corrector algorithms, but is instead based on a Runge-Kutta approach [75]. This ETDRK2 algorithm is defined by

$$\hat{\bar{w}}(\boldsymbol{k}) - \hat{w}^j(\boldsymbol{k}) = \frac{1 - e^{-\hat{c}(k)\Delta t}}{\hat{c}(k)}\hat{G}(\boldsymbol{k};[w^j]) + \left(\frac{1 - e^{-2\hat{c}(k)\Delta t}}{2\hat{c}(k)\Delta t}\right)^{1/2}\hat{R}^j(\boldsymbol{k}) \tag{2.18}$$

$$\hat{w}^{j+1}(\boldsymbol{k}) - \hat{\bar{w}}(\boldsymbol{k}) = \frac{\hat{c}(k)\Delta t + e^{-\hat{c}(k)\Delta t} - 1}{(\hat{c}(k))^2\Delta t}\left(\hat{F}(\boldsymbol{k};[\bar{w}]) - \hat{F}(\boldsymbol{k};[w^j])\right) \tag{2.19}$$

The predictor step is an ETD1 step as described above, while the corrector step is based on a trapezoidal Runge-Kutta approximation. Note that this algorithm is slightly different than a predictor corrector ETD method described elsewhere [31].

The final type of algorithm we consider is an adaptive time-stepping (ADT) method for CL simulations. This approach was introduced by Aarts and coworkers in the context of CL sampling of quantum chromodynamics models [32]. The first adaptive time-stepping algorithm that we consider, EM1ADT, uses a simple Euler-Maruyama update scheme with a time step that is updated between iterations according to

$$\Delta t_j = \frac{K}{\max(|G(\boldsymbol{r};[w^j])|)}\overline{\Delta t} \tag{2.20}$$

$$w^{j+1}(\boldsymbol{r}) = w^j(\boldsymbol{r}) + \Delta t_j\, G(\boldsymbol{r};[w^j]) + R^j(\boldsymbol{r}) \tag{2.21}$$

where $\overline{\Delta t}$ is the nominal time step and K is an adjustable parameter. Typically K is set to be close to the average modulus of the force so that if a large force value is encountered, the time step is reduced to allow for more accurate time integration. In contrast, if the forces are small, then Δt is increased to allow for sampling more states. In all ADT calculations in this work, the parameter K was computed by averaging the

modulus of the force over the first 1000 iterations, unless otherwise specified. No adaptive time-stepping is performed over these initial calibration steps and the iteration proceeds with the nominal time step. One can determine if the ADT method is well calibrated by plotting the time step to ensure it fluctuates around the nominal value $\overline{\Delta t}$. Operator values must also be weighted by the adaptive time step when computing averages and other statistics. The adaptive time-stepping approach can easily be generalized to any other algorithm. A second ADT scheme that we consider here is the EMPEC2ADT method, which layers adaptive time-stepping on top of EMPEC2 updates:

$$\Delta t_j = \frac{K}{\max(|G(\boldsymbol{r};[w^j])|)}\overline{\Delta t} \tag{2.22}$$

$$\bar{w}(\boldsymbol{r}) = w^j(\boldsymbol{r}) + \Delta t_j\, G(\boldsymbol{r};[w^j]) + R^j(\boldsymbol{r}) \tag{2.23}$$

$$w^{j+1}(\boldsymbol{r}) = w^j(\boldsymbol{r}) + \frac{\Delta t_j}{2}(G(\boldsymbol{r};[\bar{w}]) + G(\boldsymbol{r};[w^j])) + R^j(\boldsymbol{r}) \tag{2.24}$$

It is important for both the EM1ADT and EMPEC2ADT schemes that the variance of the noise is adjusted with the time step: $\langle R^j(\boldsymbol{r})R^k(\boldsymbol{r}')\rangle = 2\Delta t_j\,\delta_{jk}\delta(\boldsymbol{r}-\boldsymbol{r}')$.

As a final note, there are other small changes to each algorithm that can be made. For both SCFT and CL fictitious dynamics simulations, we include a positive, constant mobility λ as a coefficient to the force for each field and in the noise variance. These mobilities affect the relative speed at which each field is updated. Additionally, when performing SCFT calculations with first-order fictitious dynamics algorithms (EM1, SI1, ETD1), the fields are not updated simultaneously but rather follow a staggered scheme where only one field is updated per iteration and the stiffer w_+ pressure mode is updated first [17]. For the AB diblock model considered here, the staggered updates with the

EM1 algorithm can be described mathematically as,

$$w_+^{j+1}(\boldsymbol{r}) = w_+^j(\boldsymbol{r}) + \lambda_+ \Delta t \, G_+(\boldsymbol{r}; [w_+^j, w_-^j]) \tag{2.25}$$

$$w_-^{j+1}(\boldsymbol{r}) = w_-^j(\boldsymbol{r}) + \lambda_- \Delta t \, G_-(\boldsymbol{r}; [w_+^{j+1}, w_-^j]) \tag{2.26}$$

For CL calculations, all fields are always updated simultaneously, i.e.

$$w_+^{j+1}(\boldsymbol{r}) = w_+^j(\boldsymbol{r}) + \lambda_+ \Delta t \, G_+(\boldsymbol{r}, [w_+^j, w_-^j]) + R_+^j(\boldsymbol{r}) \tag{2.27}$$

$$w_-^{j+1}(\boldsymbol{r}) = w_-^j(\boldsymbol{r}) + \lambda_- \Delta t \, G_-(\boldsymbol{r}, [w_+^j, w_-^j]) + R_-^j(\boldsymbol{r}) \tag{2.28}$$

Including a mobility $\lambda_\pm$ changes the variance of the noise to $\langle R_\pm^j(\boldsymbol{r}) R_\pm^k(\boldsymbol{r}') \rangle = 2\lambda_\pm \Delta t \, \delta_{jk} \delta(\boldsymbol{r} - \boldsymbol{r}')$.

2.3.1 Software

All calculations involving Anderson mixing were computed using the publicly available PSCF code developed at the University of Minnesota [69]. Both the FORTRAN90 and C++ versions of the code were tested, with quantitative agreement between the two. All data presented in this work used the C++ version of the code. The FORTRAN90 version of the code was pulled on February 2, 2020 (SHA1 67d107f3a6) and the C++ version was pulled on July 1, 2020 (SHA1 3ed5f6caac). All calculations involving fictitious dynamics or CL sampling were performed using a UCSB-developed custom C++ code.

All SCFT calculations were computed using a single thread on an Intel Xeon E5-2630 CPU. All CL simulations were executed on NVIDIA V100 GPUs [77].

2.4 Results

2.4.1 Self-Consistent Field Theory

We first evaluate the various algorithms in the context of SCFT. For each algorithm we examine the stability properties and the ways its performance can be adjusted via numerical parameters.

There is one adjustable parameter for the AM method: the history length, n_h. Although keeping a longer history length typically leads to faster convergence of field updates, it also increases the computational cost of the calculation. This is both due to increased memory requirements of storing the field history as well as the arithmetic operations required to update the fields, which scale like $\mathcal{O}(n_h^2 M)$. Recall that to evaluate the force requires $\mathcal{O}(N_s M \ln(M))$ operations, so if $n_h^2 \sim N_s \ln(M)$ then field updates can have comparable cost to that of evaluating the force. For typical parameter values of $N_s = 100$ and $M = 64^3$ this crossover occurs at $n_h = 35$. To combat this problem it is common practice when performing field updates to map the fields from the original grid in real space with M samples to a symmetry reduced space with M_r samples, where $M_r \ll M$ [22, 24]. This leads to a field update cost of $n_h^2 M_r$. After conducting the field update, the fields are then mapped back to the original grid to perform pseudospectral evaluations of the force. In the case of the highly symmetric double gyroid phase, which has the space group $Ia\bar{3}d$, a full grid of size $M = 64^3$ is reduced to $M_r = 2761$, corresponding to a factor of 95 reduction. In addition to reducing the computational cost of a given field update step, using symmetry reduction also decreases the dimension of the space that must be searched for the saddle-point, which typically leads to faster convergence. A disadvantage to using symmetry reduction is that it limits the overall set of structures that are possible to explore. Performing large-cell quenches to discover phases [78–81], and to study defects, thin films, and other asymmetric structures is not

possible using techniques that impose the symmetry elements of a space group on the fields.

We compare the number of iterations and the time it takes to converge a calculation to a force tolerance of 10^{-8} using the AM algorithm for a unit cell of the double gyroid phase with and without symmetry reduction at $f = 0.34$ and $\chi N = 30$ in Figure 2.1. All calculations were initialized from a converged SCFT calculation at $\chi N = 20$ and $f = 0.37$ and were run until a prescribed force cutoff of 10^{-8} was achieved. When constructing a phase diagram, it is common to use one point in phase space with a converged structure to initialize a nearby point in phase space to accelerate the saddle-point search. As such, the change in both χN and f between the seed fields and the converged fields is a representative test for the algorithms.

The top panel of Figure 2.1 illustrates that increasing history length reduces the iterations required to converge, nearly monotonically. This is expected because a longer history length leads to a more efficient search towards the saddle-point. Additionally, the symmetrized calculations ($Ia\bar{3}d$) converge with fewer iterations than the calculations without symmetrization ($P1$). In the bottom panel, the CPU time required to complete the calculation is plotted. For the symmetrized case, the run time nearly perfectly mirrors the iterations in the top panel. This indicates that the increased computational cost of larger n_h is negligible in the total cost of an iteration. For the $P1$ calculations, the conclusion is quite different. The CPU time required decreases as n_h is increased from 5 to 20, but for $n_h \geq 25$ the CPU time increases with increasing n_h despite the fact that the total number of field update iterations is decreasing. This clearly indicates that the cost of a field update is no longer negligible and is affecting the overall run time. The transition occurs close to the prior scaling-based estimate of $n_h = 35$. This procedure was repeated at $\chi N = 40$ and $\chi N = 60$ with qualitatively the same conclusions. The only major difference occurred at $\chi N = 60$, where the $P1$ calculations would not converge for

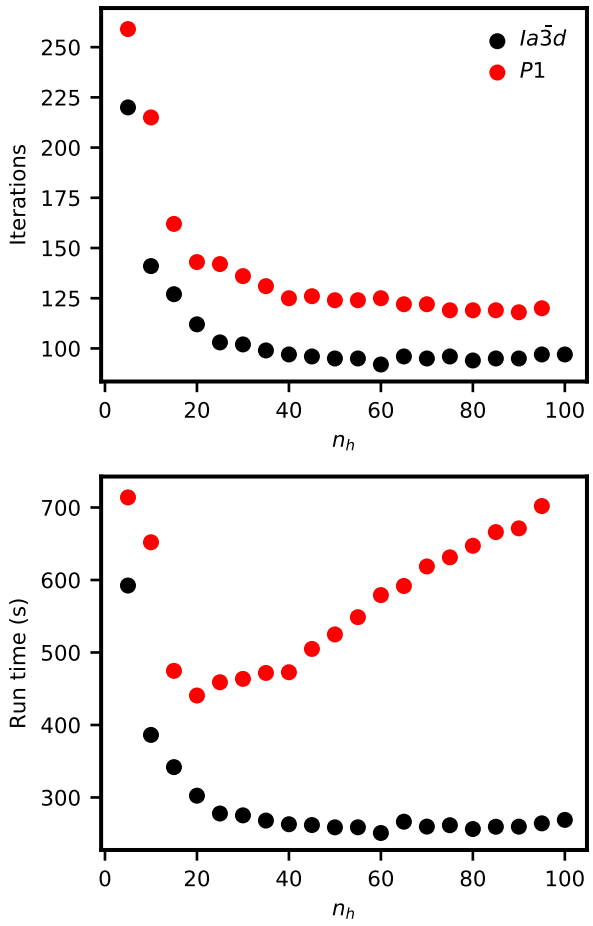

Figure 2.1: Convergence rate for AM method with and without symmetrization at $\chi N = 30$. $P1$ indicates that no symmetry reduction is used, whereas $Ia\bar{3}d$ uses the symmetry of the double gyroid phase. The spatial discretization with no symmetry reduction was $M = 64^3$. All calculations were performed using a single thread on an Intel Xeon E5-2630 CPU.

any value of n_h attempted.

For the fictitious dynamics algorithms, the adjustable parameters are the time step Δt and mobilities, λ_+ and λ_-, used to update each field. Each field mobility can be set independently, but only two out of the three time step and mobility parameters are independent because they appear in the combinations $\lambda_+\Delta t$ and $\lambda_-\Delta t$ in all algorithms. For the SCFT studies we therefore arbitrarily set $\Delta t = 1$ and vary the two mobilities. Because fictitious dynamics algorithms have one more parameter compared to AM, the parameter space for fictitious dynamics is larger and requires more work to optimize the performance. Some heuristics can be constructed to help reduce the burden of this search, however [26].

In analogy to the AM method, we evaluated the various time steppers over a range of field mobility values. These data are presented in Figure 2.2. In all cases the calculations were initialized from the same fields used in the AM studies and were run until the l_2 norm of the forces on w_+ and w_- were both less than 10^{-8}.

Unlike the AM method, changing the parameters does not affect the arithmetic cost of a field update step, so we only consider the number of iterations required to reach the force cutoff. Figure 2.2 shows that the EM1 method is by far the least stable and only converges for $\lambda_+ = \lambda_- = 1$ out of the values attempted. The mobility values attempted here are relatively aggressive and most algorithms will have larger stability windows at smaller mobility values. The semi-implicit, first-order algorithms (SI1 and ETD1) perform much better than EM1 and converge for nearly any $\lambda_+ > \lambda_-$. The fastest convergence from the values considered occurs for $\lambda_+ = 50$ and $\lambda_- = 20$. Although not shown, increasing either mobility above these values starts to destabilize the algorithm and leads to slower convergence. Finally, the second order algorithms show an intermediate level of stability, but converge quite quickly with optimal parameter selection. The EMPEC2 and PO2 algorithms perform best for $\lambda_+ = \lambda_-$, while the ETDRK2 algorithm performs best with

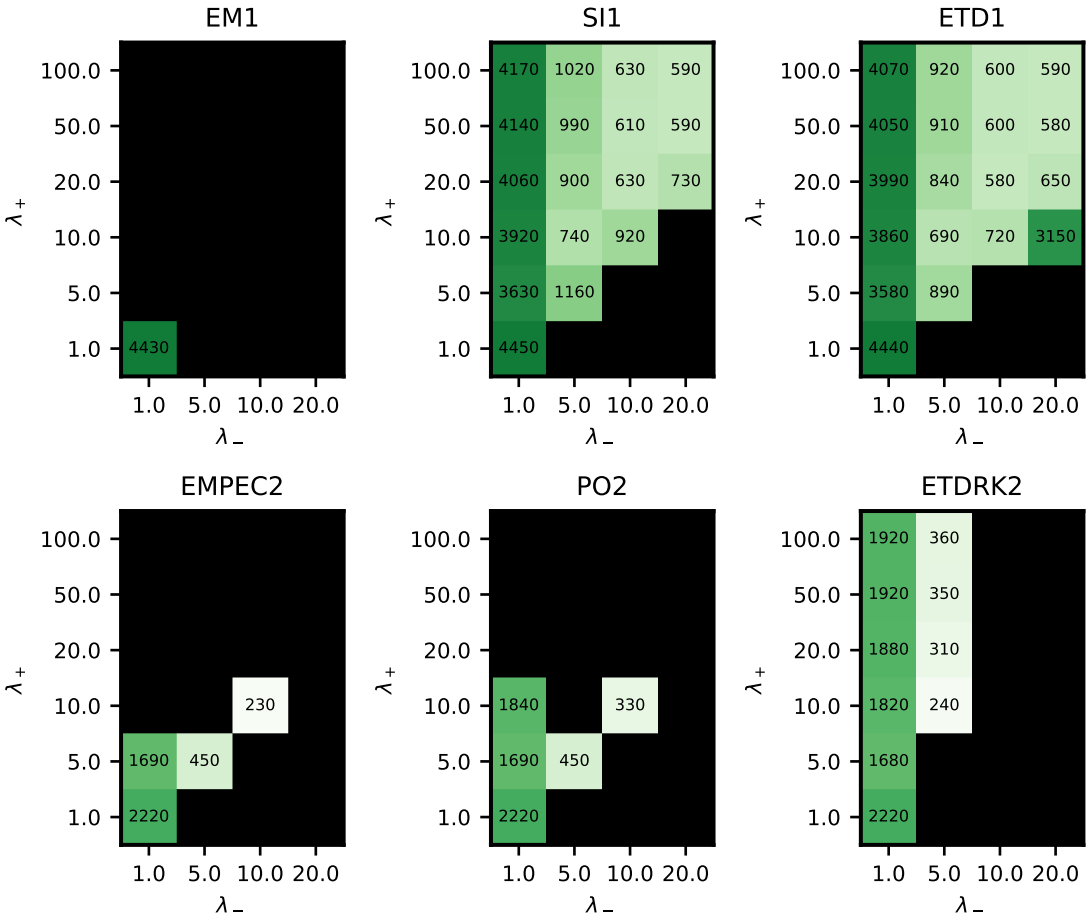

Figure 2.2: Iterations to convergence for time steppers at $\chi N = 30$. λ_+ is the time step for the w_+ field and λ_- is the time step for the w_- field. The number inside each square indicates iterations to convergence. Black squares indicate that the calculation did not converge.

$\lambda_+ > \lambda_-$. These three algorithms require approximately half as many iterations as the SI1 and ETD1 algorithms, but each iteration requires twice as many force evaluations, so it is unclear which is faster from these data alone.

To further probe the question of which algorithm converges fastest, we examine the absolute value of the error in the intensive Hamiltonian as a function of the number of force evaluations. Comparing the different algorithms based on iterations to convergence can be misleading because the second order algorithms require twice as many force evaluations per iteration. It is also not reliable to compare run times from different software implementations that were used for different algorithms. Many software design decisions such as single vs. double precision arithmetic, numerical library selection, and hardware availability (CPU vs. GPU) can outweigh the effect of algorithm choice. As such we use number of force evaluations as the computational effort metric because, apart from the previously mentioned edge case of non-symmetrized AM with long history length, evaluating the forces should typically be the dominant computational burden and the number of times that this is required therefore determines the overall run time.

Figure 2.3 shows the error in the intensive Hamiltonian versus the number of force evaluations conducted for the various algorithms at $\chi N = 30$. All calculations were run until the change in the Hamiltonian between iterations was less than 10^{-10}. The error was then referenced to this final value of the Hamiltonian. For all algorithms we used the parameter values that led to the lowest CPU time to convergence. For most applications an error of 10^{-4} to 10^{-6} in the Hamiltonian is sufficient to accurately compute phase boundaries. At $\chi N = 30$, the EMPEC2 time stepper and both AM algorithms are all nearly equivalent. The ETDRK2 algorithm is slightly slower, and is then followed by PO2, ETD1, and SI1. Finally EM1 is much slower to converge than any other algorithm. Increasing χN to 40 or 60 leads to some slight variations in the relative performance of the algorithms shown in Figure 4 and Figure 5. For very high accuracy (tighter

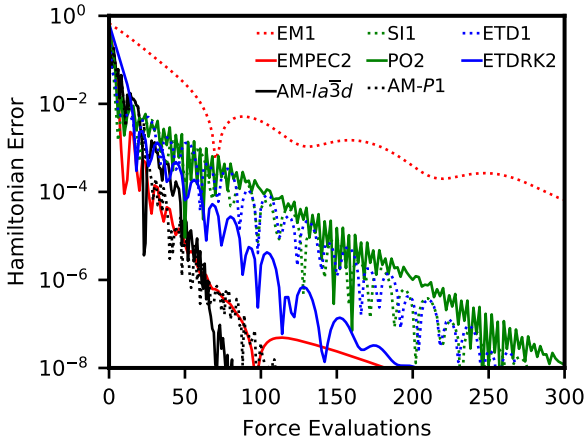

Figure 2.3: Error in the per-chain intensive Hamiltonian in units of k_BT after a given number of force evaluations. All calculations were conducted at $\chi N = 30$.

than 10^{-7}) and strong segregation strengths, the AM algorithm with symmetrization shows faster convergence than any of the time steppers (Figure 2.5). The time steppers demonstrate a long tail of slow convergence at very high accuracy for strong segregation. AM without symmetrization is not stable at $\chi N = 60$, re-emphasizing the importance of symmetrization to the efficacy of the AM algorithm.

For all conditions tested, the EMPEC2 algorithm was fastest of all the time steppers, despite being one of the most simple. All of the semi-implicit algorithms rely on a linear response derived in the disordered phase. This linear response information is not a good match for the true linear force in the ordered double gyroid phase being tested here, which may limit or eliminate the benefit from the implicit part. The EMPEC2 algorithm on the other hand obtains all information about force variation over a time interval numerically from the predictor-corrector scheme and does not rely on approximate linear response information. Additionally, the second-order schemes nearly universally converge faster than the first-order algorithms, despite having smaller stability windows. This may be attributed to the lower time accuracy of the first-order schemes. Although in SCFT we are concerned only with the effort to find the saddle point and not with accurately

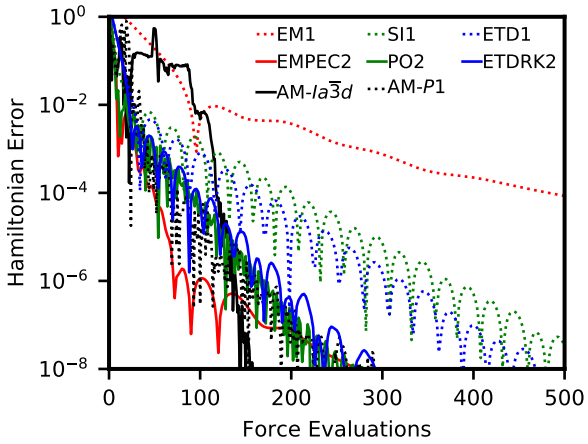

Figure 2.4: Same as Figure 2.3 but at $\chi N = 40$.

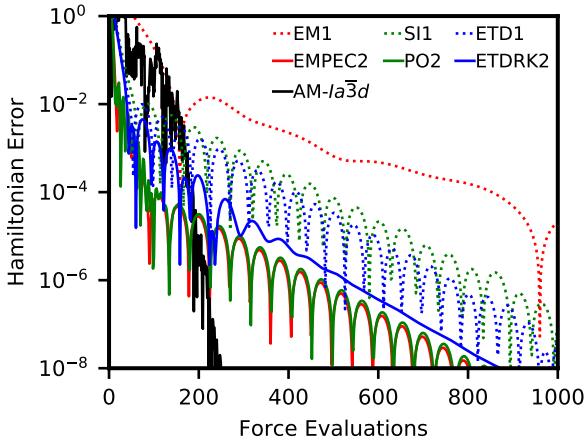

Figure 2.5: Same as Figure 2.3 but at $\chi N = 60$.

reproducing a dynamical trajectory, the time-step errors in the first-order methods can make the trajectory divert from the fastest path to convergence. This can be seen in the oscillatory change in the Hamiltonian in Figures 2.3–2.5.

2.4.2 Field Theoretic Simulations

We now consider full FTS that are not limited by the mean field approximation of SCFT. As previously stated, the most efficient way to conduct such simulations without approximation is with the complex Langevin method. Unfortunately, there is no easy way to convert the AM algorithm into one that can correctly sample fluctuations in an FTS, so we do not consider it for the remainder of this work. The time steppers on the other hand can trivially be extended to include fluctuations by including an additional noise term in the update. We begin by evaluating the performance of the different algorithms in the *disordered* phase at $f = 0.34$, $\chi N = 10$ and $C = 20$ in a cubic box of size $V = 9^3\, R_g^3$ with $M = 48^3$. The melt is also compressible with $\zeta N = 100$ and the polymer density has been smeared with a range of $a = 0.2\, R_g$. The mobilities are fixed at $\lambda_+ = 2$ and $\lambda_- = 1$. In FTS, the effective Hamiltonian is not a physically relevant operator, so we instead consider the excess chemical potential relative to the ideal gas of copolymer chains, the average of which is plotted in Figure 2.6 for a range of time step sizes. The excess chemical potential operator is defined as $\tilde{\mu}_{\text{ex}} = -\ln Q[w_+, w_-]$ where $\tilde{\mu}_{\text{ex}}$ is in units of the thermal energy $k_B T$. The physical observable, μ_{ex}, is then computed according to

$$\mu_{\text{ex}} = \langle \tilde{\mu}_{\text{ex}} \rangle = \frac{\int \mathcal{D}w_+ \int \mathcal{D}w_- \, \tilde{\mu}_{\text{ex}} \exp(-H[w_+, w_-])}{\int \mathcal{D}w_+ \int \mathcal{D}w_- \exp(-H[w_+, w_-])} \tag{2.29}$$

where $\langle \ldots \rangle$ indicates a thermodynamic ensemble average. Under the ergodic principle with CL importance sampling, the ensemble average can be replaced with a CL time average.

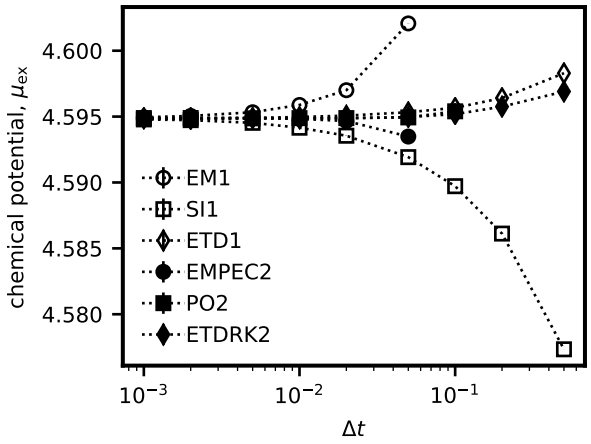

Figure 2.6: Average value of the chemical potential for the disordered phase at $\chi N = 10$, $f = 0.34$, and $C = 20$.

An ideal algorithm will be able to produce accurate values at large time steps in order to reduce simulation times. At small Δt all algorithms show good agreement, but as Δt is increased various algorithms start to show time-integration errors. For CL simulations it is important to accurately reproduce the *trajectory* of the fictitious dynamics in order to properly importance sample the system. The first-order methods (EM1, SI1, and ETD1) have the worst accuracy scaling with Δt and show the strongest divergence from the true value of μ_{ex} as Δt increases. In particular the EM1 and SI1 algorithms perform worst, while the ETD1 algorithm is nearly as accurate as the second order methods, which weakly diverge from the true value of μ_{ex} with increasing Δt over the range of time steps tested. Although perhaps less limiting than accuracy requirements for FTS, another important aspect for an algorithm is its stability. The most stable algorithm will be able to run at large Δt, which enables sampling more CL time for a given amount of CPU time. This leads to tighter confidence intervals for estimates (via reduced statistical sampling error) for a given amount of resources.

In the disordered phase there is a clear maximum time step for each algorithm, above which the simulation diverges in fewer than 100 iterations; these conditions are found

where the lines of Figure 2.6 terminate for large Δt. The most stable algorithms, i.e. the ones with largest maximum Δt, are the semi-implicit algorithms SI1, ETD1, and ETDRK2 which have $\Delta t_{\max} = 0.5$. The PO2 algorithm uses semi-implicit information in the corrector step but relies on a fully explicit Euler step in the predictor, which confers it with worse stability ($\Delta t_{\max} = 0.1$) compared to the other semi-implicit methods. Finally, the EM1 and EMPEC2 algorithms show the worst stability of the tested algorithms ($\Delta t_{\max} = 0.05$), which is unsurprising as they make no attempt to use semi-implicit information. Notably in this disordered system, the linear response functions used to construct the semi-implicit algorithms are accurate for weak fluctuations about the homogeneous state, which likely leads to the much better performance of these algorithms compared to SCFT of the double gyroid phase. When considering both stability and accuracy, the ETD1 and ETDRK2 algorithms perform best and produce comparable levels of error. The ETD1 algorithm requires half as many force evaluations as the ETDRK2 algorithm, however, making it the most cost efficient algorithm. The high accuracy and stability found for the ETD1 algorithm are in agreement with similar studies of the Edwards homopolymer solution model [7] and three and four-species block polymer melts [26].

Repeating the same CL calculations at $\chi N = 30$ for the double gyroid phase yields qualitatively similarly results, though the trends are not quite as clear. These data are presented in Figure 2.7. At small Δt all algorithms converge to the same value. As Δt is increased, the algorithms with first-order accuracy start to show significant errors while second-order accurate algorithms remain close to the true value. Unlike in the disordered phase, there is no clear maximum time step for each algorithm, however. Instead, as Δt is increased, the algorithms become statistically more likely to follow divergent trajectories. This can be quantified via a mean time to divergence, defined as the harmonic mean of

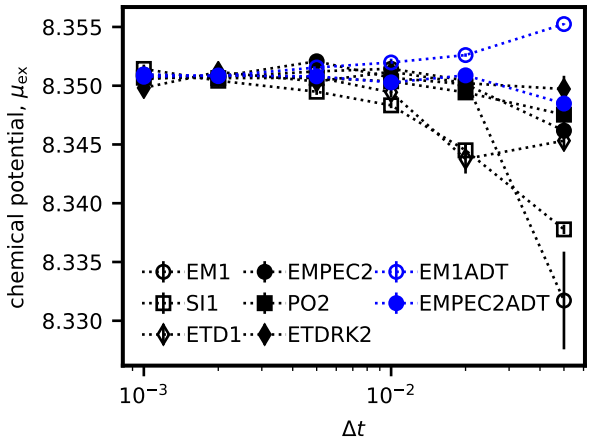

Figure 2.7: Average value of the chemical potential for the double gyroid phase at $\chi N = 30$, $f = 0.34$, and $C = 20$.

the CL simulation time before a calculation diverges. Mathematically,

$$\bar{\tau}_{div} = \left(\frac{1}{n_s} \sum_{j=1}^{n_s} \frac{1}{\tau_{div,j}} \right)^{-1} \tag{2.30}$$

where $\tau_{div,j}$ is the divergence time for an individual trajectory and j indexes statistically independent simulations of which there are n_s. A simulation is terminated as divergent when any individual field value is IEEE 754-defined +INF, -INF or NAN. The mean divergence times were computed from ten independent trajectories and are plotted in Figure 2.8.

All calculations were run for a maximum of two million iterations. The solid black line in Figure 2.8 indicates the maximum CL time that could be achieved with two million iterations at a given time step. For $\Delta t \leq 0.005$ all algorithms have a divergence time that lies on top of the $\tau_{\max}$ curve, indicating that no calculations diverged for the entire CL time window. At larger Δt various algorithms have $\tau_{\text{div}} < \tau_{\max}$ indicating that divergence became limiting rather than the specified iteration cap. For $\Delta t = 0.05$ all algorithms except EM1ADT have $\tau_{div} \ll \tau_{max}$. In contrast to the simulations for the disordered

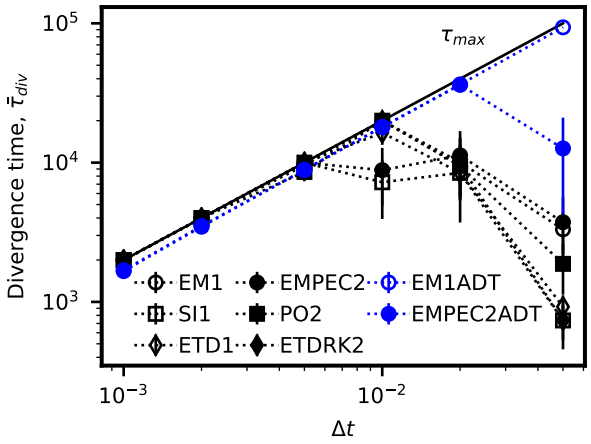

Figure 2.8: Harmonic mean divergence time for the double gyroid phase at $\chi N = 30$, $f = 0.34$, and $C = 20$.

phase, simulations of a microphase separated system show no overall performance benefit from algorithms using semi-implicit information over the Euler-based methods, which is similar to the behavior for SCFT of the double gyroid phase. Again this is presumably due to the fact that the linear response functions used in the semi-implicit algorithms are not appropriate for the double gyroid phase. The algorithms that perform best are the ones that use adaptive time stepping. The EM1ADT algorithm never diverged over the range of time steps used in this study, while the EMPEC2ADT algorithm only diverged for $\Delta t = 0.05$.

In Appendix A we explore in further detail what actually causes a CL simulation to diverge. We conclude that even though the saddle-point is a local fixed point of the CL dynamics, it is possible to fluctuate to a nearby trajectory that is analytically divergent (non-bound). These divergent trajectories are not attractive, but cause the force to grow exponentially, which can lead to poor time-integration accuracy and the emergence of extremely large field values. It is also possible for trajectories to leave the basin of attraction for the desired microphase and enter an attractive basin for another microphase (i.e. free-energy barrier crossing) or an unphysical state. This topic is explored further

in Appendix A. If a very small time step is used on the periphery of the basin near a divergent trajectory, then the algorithm can be significantly stabilized. The adaptive time stepping algorithms do exactly this: when the force is large the time step is small. The EMPEC2ADT algorithm is slightly less stable than the EM1ADT algorithm because EMPEC2ADT chooses the time step based on the current value of the force, but updates the fields based on the current and future forces. When near a divergent trajectory this can lead to reduced suppression of instabilities. Nevertheless the EMPEC2ADT algorithm has much better accuracy compared to EM1ADT (see Figure 2.7), and may be a better choice if stability is not limiting. As noted previously, it is possible to construct adaptive time-stepped versions of the other algorithms, but the fixed-time-step semi-implicit algorithms do not perform better than the Euler-based algorithms in the double gyroid phase, so we do not expect the ADT versions to perform better either.

As a final study, we examine how the adaptive time stepping algorithms can be used to run simulations in regions of parameter space that were previously inaccessible. We consider the same diblock copolymer system, but now at $\chi N = 80$ and $\zeta N = 200$ and in a cubic box size $V = 12\,R_g^3$ with $M = 64^3$. The time step is fixed at $\Delta t = 0.01$ and we examine algorithm performance as the chain number density, C, is varied. As C decreases the relative strength of fluctuations increases, leading to increased probability for divergence. The divergence time is plotted in Figure 2.9. All calculations were initialized from the SCFT saddle-point fields of the same double gyroid phase. This initialization choice causes a warm up period for every trajectory, during which the fluctuations are slowly incorporated as the simulation evolves. The warm up time for each algorithm is presented in Figure 2.10.

Figure 2.9 again shows that adaptive time-stepping is much more stable than fixed-time-step approaches. Over all values of C considered, the EM1ADT algorithm never diverged. Although not shown, the algorithm is also stable below $C = 1$, however the

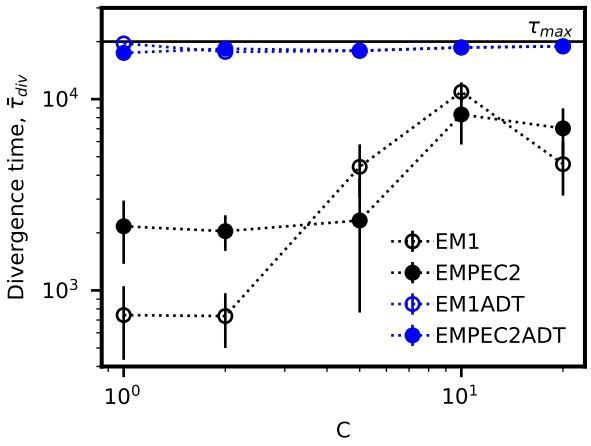

Figure 2.9: Harmonic mean divergence time for the double gyroid phase at $\chi N = 80$ and $f = 0.34$.

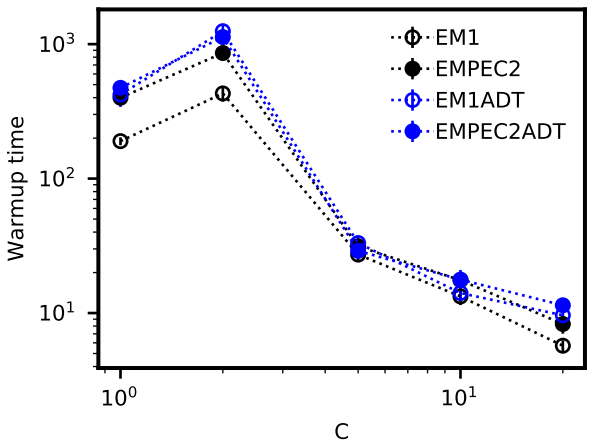

Figure 2.10: Mean warm up time for the double gyroid phase at $\chi N = 80$ and $f = 0.34$.

double gyroid phase starts to become unstable relative to the disordered phase because of strong fluctuations at small C. In contrast, the fixed-time-step algorithms (EM1 and EMPEC2) have a decreasing divergence time with decreasing C. As fluctuations become stronger at small C, the fixed-time-step algorithms become susceptible to an instantaneous perturbation to the fields which pushes the fields far away from the saddle-point, and can lead to a divergent trajectory. The adaptive time steppers on the other hand can accurately integrate forward in time and prevent escape from the stable basin.

The problem of simulating small C with fixed-time-step algorithms is further accentuated by examining the warm up time in Figure 2.10. For all algorithms the warm up time increases as C decreases, indicating that fluctuations away from the saddle-point become more important as C is decreased. For $C < 2$ the warm up time for the EM1 and EMPEC2 algorithms is approaching the divergence time for each algorithm. This makes it difficult to collect any data because the simulation is likely to diverge by the time the system has become thermalized. Such stability problems are not present with adaptive time stepping, but the averaging time for the K parameter had to be increased to 50,000 iterations for $C \leq 2$.

2.5 Conclusion

We examined a wide array of field update algorithms to perform polymer SCFT calculations and field theoretic simulations (FTS). These algorithms fall into two groups: Anderson-mixing (AM) and fictitious dynamics. We show that AM and fictitious dynamics algorithms perform similarly under physically relevant conditions for SCFT, as long as the numerical parameters have been tuned appropriately. The AM approach is advantaged in that it has fewer numerical parameters compared to the fictitious dynamics algorithms, but the latter methods are more robust when simulating systems with low

spatial symmetry. We also find that fictitious dynamics algorithms with second-order time accuracy can outperform first-order methods despite doubled cost per time step.

For complex Langevin field theoretic simulations we observed that the exponential time-differencing type algorithms outperform all others in disordered phases because of the availability of useful linear response information and their sophisticated use of this information. In ordered mesophases, adaptive time stepping (ADT) is found to dramatically stabilizes algorithms and is much more important than individual algorithm choice. The ADT algorithms also allow access to parameter spaces characteristic of strong fluctuations (e.g. low C) that were previously intractable. These insights should aid future field theoretic simulations of a wide variety of polymer models.

2.6 Acknowledgements

This material is based upon work supported by the National Science Foundation Graduate Research Fellowship Program under Grant No. 1650114 and by the National Science Foundation CMMT Program under Award Nos. DMR-1822215 and DMR-2104255. Any opinions, findings, and conclusions or recommendations expressed in this material are those of the author(s) and do not necessarily reflect the views of the National Science Foundation. Use was made of computational facilities purchased with funds from the National Science Foundation (OAC-1925717) and administered by the Center for Scientific Computing (CSC). The CSC is supported by the California NanoSystems Institute and the Materials Research Science and Engineering Center (MRSEC; NSF DMR 1720256) at UC Santa Barbara.

Chapter 3

Phase Behavior for Linear, Comb, and Bottlebrush Diblock Copolymers

3.1 Introduction

Block copolymers have been a topic of vigorous research for many decades due to their ability to self-assemble into a wide variety of microstructures that impart an array of different materials properties. In recent years a set of microstructures known as Frank-Kasper sphere phases have been identified in block copolymer systems [82, 83]. These sphere phases have long been known in metal alloys and typically have high coordination number and low symmetry, containing numerous spheres in the primitive cells.

Recent studies have revealed that a critical factor in forming Frank-Kasper phases is conformational asymmetry [39], which describes the tendency of one or more blocks to form looser or tighter coils compared to other blocks. This conformational asymmetry can allow a molecule with composition that would typically lead to formation of a

cylinder phase to instead adopt a microphase consisting of spherical domains. Conformational asymmetry is typically defined as the ratio of length scales between two different monomers. The length scales used include the Kuhn length, statistical segment length, or packing length.

Conformational asymmetry is not the only mechanism that can facilitate Frank-Kasper phase formation: it has previously been shown that comb-like and bottlebrush block copolymers can form Frank-Kasper phases in the absence of contrasting statistical segment lengths if there are sufficient differences in the architecture between blocks [38]. The fact that both architectural variations and conformational asymmetry can be used to stabilize Frank-Kasper phases implies that the two factors may produce similar effects on self assembly. A similar relationship between architecture and conformational asymmetry was studied in the context of mikto-arm star block copolymers by Milner [40]. Using strong segregation theory (SST), he showed that for an A_nB_m star block copolymer, a combined architectural and conformational asymmetry parameter, ϵ, can be defined that collapses the phase behavior of any combination of n and m to a single phase diagram. More recently, a similar SST study was conducted by Zhulina and coworkers for comb-like and bottlebrush copolymers, which showed that conformational asymmetry could be combined with architectural parameters such as grafting density and side chain length [41] to produce a single asymmetry parameter. They also showed that the dependence of ϵ on architectural parameters differs between the comb-like regime and bottlebrush regime. The comb-like regime is characterized by short side chains with low grafting density, where backbone properties dominate the conformational asymmetry, while in the bottlebrush regime the side chains are long and densely grafted, leading to different chain backbone behavior and increased importance of side chain properties. The different regimes are also characterized by different scaling of microphase domain size with polymer length [37, 84]. The boundary between these two regimes is discussed

in detail elsewhere [85].

Although these SST studies have provided powerful insights, they are limited in both accuracy and detail. For example, SST studies are typically based on describing chain packing in a simple unit cell of planar, cylindrical, or spherical domains. This approximation prevents the comparison of low-symmetry microphases with a delicate free-energy balance of competing domain orderings, such as the Frank-Kasper sphere phases considered here. It has also been shown that SST can lead to qualitatively incorrect predictions: perhaps most notably, SST predicted that the double gyroid network morphology is not stable compared to hexagonally packed cylinders or lamellae [86–88], but numerical self-consistent field theory (SCFT) showed that double gyroid is in fact stable [19].

In this work, we use full numerical SCFT calculations to study Frank-Kasper phases in linear, comb-like, and bottlebrush block copolymers. Numerical SCFT allows us to compare the free energies of the Frank-Kasper phases to establish the most stable candidate, and we show that a universal phase diagram for linear and comb-like block copolymers can be generated with the introduction of an appropriate asymmetry parameter, ϵ. We do not observe a transition from comb-like scaling to bottlebrush scaling, despite considering polymers with grafting density as high as two and side chain degree of polymerization greater than thirty. We attribute this absence of bottlebrush scaling to the mean-field approximation that underlies SCFT.

3.2 Model and Methods

3.2.1 Field Theory Model of interacting AB diblocks

We consider incompressible melts of linear, comb-like, and bottlebrush diblock polymers. Figures 3.1 qualitatively shows the difference between linear, comb-like, and bottle-

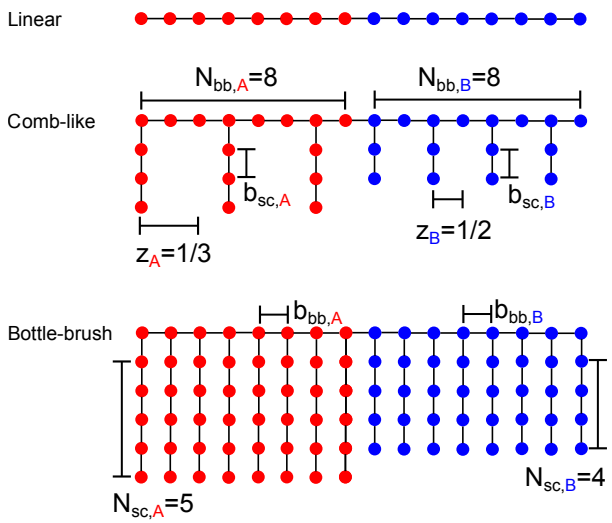

Figure 3.1: Illustration of linear, comb-like, and bottlebrush polymers and the relevant architectural parameters.

brush block copolymers and illustrates the molecular architecture parameters including backbone degree of polymerization (N_{bb}), side-chain degrees of polymerization (N_{sc}), and the grafting density (z), defined as the average number of grafts per backbone segment. We define the total degree polymerization, N, of a block copolymer with m distinct chemical blocks to be:

$$N = \sum_{i=1}^{m} (z_i N_{sc,i} + 1) N_{bb,i} \tag{3.1}$$

The conventional field theory model for an incompressible melt of AB-type block and graft copolymers is [1, 59]

$$Z(n, V, T) = Z_0 \int \mathcal{D}w_+ \int \mathcal{D}w_- \, \exp(-H[w_+, w_-]) \tag{3.2}$$

$$H[w_+, w_-] = C \left(\frac{1}{\chi N} \int d\mathbf{r} \, (w_-(\mathbf{r}))^2 - i \int d\mathbf{r} \, w_+(\mathbf{r}) - \bar{V} \ln Q[w_A, w_B] \right) \tag{3.3}$$

where $Z(n, V, T)$ is the partition function for a canonical ensemble of n copolymers in a volume V at fixed temperature T. Z_0 is a reference partition function for an ideal gas

of copolymers, and H is an effective Hamiltonian for the interacting system. The A and B segments interact through a Flory-Huggins interaction parameterized by χ. Polymer segments are defined to have equal volume, v_0, for all species. All spatial integrals are over the scaled volume $\bar{V} = V/R_g^3$ and the spatial coordinate $\mathbf{r}$ has been scaled by a reference polymer radius of gyration R_g. In all calculations in this work, we impose periodic boundary conditions on the simulation cell.

The parameter C describes a dimensionless chain density and is related to the occupied and pervaded volume of a chain. Occupied volume is the volume in space filled by the segments from a single chain due to excluded volume interactions $V_{\text{occ}} = v_0 N$, whereas pervaded volume is the minimum volume required to circumscribe a single polymer coil in a sphere or cylinder. For a linear homopolymer chain in its own melt, a measure of the pervaded volume is the unperturbed radius of gyration cubed,

$$V_{\text{perv,linear}} = R^3_{g,\text{linear}} = b^3 N^{3/2} 6^{-3/2} \tag{3.4}$$

where b is the statistical segment length. The ratio of pervaded volume to occupied yields the dimensionless chain concentration,

$$C = \frac{V_{\text{perv}}}{V_{\text{occ}}} \tag{3.5}$$

which is a prefactor to every term in the effective Hamiltonian eq 6.2. Because occupied and pervaded volumes have different scaling with the degree of polymerization N, the dimensionless chain concentration C is proportional to the square root of N for a linear chain. This is often expressed as an invariant degree of polymerization $\bar{N} = 6^3 C^2$.

For non-linear chains we must use alternative expressions for the pervaded volume and chain concentration, C. For comb-like polymers it is assumed that pervaded volume

is dominated by the backbone,

$$V_{\text{perv,comb}} = R_{g,bb}^3 = \frac{b_{bb}^3 N_{bb}^{3/2}}{6^{3/2}} \tag{3.6}$$

which yields the dimensionless chain concentration

$$C_{\text{comb}} = \frac{b_{bb,A}^3 N_{bb}^{3/2}}{6^{3/2} v_0 N} \tag{3.7}$$

where we have used the A block backbone segment length as a reference segment length.

For a bottlebrush polymer, estimation of the pervaded volume is more difficult because both side chains and the backbone contribute meaningfully. Blob scaling methods can be used to estimate the mean square end-to-end vector of the chain [41, 85]

$$\langle R_{\text{lb}}^2 \rangle = \frac{v_0 z}{b_{sc}} N_{sc}^{1/2} N_{bb} \tag{3.8}$$

which can be used to estimate the pervaded volume. This yields

$$C_{\text{lb}} = \frac{v_0^{1/2} z_A^{3/2} N_{sc,A}^{3/4} N_{bb}^{3/2}}{b_{sc,A}^{3/2} N} \tag{3.9}$$

These equations represent the "loose brush" regime [85, 89] and are applicable for $z < (b_{bb}^2 b_{sc}/v_0)^2$. For higher grafting densities, the polymer enters the dense brush regime, for which the appropriate expressions are

$$\langle R_{\text{db}}^2 \rangle = (z v_0 b_{bb} N_{sc})^{1/2} N_{bb} \tag{3.10}$$

and

$$C_{\text{db}} = \frac{z_A^{3/4} b_{bb,A}^{3/4} N_{sc,A}^{3/4} N_{bb}^{3/2}}{v_0^{1/4} N} \tag{3.11}$$

All bottlebrushes considered in this work have sufficiently low grafting density to remain in the loose brush regime.

The single-chain partition function $Q[w_A, w_B]$ describes the interactions of a single chain with the auxiliary fields. The form of Q depends on the molecular architecture and chain statistics and is explored in detail in the following section. Q also has a parametric dependence on the chain composition that is described by the species A volume fraction f_A. The fields experienced by each monomer w_A and w_B are related to the auxiliary fields by the following linear combination of the $w_\pm$ fields

$$w_A \equiv iw_+ - w_- \qquad\qquad w_B \equiv iw_+ + w_- \tag{3.12}$$

3.2.2 Chain Statistics

There are a variety of models used to describe the chain statistics of flexible polymer chains. Bead-linker models with either freely-rotating joints (FJC) or Gaussian springs (DGC) are both popular choices [51, 59, 90]. Additionally, a continuous Gaussian thread (CGC) model is also commonly used to describe long polymer strands [1, 91]. For comb-like and bottlebrush polymers, there are often short polymer segments between grafts along the backbone. For this type of architecture it is thought that the CGC model is inappropriate due to overstretching of the backbone [37]. In this work we consider linear chains with CGC, DGC, and FJC chain statistics, as well as branched polymers with DGC and FJC chain statistics. Crucially, a FJC backbone cannot overstretch beyond its contour length.

We demonstrate how to compute the single-chain partition function $Q[w_A, w_B]$ for a linear AB diblock copolymer with the aforementioned chain statistics. Extending this approach to branched molecules such as bottlebrush copolymers is discussed elsewhere

[8, 84, 92]. For a linear chain, the single-chain partition function is computed from the propagator $q(\mathbf{r}, s; [w_A, w_B])$, which describes the random walk statistics of a chain starting from a free end and ending at a contour position s.

$$Q[w_A, w_B] = \frac{1}{\bar{V}} \int d\mathbf{r}\, q(\mathbf{r}, 1; [w_A, w_B]) \tag{3.13}$$

For a polymer block with continuous Gaussian chain statistics the single-chain propagator, $q(\mathbf{r}, s)$, satisfies the modified diffusion equation

$$\frac{\partial}{\partial s} q(\mathbf{r}, s) = \left(\frac{(b(s))^2}{b_{\mathrm{bb,A}}^2} \nabla^2 - w(\mathbf{r}, s) \right) q(\mathbf{r}, s) \tag{3.14}$$

where $b(s) = b_A$ and $w(\mathbf{r}, s) = w_A(\mathbf{r})$ for $s \in (0, f_A]$ and $b(s) = b_B$ and $w(\mathbf{r}, s) = w_B(\mathbf{r})$ for $s \in (f_A, 1]$. The propagator satisfies the initial condition $q(\mathbf{r}, 0) = 1$. The chain contour dimension s has been scaled by the chain length, N.

For a polymer block with discrete bead-linker chain statistics, the single-chain propagator $q_j(\mathbf{r})$ no longer depends on a continuous contour position variable s but rather on an integer bead index j. The single chain partition function is defined according to

$$Q[w_A, w_B] = \frac{1}{\bar{V}} \int d\mathbf{r}\, q_N(\mathbf{r}; [w_A, w_B]) \tag{3.15}$$

The propagator has an initial condition

$$q_1(\mathbf{r}) = \exp(-w_1(\mathbf{r})/N) \tag{3.16}$$

and is iterated forward using the Chapman-Kolmogorov equation

$$q_{j+1}(\mathbf{r}) = \exp(-w_{j+1}(\mathbf{r})/N) \int d\mathbf{r}'\, \Phi_j(|\mathbf{r} - \mathbf{r}'|) q_j(\mathbf{r}') \tag{3.17}$$

where $\Phi_j(r)$ is the normalized bond transition probability. As in the case of the continuous Gaussian chain, both $w_j(\mathbf{r})$ and $\Phi_j(r)$ are piecewise functions of the contour index j defined according to

$$w_j(\mathbf{r}) = \begin{cases} w_A(\mathbf{r}) & 1 \leq j \leq f_A N \\ w_B(\mathbf{r}) & f_A N + 1 \leq j \leq N \end{cases} \tag{3.18}$$

$$\Phi_j(r) = \begin{cases} \Phi_A(r) & 1 \leq j \leq f_A N \\ \Phi_B(r) & f_A N + 1 \leq j \leq (N-1) \end{cases} \tag{3.19}$$

where Φ_A and Φ_B are normalized bond transition probabilities that define the linker statistics in the A and B blocks, respectively. The linker that connects the A block to the B block is of type A.

In this work, we consider Gaussian springs and freely rotating joints as linkers. The mathematical form of the bond transition probability $\Phi_K(r)$ is most conveniently expressed in Fourier space and is defined according to

$$\hat{\Phi}_K(k) = \begin{cases} \exp\left(-\frac{b_K^2}{N b_{\mathrm{bb,A}}^2} k^2\right) & \text{Gaussian} \\ j_0\left(\frac{6^{1/2} b_K}{N^{1/2} b_{\mathrm{bb,A}}} k\right) & \text{freely jointed} \end{cases} \tag{3.20}$$

where K is either A or B and $j_0(x) = \sin(x)/x$ is a spherical Bessel function of the first kind.

3.2.3 Numerical Self Consistent Field Theory

Self-consistent field theory (SCFT) is a mean-field approximation to the full theory described previously, and is defined by the saddle point equations

$$\left.\frac{\delta H[w_+, w_-]}{\delta w_+(\mathbf{r})}\right|_{w_+^*, w_-^*} = \left.\frac{\delta H[w_+, w_-]}{\delta w_-(\mathbf{r})}\right|_{w_+^*, w_-^*} = 0 \tag{3.21}$$

After obtaining $w_\pm^*$ fields that satisfy the above equations, the corresponding free energy is computed by approximating the functional integral over field configurations with the mean-field values

$$\frac{F}{k_B T} = -\ln\ Z_c \approx H[w_A^*, w_B^*] \tag{3.22}$$

This mean-field approximation becomes asymptotically exact where the parameter C goes to infinity.

To search for the saddle point fields, we use fictitious dynamics schemes [17]. For all calculations involving bottlebrush copolymers Heun's predictor-corrector method is used, while all other linear and comb-like copolymers use an exponential time differencing (ETD) scheme [31, 75]. In addition to searching for the saddle point fields, we also allow the simulation cell to relax its shape and size to attain a stress-free configuration [93]. The calculations are considered converged when the L_2 norm of the forces and stresses are below tolerances of 10^{-5} and 10^{-4}, respectively.

The field update equations require evaluating the chain propagator described previously. For continuous Gaussian chains, the modified diffusion equations were solved by a second-order pseudo-spectral method [14, 15] with a contour discretization of $\Delta s = 0.01$. All discrete bead-linker polymers also used a pseudospectral approximation [1] to efficiently compute the convolutions required in the iterative update scheme described

by eq 3.17.

Phase diagrams are constructed by comparing candidate phases' free energies, including BCC spheres, FCC spheres, hexagonally packed cylinders (HEX), and tetrahedrally close-packed sphere phases A15 and σ. Spatial discretization of all phases are summarized in Appendix B.

3.2.4 Conformational Asymmetry, Chain Scaling, and the Bottlebrush Transition

Conformational asymmetry is intimately tied to the concepts of occupied volume and pervaded volume. As previously discussed, the ratio of these quantities yields a dimensionless chain concentration, C, which is related to the invariant degree of polymerization, $\bar{N}$. An alternative quantity can be defined that is independent of the degree of polymerization:

$$p_{\text{linear}} = \frac{v_0}{b^2} \tag{3.23}$$

where p is a length scale that is often referred to as the "packing length" and is a materials property of a given monomer [94]. It is also proportional to a modified ratio of the occupied and pervaded volume:

$$p \propto \frac{V_{\text{occ}}}{V_{\text{perv}}^{2/3}} \tag{3.24}$$

Conformational asymmetry then compares the relative size of the packing length for one polymer species to another [95]. Because the segment volumes are defined to be equal, for a linear chain, we obtain

$$\epsilon_{\text{linear}} = \sqrt{\frac{p_B}{p_A}} = \frac{b_A}{b_B} \tag{3.25}$$

However, this definition of conformational asymmetry is not universal, and some authors omit the square root leading to $\epsilon = b_A^2/b_B^2$ [38, 95, 96].

We can use eq 3.24 to estimate the packing length for comb and bottlebrush polymers as well. Using the previously obtained estimates for pervaded volume, we estimate the packing length of block i of a comb as

$$p_{i,\text{comb}} = \frac{v_0(1 + z_i N_{sc,i})}{b_{bb,i}^2} \tag{3.26}$$

which yields an epsilon definition of

$$\epsilon_{\text{comb}} = \frac{b_{bb,A}}{b_{bb,B}} \sqrt{\frac{z_B N_{sc,B} + 1}{z_A N_{sc,A} + 1}} \tag{3.27}$$

Repeating the exercise for loose and dense bottlebrush polymers yields

$$\epsilon_{\text{lb}} = \frac{b_{sc,B}^{1/2} N_{sc,B}^{1/4}}{b_{sc,A}^{1/2} N_{sc,A}^{1/4}} \tag{3.28}$$

and

$$\epsilon_{\text{db}} = \frac{(b_{bb,A} z_B N_{sc,B})^{1/4}}{(b_{bb,B} z_A N_{sc,A})^{1/4}} \tag{3.29}$$

Both loose and dense brushes are characterized by $\epsilon \propto N_{sc}^{1/4}$ and $C \propto N_{bb}^{1/2} N_{sc}^{-1/4}$. Comb-like polymers on the other hand have an asymmetry parameter that is predicted to scale like $N_{sc}^{1/2}$. In addition, the loose bottlebrush asymmetry parameter depends on the side chain segment lengths b_{sc}, whereas the comb-like prediction depends on backbone segment lengths b_{bb}. As previously stated, the polymers in this work have sufficiently low grafting density z that we do not expect to observe dense brush scaling.

3.3 Results and Discussion

3.3.1 Universal Phase Diagram

We first compare the phase behavior of linear, comb-like, and bottlebrush copolymers with continuous Gaussian (CGC), discrete Gaussian (DGC), and freely jointed (FJC) chain statistics. In contrast to typical block-copolymer phase diagrams, which map the space of the composition, f_A, and segregation strength, χN, we instead fix $\chi N = 60$ and examine the effect of conformational asymmetry, ϵ, and f_A.

For linear polymers we vary $b_{bb,B}/b_{bb,A}$ to sweep a range of ϵ_{linear} values. For comb-like and bottlebrush polymers we choose equal segment lengths $b_{sc,A} = b_{bb,A} = b_{sc,B} = b_{bb,B}$ and grafting density of unity $z_A = z_B = 1$. The length of side chains, $N_{sc,A}$ and $N_{sc,B}$, were then varied to change ϵ. For comb-like polymers we set $N_{sc,A} = 0$ and varied $N_{sc,B}$ from 0 to 8. For the bottlebrush polymer we require $N_{sc,A} + N_{sc,B} = 40$ for all molecules. The bottlebrush polymers thus have significantly longer side chains than the comb-like polymers. For each molecule we then computed the value of ϵ according to eqs 3.25, 3.27, or 3.28, and constructed stability boundaries in f_A for each microphase at $\chi N = 60$ using linear interpolation of free energies. These data are presented in Figure 3.2.

The phase boundaries for different architecture and chain statistics all agree well, except for the bottlebrush polymers. In Figure 3.3, we replot the bottlebrush polymer data, instead using the comb-like ϵ_{comb} prediction (eq 3.27). This figure shows near universal phase boundaries between all architectures and chain statistics. The strongest deviations are at the σ-A15 phase boundary. These deviations are not unexpected because the A15 and σ phases are very close in free energy (of order of 10^{-4} kT per chain) [39,96–98], and small changes to polymer structure will have a much larger relative impact on the position of the phase boundary compared to the boundaries between other pairs of phases. There is also an appreciable difference in the phase boundary between BCC and HEX

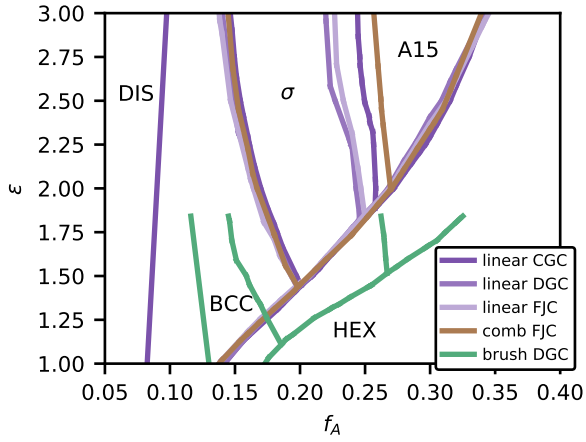

Figure 3.2: SCFT phase diagrams for linear, comb, and bottlebrush copolymers with CGC, DGC, and FJC chain statistics at $\chi N = 60$. For linear chains, segment lengths are varied to change ϵ, whereas for comb and bottlebrush polymers the side chain lengths are varied. DIS-BCC boundaries are not shown for linear DGC, linear FJC, and comb FJC polymers.

phases near $\epsilon = 1$ when comparing bottlebrushes to other architectures. We attribute this difference to the large shift in the order-disorder transition (ODT) when comparing linear CGC polymers and brush DGC polymers. The ODT shift for bottlebrush block copolymers is discussed in Appendix B. The ODTs for other discrete polymers are not shown in Figure 3.3 due to the difficulty resolving the position of the phase boundary with the coarse composition variations of discrete chains. To precisely locate the ODT requires identifying a point in phase space where microphases are metastable compared to the disordered phase. This is sometimes not possible with discrete chains due to the discrete set of compositions available, whereas for continuous chains all compositions are easily accessible. Nevertheless, the approximate ODTs for linear DGC, linear FJC, and comb FJC have f_A within ± 0.01 of the linear CGC ODT.

Although applying the comb-like scaling of eq 3.27 to the bottlebrush data yields a nearly universal phase diagram, it prompts the question of why polymers with a nominal bottlebrush architecture are behaving like combs. To further pursue this question, we

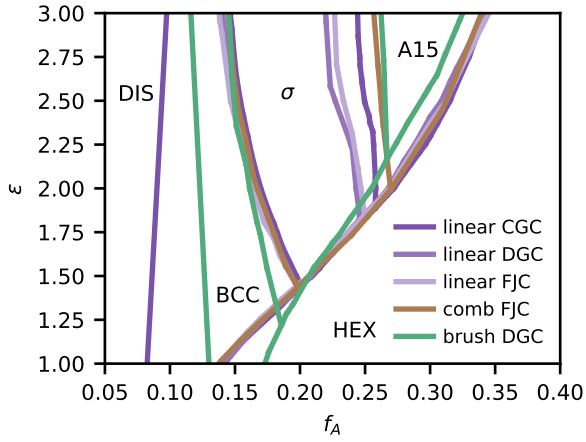

Figure 3.3: Same as Figure 3.2, but the bottlebrush ϵ was computed using eq 3.27 instead of eq 3.28.

Case	$b_{bb,B}$	$b_{sc,A}$	$b_{sc,B}$	z_A	z_B	$N_{sc,A}$	$N_{sc,B}$	ϵ_{comb}
1a)	1	1	1	1	1	2	11	2.0
1b)	1	1	3/2	1	1	2	11	2.0
1c)	2/3	1	1	1	1	2	11	3.0
1d)	1	1	1	1/6	1	2	11	3.0
2a)	1	1	1	1	1	8	32	1.9
2b)	1	1	3/2	1	1	8	32	1.9
2c)	2/3	1	1	1	1	8	32	2.9
2d)	1	1	1	1	2	8	32	2.7

Table 3.1: Case studies parameters for bottlebrush and comb-like polymers. All segment lengths, b, are given relative to the reference segment length $b_{\text{bb,A}}$

examined the effect of other architectural parameters such as segment lengths b and grafting density z.

3.3.2 ϵ dependence on segment lengths and grafting density

Previous architecture variations allowed us to probe the dependence of ϵ only on side-chain lengths. Other architectural parameters such as segment lengths and grafting densities could further affect the conformational asymmetry. To examine these effects, we systematically vary backbone segment lengths, side-chain segment lengths, and grafting

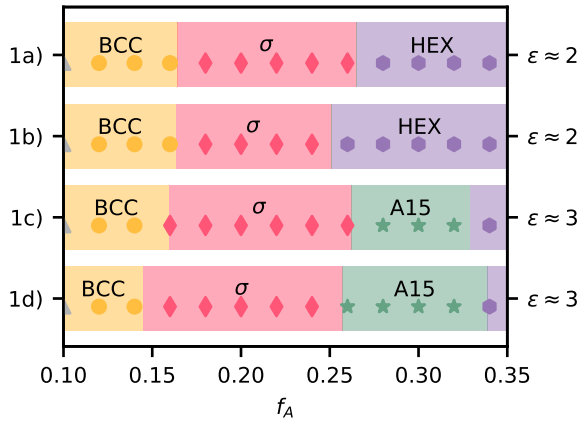

Figure 3.4: Variations in phase stability with different architectural changes. 1a) Reference molecule with identical segment lengths and grafting density. 1b) B block side chain segment length increased to 3/2. 1c) B block backbone segment length decreased to 2/3. 1d) A block grafting density decreased to 1/6. Full architectural parameters are given in Table 3.1.

density and evaluate the phase stability windows. We investigate four cases for both comb-like (1a-1d) and bottlebrush polymers (2a-2d), with parameters listed in Table 3.1. In the same table we list the corresponding value of ϵ_{comb} using the comb-like scaling law eq 3.27.

Figure 3.4 shows the phase stability windows for the four comb architectures, Cases 1a-1d. Case 1a denotes a reference model where the A side chain has 2 beads, the B side chain has 11 beads, and the bond lengths are all unity. These parameters combine to give $\epsilon_{\text{comb}} = 2$. The stability windows for the BCC, σ and HEX phases shown in Figure 3.4 are in agreement with the universal phase diagram, Figure 3.3 at $\epsilon = 2$, as expected. For Case 1b, the side-chain segment length of the B block is increased to 3/2. The corresponding phase diagram is nearly identical to the Case 1a, so that, in agreement with eq 3.27, the comb's side chain segment length should not contribute to the asymmetry parameter ϵ. This result is expected from physical intuition because the side chains of comb-like polymers are short relative to the backbone and do not contribute

substantially to the pervaded volume. In Case 1c, the *backbone* segment length of the B block was decreased to 2/3. By substituting this $b_{bb,B}$ into eq 3.27, $\epsilon_{\text{comb}} = 3$ is predicted, and a stability window for the A15 phase appears in the phase diagram consistent with $\epsilon = 3$ in Figure 3.3. Finally, a decreased grafting density in the A block ($z_A = 1/6$) was considered in Case 1d, which from eq 3.27 is expected to provide another route to $\epsilon_{\text{comb}} = 3$ and has the expected phase boundaries. These results show that the comb-like prediction for ϵ has the correct dependence (or independence) on the model parameters and is appropriate even for collapsing the boundaries between complex sphere phases.

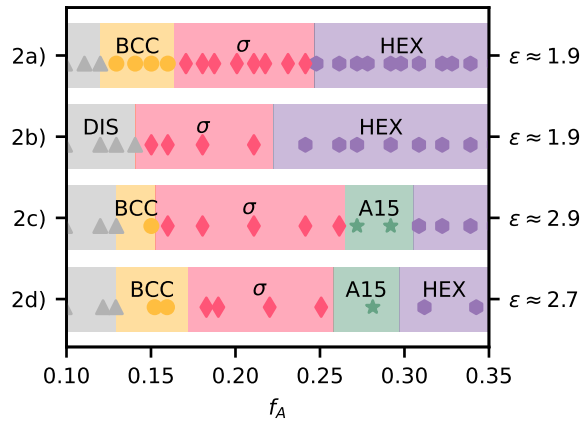

Figure 3.5: Variations in phase stability with different architectural changes. 2a) Reference molecule with identical segment lengths and grafting density. 2b) B block side chain segment increased to 3/2. 2c) B block backbone segment length decreased to 2/3. 2d) B block grafting density increased to 2. Full architectural parameters are given in Table 3.1.

For bottlebrush polymers, we also contrast four cases (2a-2d) to explore the effect of segment length and grafting density. Case 2a is the reference case with all equivalent segment lengths and grafting density of unity. We predict the conformational asymmetry using the comb-like expression (eq 3.27) because it yielded a nearly universal phase diagram in Figure 3.3. The predicted conformational asymmetry for Case 2a is $\epsilon_{\text{comb}} = 1.9$.

In Case 2b, the side chain segment length of the B block is increased to 3/2. Eq 3.27 predicts that ϵ_{comb} is independent of side chain segment length so the predicted value remains the same as for Case 2a. In the corresponding phase diagram, we observe that the complex sphere phase window does not expand, but we see a shifted order-disorder phase boundary that removes the BCC window. More details concerning the BCC phase can be found in the supplementary information and will be discussed in more detail in future publications. Notably, the bottlebrush prediction for ϵ (eq 3.28) depends on the side chain segment length which would demand a shift in phase boundaries between Cases 2a and 2b. This further reinforces that the finding that the molecules termed "bottlebrush" in this work obey comb-like scaling rather than bottlebrush scaling.

In Case 2c, the backbone segment length of the B block is decreased to 2/3. Using eq 3.27 we find that $\epsilon = 2.9$ and observe that the phase diagram has A15 and σ phase boundaries commensurate with the universal phase diagram at the same ϵ value. The bottlebrush prediction for ϵ is independent of backbone segment lengths, so if bottlebrush scaling were obeyed, there would be no difference between Case 2a and Case 2c; this is in contradiction with the SCFT results.

Finally, in Case 2d, we increase the grafting density to $z_B = 2$. This increase corresponds to the highest grafting density and side chain length considered, placing the molecules most deeply into the expected bottlebrush scaling regime [85, 89]. The bottlebrush scaling prediction for conformational asymmetry (eq 3.28) has no dependence on grafting density, however. Case 2d in Figure 3.5 shows a clear stability window for the A15 phase, indicating that Case 2d has more conformational asymmetry than Case 2a. The relative position of phase boundaries is also commensurate with the universal phase diagram when using comb-like ϵ predictions. This phase behavior further indicates that the comb-like scaling is more appropriate than the bottlebrush relation. All bottlebrush polymers have therefore shown comb-like (eq 3.27) dependence on segment length and

grafting density.

The most obvious explanation for these data is that the bottlebrush polymers used in this work remain in the comb-like scaling regime despite relatively long side chains and high grafting densities. In the next section, we explore what is required to reach the bottlebrush regime in field-theoretic models.

3.3.3 Alternate models and fluctuation effects

We have established that both our comb-like and bottlebrush block copolymers follow a form of ϵ given in eq 3.27, consistent with the comb scaling regime. However, we expected the bottlebrush block copolymers to observe a different form of ϵ. Zhulina and coworkers studied architectural asymmetry in comb and bottlebrush block copolymers by combining strong segregation results with blob scaling methods [41, 85]. Our $\epsilon \sim (N_{sc,B}/N_{sc,A})^{1/2}$ is consistent with their predictions in the comb-like regime, but our bottlebrush results fail to observe the $\epsilon \sim (N_{sc,B}/N_{sc,A})^{1/4}$ prediction expected for the dense brush regime.

We believe that the mean-field approximation of SCFT is responsible for underestimating the side chain contribution to backbone stiffening for flexible chains. It is postulated that side chains in the comb regime interpenetrate one another, but in the bottlebrush regime side chains form impermeable blobs. One can determine the crossover between these two regimes by comparing the pervaded and occupied volume of the side chains which yields [99]

$$\Theta = \frac{(zN_{\mathrm{sc}} + 1)v_0}{N_{\mathrm{sc}}^{1/2} b_{\mathrm{sc}} b_{\mathrm{bb}}^2} \tag{3.30}$$

This grouping is referred to as the crowding parameter, Θ. The comb region is found for $\Theta < 1$ whereas bottlebrush behavior is expected for $\Theta \geq 1$. In numerical SCFT simulations, we can set the architectural parameters N_{sc}, z, and N_{bb}, but the quantity

v_0/b^3 does not appear because it multiplies all terms in the saddle point equations. Instead, the quality of the mean-field approximation is controlled by the ratio v_0/b^3 as it enters the Ginzburg parameter C. As stated previously, the mean-field approximation of SCFT becomes asymptotically exact for large C.

We can use eq 3.30 to estimate what regime the polymers from this study fall under. For hydrocarbon polymers, v_0/b^3 is typically of order 0.1 [94], so we use this value to approximate the experimental values of Θ and C. The polymers with the longest side chains and highest grafting density considered in this work had $z = 2$, $N_{sc} \approx 30$, and $N_{bb} \approx 100$, which combine to yield $\Theta \approx 1.1$ and is in the bottlebrush regime, contrary to our SCFT results. We next compute the dimensionless chain concentration, which yields $C_{\mathrm{lb}} \approx 1.9$. For SCFT to be accurate, we require $C \gg 1$, which is not true for the polymers considered here.

In order to accurately capture bottlebrush behavior in SCFT we require $\Theta \geq 1$ and $C \gg 1$. One approach to reach this regime is to increase the backbone degree of polymerization since C increases with N_{bb}, but Θ is unaffected. Unfortunately, the largest accessible value is $N_{bb} \approx 2000$ due to memory constraints of numerical SCFT simulations on contemporary GPU hardware[1]. This relatively large value of N_{bb} combined with the previous values of $v_0/b^3 = 0.1$, $z = 2$, and $N_{sc} = 30$ yields $C_{\mathrm{lb}} \approx 8.4$, which is still far below the asymptotic limit of large C where SCFT is accurate. While future computational developments may enable accurate numerical SCFT simulations of the bottlebrush regime, it is currently an intractable task to simulate polymers with sufficiently long backbones.

We have explained why our SCFT calculations cannot capture the bottlebrush regime,

[1]The memory required to store the propagator object q is proportional to the backbone length times the number of spatial grid elements. For the σ phase, which requires approximately 2^{20} spatial grid points, a polymer with $N_{bb} \approx 2000$ would require nearly 32 GB of memory to store the propagators in double precision.

but we still must explain why the nominally bottlebrush polymers instead behave like combs. To reach a limit where the mean-field approximation is reasonable ($C > 100$) using the previous parameter values of $z = 2$, $N_{sc} \approx 30$ and $N_{bb} \approx 100$, requires $v_0/b^3 \approx 1 \times 10^{-4}$. This is an unphysically small value of v_0/b^3 for hydrocarbon polymers, but SCFT calculations are not restricted by v_0/b^3. Inserting this value of v_0/b^3 and the other parameters into eq 3.30 yields $\Theta \approx 1.1 \times 10^{-3}$, which is clearly deep in the comb regime. Thus, the "bottlebrush" polymers with short backbones considered in this work actually behave like combs under conditions where the mean-field approximation of SCFT is accurate.

The inability of SCFT to account for backbone stiffening induced by side chains has been partially avoided by Dalsin and coworkers, who instead chose to model the bottlebrush backbone using wormlike-chain statistics [37]. This choice of model manually introduces the required stiffening, controlled by an extra persistence length parameter, rather than observing its spontaneous emergence from excluded volume effects. Using this model, they investigated lamellar domain sizes and found that explicitly introduced chain stiffening led to agreement in domain sizes between experimental and SCFT bottlebrushes. Unfortunately, the worm-like chain has a dramatically increased computational cost compared to flexible-chain models due to resolving two additional dimensions required to account for chain segmental orientation. The computational cost has to date limited the worm-like chain phase behavior studies for bottlebrushes to one-dimension mean-field calculations, although it maybe to possible to explore other ordered phases for bottlebrushes [100].

Recent work by Panagiotou and coauthors utilized fully fluctuating field-theoretic simulations to investigate the melt behavior of bottlebrush homopolymers with flexible backbone statistics [8]. These fully fluctuating simulations relax the mean field approximation of SCFT and are accurate for small values of C. The authors found that at

small values of C, spontaneous backbone stiffening emerges in intrinsically flexible bottlebrushes. Recent algorithmic advances have also made it possible to simulate microphase-separated polymers at the low values of C characteristic of the bottlebrush regime [101]. Unfortunately, constructing phase diagrams requires free energies, which are not trivial to obtain in FTS, with the current state-of-the-art methods relying on costly thermodynamic integration [9,21]. We defer fully fluctuating field-theoretic simulations for a future study, but speculate that bottlebrush-like scaling will emerge spontaneously in diblock bottlebrush polymers with flexible linker statistics when the mean-field approximation is lifted.

3.4 Conclusions

We performed SCFT calculations on linear, comb-like, and bottlebrush diblock copolymers. We show that a universal phase diagram can be defined for these varied architectures by relating side chain length, segment lengths and grafting densities to conformational asymmetry. Other authors predict a change in chain scaling at high side chain length and grafting density [41], which marks the transition between comb-like and bottlebrush polymers, but we do not observe such a transition in SCFT.

3.5 Acknowledgements

The authors thank Joshua Lequieu and Kevin Dorfman for helpful discussions. This work was partially supported by the DMREF Program of the National Science Foundation under Award DMR-1725414 (T.Q. and K.T.D) and by the U.S. Department of Energy, Office of Basic Energy Sciences, under Award Number DE-SC0019001 (D.S, D.V., and G.F.). D.V. and T.Q. acknowledge support from the National Science Foun-

dation Graduate Research Fellowship Program under grant no. 1650114. Any opinions, findings, and conclusions or recommendations expressed in this material are those of the author(s) and do not necessarily reflect the views of the National Science Foundation. Use was made of computational facilities purchased with funds from the National Science Foundation (OAC-1925717) and administered by the Center for Scientific Computing (CSC). The CSC is supported by the California NanoSystems Institute and the Materials Research Science and Engineering Center (MRSEC; NSF DMR 1720256) at UC Santa Barbara.

Chapter 4

Self-Consistent Field Theory for Coherent States Models

Numerical auxiliary field (AF)-based self consistent field theory (SCFT) has become a standard tool in modern polymer physics. It has been used to predict, interrogate, and understand many phenomena in inhomogeneous polymer systems, such as self-assembly and phase behavior [1]. The core of numerical AF SCFT is computing polymer density fields, $\tilde{\psi}(\boldsymbol{r})$, from propagators, $q(\boldsymbol{r}, s)$, which describe the random-walk statistics of polymers in an auxiliary potential field, $w(\boldsymbol{r})$, where s indexes the chain contour position and $\boldsymbol{r}$ denotes position in a d-dimensional domain. The potential field is updated based on the densities until a self-consistent solution is reached. The most computationally expensive task is computing the chain propagator, which, for Gaussian chains, satisfies the modified diffusion equation (MDE):

$$\partial_s q(\boldsymbol{r}, s) = \left(\nabla^2 - w(\boldsymbol{r}, s)\right) q(\boldsymbol{r}, s) \tag{4.1}$$

Originally this equation was solved using a spectral method with a Galerkin approxi-

mation and symmetry-adapted plane-wave basis functions [13]. This method has spectral accuracy in space ($\boldsymbol{r}$), and is analytical in contour (s), but suffers from high computational cost due to the need to diagonalize a matrix to find the Fourier coefficients. The dimension of the matrix is the number of basis functions used, M, and the diagonalization is an $\mathcal{O}(M^3)$ operation. For three dimensional calculations with large cells or low symmetry, the matrix diagonalization becomes unfeasible because of the large number of basis functions needed and poor algorithm scaling.

There exist alternative, pseudo-spectral methods that have spectral accuracy in space ($\boldsymbol{r}$), polynomial accuracy in contour (s) and that can be solved with near-linear cost $\mathcal{O}(N_s M \ln M)$, where N_s is the number of contour points [14]. Two of the most common methods are those developed by Rasmussen and coworkers, [14, 15] and by Ranjan and coworkers [20], which are $\mathcal{O}(N_s^{-2})$ and $\mathcal{O}(N_s^{-4})$ accurate and which we abbreviate as RK2 and RQM4, respectively. Prior work has shown that although the RQM4 method is more accurate, RK2 is more efficient for some problems because of lower computational costs [25].

While these algorithms are representative of state-of-the-art methods, at strong segregation they need $\mathcal{O}(10^3)$ contour points for sufficient accuracy [19]. This can become intractable in very large cells or for systems with sharp interfaces where many spatial grid points are also necessary to resolve interfaces accurately. Recently, there has been work to obtain even higher accuracy in contour sampling by using a spectral deferred correction, but these methods are still limited to polynomial-order accuracy in contour [102]. An ideal algorithm would achieve spectral accuracy in the spatial and contour dimensions, while preserving the near-linear cost scaling of the pseudospectral methods. One way to achieve spectral accuracy in the contour domain is by using a Chebyshev polynomial expansion in s in eq 4.1, but this yields a non-sparse system of equations that cannot be solved efficiently.

An alternative, "coherent states" (CS) representation of polymer field theory has recently emerged [2], which is formally equivalent to the AF theory [103], but allows for different numerical methods that achieve spectral contour accuracy with linear scaling. Here we consider a canonical ensemble of incompressible molten diblock copolymers to illustrate the differences between the form of the two theories, then discuss numerical methods to solve each model. The ensemble contains n diblock chains, with species "A" volume fraction f in a volume V at temperature T.

The AF theory for a linear diblock copolymer is well documented in the literature, so we do not reproduce it here [1, 17]. We simply note that the theory consists of a pressure and exchange field, w_+ and w_-, that modulate incompressibility and a Flory χ interaction between dissimilar segments, respectively.

The details of how to convert an AF theory to a CS theory are given explicitly by Man and coauthors [42], and following their procedure yields the partition function

$$Z = \int \mathcal{D}w_+ \int \mathcal{D}w_- \int \mathcal{D}\phi_A \int \mathcal{D}\phi_A^* \int \mathcal{D}\phi_B \int \mathcal{D}\phi_B^* \exp(-\beta H_{CS}[w_+, w_-, \phi_A, \phi_A^*, \phi_B, \phi_B^*]) \tag{4.2}$$

$$\begin{aligned}\beta H_{CS} = \frac{n}{V}\Bigg[& \int d\boldsymbol{r} \left(\frac{w_-(\boldsymbol{r})^2}{\chi N} + w_-(\boldsymbol{r})(1-2f) - w_+(\boldsymbol{r}) \right) \\ & + \int_0^f ds \int d\boldsymbol{r}\ \phi_A^*(\boldsymbol{r},s) \left(\partial_s - \nabla^2 + w_+(\boldsymbol{r}) + w_-(\boldsymbol{r}) \right) \phi_A(\boldsymbol{r},s) \\ & + \int_0^{1-f} ds \int d\boldsymbol{r}\ \phi_B^*(\boldsymbol{r},s) \left(\partial_s - \nabla^2 + w_+(\boldsymbol{r}) - w_-(\boldsymbol{r}) \right) \phi_B(\boldsymbol{r},s) \\ & - V \ln \left(\frac{1}{V} \int d\boldsymbol{r}\ \phi_A^*(\boldsymbol{r},0) \phi_B^*(\boldsymbol{r},0) \right) - \int d\boldsymbol{r}\ \phi_A(\boldsymbol{r},f) - \int d\boldsymbol{r}\ \phi_B(\boldsymbol{r},1-f) \Bigg]\end{aligned} \tag{4.3}$$

where $\beta = 1/k_B T$ is the inverse thermal energy. In eq 4.3, the contour dimension, s,

has been scaled by the polymer length, N, and all positions, lengths, and volumes have been scaled by the unperturbed radius of gyration. All spatial integrals are over the system volume, V, and we choose periodic boundary conditions in the spatial dimension, $\boldsymbol{r}$. The coherent-states Hamiltonian, H_{CS}, is similar to the AF model Hamiltonian, but the single-chain partition function from the AF model has been replaced by explicit, semi-local terms containing the $(d+1)$-dimensional propagator-like fields ϕ_A, ϕ_A^*, ϕ_B and ϕ_B^* that generate the single chain statistics and architecture. Notably, the term involving $\phi_A^*(\boldsymbol{r},0)\phi_B^*(\boldsymbol{r},0)$ is a source to create A-B diblock junctions, while the final two terms terminate A blocks after f monomers and B blocks after $1-f$ monomers. The w_- field appears quadratically in the Hamiltonian, and could be integrated out of the theory, but we have found it advantageous to retain both w_- and ϕ, ϕ^* fields in developing our linear scaling methods. It should be noted that the functional integration paths of the w_+, ϕ_A^* and ϕ_B^* fields have been Wick rotated to the imaginary axis, rendering the exact theory deceivingly real.

To perform an SCFT calculation, we seek a saddle point with respect to the six fields that are arguments of H_{CS}. As is frequently done in the AF case, we perform a relaxation in fictitious time to reach the steady state saddle point [1, 42]. This time relaxation can in principle be augmented with appropriately distributed noise to perform a complex Langevin field theoretic simulation of the exact field theory [16, 42], but here we restrict consideration to the mean field approximation of SCFT. The relaxation equations are

$$\mu_1^{-1}\partial_t w_+(\boldsymbol{r},t) = -1 + \tilde{\psi}_A(\boldsymbol{r},t) + \tilde{\psi}_B(\boldsymbol{r},t) \tag{4.4}$$

$$\mu_2^{-1}\partial_t w_-(\boldsymbol{r},t) = -\frac{2w_-}{\chi N} - \tilde{\psi}_A(\boldsymbol{r},t) + \tilde{\psi}_B(\boldsymbol{r},t) + 2f - 1 \tag{4.5}$$

$$\mu_3^{-1}\partial_t\phi_A(\boldsymbol{r},s,t) = -\left(\partial_s - \nabla^2 + w_+(\boldsymbol{r},t) + w_-(\boldsymbol{r},t)\right)\phi_A(\boldsymbol{r},s,t) + \frac{V\delta(s)\phi_B^*(\boldsymbol{r},0,t)}{\int d\boldsymbol{r}\ \phi_A^*(\boldsymbol{r},0,t)\phi_B^*(\boldsymbol{r},0,t)} \tag{4.6}$$

$$\mu_3^{-1}\partial_t\phi_A^*(\boldsymbol{r},s,t) = -\left(-\partial_s - \nabla^2 + w_+(\boldsymbol{r},t) + w_-(\boldsymbol{r},t)\right)\phi_A^*(\boldsymbol{r},s,t) + \delta(f-s) \tag{4.7}$$

with analogous equations for ϕ_B and ϕ_B^*. The mobility parameters μ_1, μ_2, and μ_3 can be chosen to give the fastest numerical convergence. The volume fraction operators in the CS framework are

$$\tilde{\psi}_A(\boldsymbol{r},t) = \int_0^f ds\ \phi_A(\boldsymbol{r},s,t)\phi_A^*(\boldsymbol{r},s,t) \tag{4.8}$$

$$\tilde{\psi}_B(\boldsymbol{r},t) = \int_0^{1-f} ds\ \phi_B(\boldsymbol{r},s,t)\phi_B^*(\boldsymbol{r},s,t) \tag{4.9}$$

At steady state the AF and CS models reduce to precisely the same equations; however in AF theories we solve the MDE (eq 4.1) for the propagator at each time point, while in CS theories we update the propagator-like fields, ϕ_A, ϕ_A^*, ϕ_B, ϕ_B^*, in fictitious time according to eqs 4.6 and 4.7.

A successful alternative to the relaxation method is a fixed point iteration method with Anderson mixing (AM) applied to the w fields [24,104]. Although we do not employ (AM) in this work, it could be applied to both the CS and AF w-field saddle point searches instead of the relaxation algorithm. We do not expect the choice of w-field update algorithm to affect the relative performance of AF and CS methods, so long as the same method is used for each.

To solve the mean-field relaxation equations, we must specify a time discretization scheme. The simplest method uses an Euler discretization to update the potential fields,

w:

$$\frac{w_+^{j+1}(\boldsymbol{r}) - w_+^j(\boldsymbol{r})}{\mu_1 \Delta t} = -1 + \tilde{\psi}_A^j(\boldsymbol{r}) + \tilde{\psi}_B^j(\boldsymbol{r}) \tag{4.10}$$

$$\frac{w_-^{j+1}(\boldsymbol{r}) - w_-^j(\boldsymbol{r})}{\mu_2 \Delta t} = -\frac{2w_-^{j+1}(\boldsymbol{r})}{\chi N} - \tilde{\psi}_A^j(\boldsymbol{r}) + \tilde{\psi}_B^j(\boldsymbol{r}) + 2f - 1 \tag{4.11}$$

where the superscript j denotes the discrete time index.

We refer to eqs 4.10 and 4.11 as Euler time stepping. Previous work has shown that a far improved time stepping uses a semi-implicit Seidel (SIS) method [17], which can accelerate calculations by orders of magnitude. Unfortunately, existing SIS methods only apply to AF methods and not to CS theories because the volume fraction operators have a non-local time dependence on the potential fields in the latter case.

To complete the CS-SCFT method we require an algorithm to solve eqs 4.6 and 4.7. Previous authors reported a method with spectral accuracy in space and first order accuracy in contour by using a combination of Fourier transforms and finite differences (FD) [42]. We propose an alternative method that replaces the FD approximation with a Chebyshev-tau approximation in the contour dimension to obtain a scheme that has spectral accuracy in both space and contour [105]. Volume fraction operators can also be computed with spectral accuracy using Clenshaw-Curtis quadrature [106]. Importantly, this scheme has near-linear scaling in both the spatial and contour resolution via Fast Fourier Transform (FFT) algorithms. We explain the method using the ϕ_A equation, but it easily generalizes to the equations for all the propagator-like fields.

We first convert the source term to an effective boundary condition

$$\phi_A(\boldsymbol{r}, 0, t) = \frac{V \phi_B^*(\boldsymbol{r}, 0, t)}{\int d\boldsymbol{r}\ \phi_A^*(\boldsymbol{r}, 0, t) \phi_B^*(\boldsymbol{r}, 0, t)} \tag{4.12}$$

We next define a Chebyshev expansion for ϕ_A

$$\phi_A(\boldsymbol{r}, s, t) = \sum_{n=0}^{N_s} a_n(\boldsymbol{r}, t) T_n\left(\frac{2s}{f} - 1\right) \tag{4.13}$$

$$T_n(\cos(\nu)) = \cos(n\nu) \tag{4.14}$$

If we discretize the contour along the Chebyshev nodes, $s_j = f(1 - \cos(j\pi/N_s))/2$, $j = 0, 1, \ldots, N_s$, then ϕ_A can be computed from the Chebyshev coefficients, a_n, using the Discrete Cosine Transform (DCT):

$$\phi_A(\boldsymbol{r}, s_{N_s-j}, t) = \sum_{n=0}^{N_s} a_n(\boldsymbol{r}, t) \cos(jn\pi/N_s) \tag{4.15}$$

Substituting the expansion into eq 4.6 and using the properties of Chebyshev polynomials and Fourier transforms we obtain for $0 \leq n \leq N_s - 3$

$$\begin{aligned} \left(\mu_3^{-1}\partial_t + k^2\right) c_n \hat{a}_n(\boldsymbol{k}, t) + \frac{4}{f}(n+1)\hat{a}_{n+1}(\boldsymbol{k}, t) - \left(\mu_3^{-1}\partial_t + k^2\right) \hat{a}_{n+2}(\boldsymbol{k}, t) \\ = -\mathcal{F}_{\boldsymbol{r}}\{(w_+(\boldsymbol{r}, t) + w_-(\boldsymbol{r}, t))(c_n a_n(\boldsymbol{r}, t) - a_{n+2}(\boldsymbol{r}, t))\} \end{aligned} \tag{4.16}$$

and for $N_s - 2 \leq n \leq N_s - 1$

$$\left(\mu_3^{-1}\partial_t + k^2\right) \hat{a}_n(\boldsymbol{k}, t) + \frac{4}{f}(n+1)\hat{a}_{n+1}(\boldsymbol{k}, t) = -\mathcal{F}_{\boldsymbol{r}}\{(w_+(\boldsymbol{r}, t) + w_-(\boldsymbol{r}, t))a_n(\boldsymbol{r}, t)\} \tag{4.17}$$

where $\mathcal{F}_{\boldsymbol{r}}\{a_n(\boldsymbol{r}, t)\} = \hat{a}_n(\boldsymbol{k}, t)$ is the Fourier transform in space. The coefficient $c_n = 1$ for $n \neq 0$ and $c_0 = 2$. Time discretization with semi-implicit forward Euler and defining $\mu_3 \Delta t = \Delta t'$ yields for $0 \leq n \leq N_s - 3$

$$\left(1 + k^2\Delta t'\right) c_n \hat{a}_n^j(\boldsymbol{k}) + \frac{4\Delta t'}{f}(n+1)\hat{a}_{n+1}^j(\boldsymbol{k}) - \left(1 + k^2\Delta t'\right) \hat{a}_{n+2}^j(\boldsymbol{k})) = c_n f_n^j(\boldsymbol{k}) - f_{n+2}^j(\boldsymbol{k}) \tag{4.18}$$

and for $N_s - 2 \leq n \leq N_s - 1$

$$\left(1 + k^2 \Delta t'\right) \hat{a}_n^j(\boldsymbol{k}) + \frac{4\Delta t'}{f}(n+1)\hat{a}_{n+1}^j(\boldsymbol{k}) = f_n^j(\boldsymbol{k}) \tag{4.19}$$

with

$$f_n^j(\boldsymbol{k}) = \mathcal{F}_{\boldsymbol{r}}\{[1 - \Delta t'(w_+^j(\boldsymbol{r}) + w_-^j(\boldsymbol{r}))]a_n^{j-1}(\boldsymbol{r})\} \tag{4.20}$$

combining eqs 4.18 - 4.20 with the boundary condition

$$\sum_{n=0}^{N_s} \hat{a}_n^j(\boldsymbol{k})(-1)^n = \frac{V\mathcal{F}_{\boldsymbol{r}}\{\phi_B^{*j-1}(\boldsymbol{r},0)\}}{\int d\boldsymbol{r}\ \phi_A^{*j-1}(\boldsymbol{r},0)\phi_B^{*j-1}(\boldsymbol{r},0)} \tag{4.21}$$

yields a bordered tri-diagonal system for each Fourier mode, $\boldsymbol{k}$. Each system can be solved in $\mathcal{O}(N_s)$ operations, resulting in $\mathcal{O}(N_s M)$ operations to solve the global system. The original propagator can be obtained via a fast DCT in contour ($\mathcal{O}(N_s M \ln N_s)$ operations) followed by a FFT in space ($\mathcal{O}(N_s M \ln M)$ operations). After updating propagators and converting from Fourier-Chebyshev space to real-contour space, volume fraction operators are computed using Clenshaw-Curtis quadrature [106]. Finally, we update the interaction fields according to the Euler potential update scheme (eqs 4.10 and 4.11).

To compare this new CS-Chebyshev method to AF methods (RK2 and RQM4) and the previously reported FD method for CS theories, we computed the SCFT intensive Hamiltonian, $\beta H/n$, of a symmetric ($f = 0.5$) diblock copolymer in a one-dimensional cell with length 4 R_g at $\chi N = 15$ and $\chi N = 80$. In all cases, the relaxation was run until the l_2 norm of $\delta H/\delta w_+$ and $\delta H/\delta w_-$ were both less than the tolerance, λ_f, but we omit the $k = 0$ mode of $\delta H/\delta w_+$ to which the theory is invariant. Numerical parameters such as time step and mobilities were tuned to just below their stability thresholds. We use a Chebyshev method calculation with $N_s = 500$ as the reference value for the intensive Hamiltonian and run time.

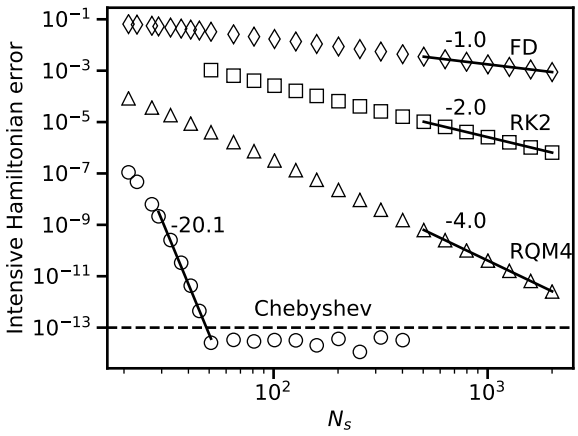

Figure 4.1: Comparison of intensive Hamiltonian error with number of contour samples for each contour method. Computed at $\chi N = 15$ and $f = 0.5$ with $M = 32$ spatial grid points. Horizontal dash line indicates force cutoff, $\lambda_f = 10^{-13}$.

We first examine the error scaling with N_s for each method. Figure 4.1 shows that the FD, RK2, and RQM4 methods have the expected asymptotic error scaling slopes of -1, -2, and -4, respectively. Although the Chebyshev method was fit with a line to illustrate the rapid convergence with N_s, the points are not linear on the log-log plot because of the spectral accuracy.

The Chebyshev method has greatly improved accuracy and scaling compared to the other methods, shown by the lower error and much steeper slope. The method is so accurate that the error saturates to the force tolerance, λ_f, with only 51 contour points. The high accuracy with few contour samples represents a potential huge memory savings in large scale numerical computations.

We now discuss the computational speed of each method. We present results in terms of efficiency: the computation time taken to reach a given level of accuracy in the intensive Hamiltonian. The appropriate accuracy level will vary between applications, but resolving phase boundaries can require $\mathcal{O}(10^{-6})$ accuracy in the SCFT intensive Hamiltonian [19, 39]. While the previous results did not differentiate between time stepping

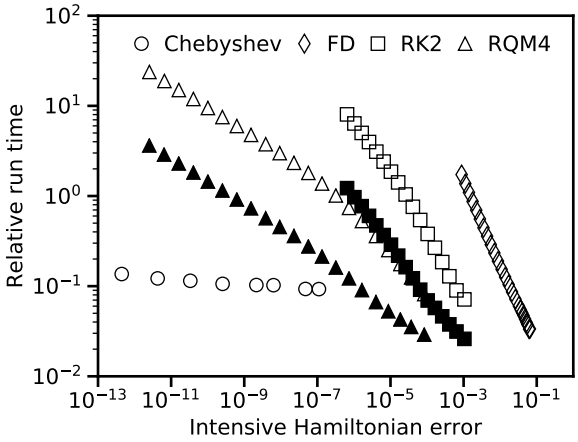

Figure 4.2: Comparison of relative run time with intensive Hamiltonian error for each contour method. Computed at $\chi N = 15$ and $f = 0.5$ with $M = 32$ spatial grid points. Open symbols use Euler time stepping. Solid symbols use SIS time stepping. Error bars are within the symbol size.

methods, here we present results for both the Euler and SIS time stepping methods for the AF theories. It is important to compare different contour methods using the same w-field time stepping algorithm, which isolates the effect of contour accuracy, but it is also useful to compare the new CS methods that use Euler time stepping versus the AF-SIS methods, which represent the current standard in polymer SCFT. Figure 4.2 shows efficiency curves for each method when applied to a symmetric diblock at $\chi N = 15$.

For calculations that use Euler time stepping (open symbols), the Chebyshev method shows the best efficiency. For fixed small values of intensive Hamiltonian error, the Chebyshev method is an order of magnitude faster than any other method. SIS time stepping (solid symbols) speeds up the AF calculations by approximately an order of magnitude, but this does not make them more efficient than the Chebyshev method over the relevant ranges of intensive Hamiltonian error. For large values of the intensive Hamiltonian error ($> 10^{-5}$) where the Chebyshev method is not applicable because no N_s returned such a large error, the AF-SIS methods are faster than the Chebyshev-Euler method. There thus remains a niche for AF-SIS calculations where significant accuracy

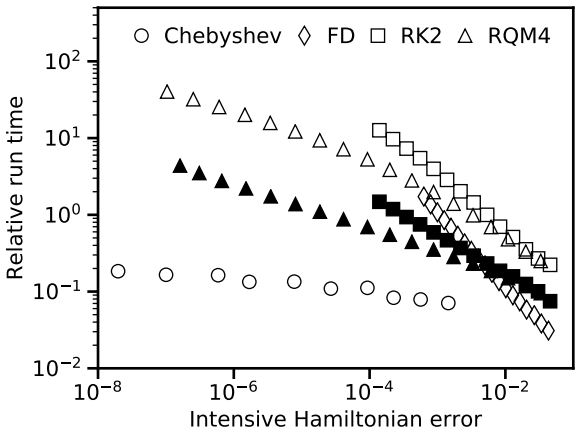

Figure 4.3: Comparison of relative run time with intensive Hamiltonian error for each contour method. Computed at $\chi N = 80$ and $f = 0.5$ with $M = 256$ spatial grid points. Open symbols use Euler time stepping. Solid symbols use SIS time stepping. Error bars are within the symbol size.

can be sacrificed for speed.

We note, however, that there has been much more work to date on AF theories than CS theories. Although the SIS time stepping method is not applicable to CS theories, there are other techniques such as Anderson mixing that could be used to improve w-field iteration [24]. Combining fictitious time relaxation of ϕ fields with AM on w fields could potentially yield the most efficient algorithm for *all* ranges of accuracy.

We next consider a strongly segregated symmetric diblock with $\chi N = 80$. Previous work has shown that high accuracy is essential to successfully converge SCFT calculations under these conditions [19], so we expect the Chebyshev method to outperform the other methods. Results are presented in Figure 4.3.

The Chebyshev method again is the most efficient method at a fixed level of intensive Hamiltonian error, regardless of time stepping method. Contrary to the $\chi N = 15$ case, the AF-SIS methods do not provide a fast, low accuracy alternative to the Chebyshev method: low accuracy AF-SIS calculations take just as long as high accuracy Chebyshev calculations. For applications where high accuracy is necessary, the Chebyshev method

thus offers a large improvement over existing methods.

In this letter we have shown that CS field theories can offer numerical advantages over traditional approaches to SCFT. Although they are formally equivalent, coherent states theories allow for fully spectral, linear scaling numerical methods, which enable much more accurate simulations at lower memory cost and faster speeds than AF methods. Although not discussed in this work, CS theories can also be applied to a wide range of polymer systems, such as systems with three or more components, arbitrary architecture, and supramolecular chemistries that cannot be effectively treated with AF models [43]. We expect that the numerical and theoretical advantages of CS theories over AF theories will allow for previously intractable problems to now be tackled.

4.1 Acknowledgements

This work was supported by the NSF Condensed Matter and Materials Theory Program under DMR-182215. Extensive use was made of the Center for Scientific Computing from the CNSI, MRL: an NSF MRSEC (DMR-1720256) and NSF CNS-1725797. D.L.V. acknowledges support from the NSF Graduate Research Fellowship Program under Grant No. 1650114.

Chapter 5

Binary Blends of Telechelic Homopolymers

5.1 Introduction

Block copolymers (BCPs) are a major industrially platform due to their highly tunable properties via self assembly and the ability to compatibilize dissimilar polymers. A major triumph of polymer physics is the ability to predict when melts or solutions of homopolymers and copolymers will mix into a single liquid, macroscopically phase separate into two liquids [107, 108] or self assemble into a solid-like microstructure [4]. One important tool for predicting this phase behavior is numerical self-consistent field theory (SCFT) which is particularly effective at computing free energies of the self-assembled microstructures [13]. Numerical advances over the last 30 years have enabled efficient simulation of complex self-assembled structures, including aperiodic bricks-and-mortar phases [109] and Frank-Kasper sphere phases [33, 82]. The standard approach for numerical SCFT uses an auxiliary field (AF) based model, which decouples chain interactions via a set of local chemical potential fields [13]. This approach is well suited to polymer

systems with a pre-defined distribution of components in the mixture, or "quenched" systems [1]. In recent years, however, there has been significant interest in supramolecular interactions, where polymers and small-molecules can form and dissociate bonds reversibly and are in a dynamic equilibrium. These types of interactions appear in both synthetic and biological polymers, including intrinsically disordered proteins [110] and polymers functionalized with acid and base groups [111, 112], multiple hydrogen bonds [113], and ligands that bind to metals [114]. Supramolecular interactions are also of industrially interest, as thermoplastic polyurethanes are BCPs composed of urethane linkages that can reversibly dissociate at elevated temperatures [46–48]. Supramolecular interactions can also lead to exotic phase behavior, including re-entrant phase transitions [115], and can also be leveraged to make thermally tunable [112] and self-healing materials [116].

There have been attempts to extend the AF-SCFT approach to supramolecular polymers [44, 117–121]. For systems in which only a finite set of products can be formed, the approach works well. One example is a supra-diblock system in which two dissimilar homopolymers each have one functional group on a chain end that can link together to form a diblock [118]. In many systems, however, there are an infinite number of possible products. This includes telechelic and network forming polymers. For these systems with infinite products, the AF-SCFT approach relies on closure approximations to account for all the different products and neglects ring and loop formation [121]. Even with these approximations, the approach is limited by computational expense and has not be used to study the complex microphases discussed earlier [44].

Recent theoretical developments have produced an alternative to the AF approach that instead represents polymers via coherent states (CS) fields [42]. These CS models are particularly effective for supramolecular systems as they can represent all possible reaction products with the proper weighting even when there is an infinite number of products [43]. The models are finite order in the CS fields and do not rely on any closure

approximations. Recent numerical advances have enabled efficient simulation of these models as well [70], though these algorithms have not yet been applied to supramolecular polymers. In this work we combine the theoretical and numerical advances to demonstrate that CS-SCFT can be used to construct full phase diagrams and reaction equilibrium for supramolecular polymers. As a model system we consider a binary blend of telechelic homopolymers that can form AB type bonds in a heterobonding scheme. This system can form arbitrarily long alternating AB type block copolymers, which makes it intractable to AF-SCFT calculations. The full CS theory also accounts for ring polymers that can be formed, but the mean field approximation invoked for SCFT does not account for these products [122]. We compute full phase diagrams that include phase coexistence between disordered phases and microphases, including the BCC sphere phase and double gyroid network phase. These phases require three dimensional calculations, which have not been performed for supramolecular block copolymers before.

With our approach we are able to demonstrate three different regimes of phase behavior depending on the relative strength of the bond equilibrium and the phase segregation strength. When bonds are weak, the system behaves similarly to a non-reactive polymer blend. In the opposite limit, when bonds are strong the system behaves like a pure block copolymer melt, or block copolymer-homopolymer blend depending on the stoichiometry of the system. In the intermediate regime, we observe a complex interplay between macroscopic phase separation and microphase segregation characteristic of the region around a Lifshitz point. In addition to phase diagrams, we are able to predict the reaction equilibrium in the system as well as microphase structure, including domain spacing. These results demonstrate the range of possible phase behavior and will help guide experimental polymer chemists who are using supramolecular chemistry in polymer blends.

5.2 Model and Methods

A CS model for a binary blend of heterobonding telechelic homopolymers in the canonical ensemble is

$$Z = Z_0 \int \mathcal{D}w_+ \int \mathcal{D}w_- \int \mathcal{D}(\phi_A, \phi_A^*) \int \mathcal{D}(\phi_B, \phi_B^*) e^{-H[w_+, w_-, \phi_A, \phi_A^*, \phi_B, \phi_B^*]} \tag{5.1}$$

$$\begin{aligned} H = {} & \frac{\rho_0}{\chi} \int d\boldsymbol{r}\, (w_-(\boldsymbol{r}))^2 - \rho_0 \int d\boldsymbol{r}\, w_+(\boldsymbol{r}) \\ & - \sum_{K \in \{A,B\}} n_K \ln \left(\frac{1}{V} \int d\boldsymbol{r}\, (\phi_K^*(\boldsymbol{r}, 0))^2 \right) \\ & + \sum_{K \in \{A,B\}} \int ds \int d\boldsymbol{r}\, \phi_K^*(\boldsymbol{r}, s) \left(\partial_s - \frac{b_K^2}{6} \nabla^2 + w_K(s) \right) \phi_K(\boldsymbol{r}, s) \\ & - \sum_{K \in \{A,B\}} \int d\boldsymbol{r}\, \phi_K(\boldsymbol{r}, N_K/2) - \frac{K_b}{\rho_0} \int d\boldsymbol{r}\, \phi_A(\boldsymbol{r}, N_A/2) \phi_B(\boldsymbol{r}, N_B/2) \end{aligned} \tag{5.2}$$

Here Z is the partition function, Z_0 is the ideal gas partition function, and H is the effective Hamiltonian. Normalizing denominators for the functional integrals have been absorbed into Z_0. The Hamiltonian depends on four CS fields (ϕ_A,ϕ_A^*,ϕ_B,ϕ_B^*) and two AF fields (w_+,w_-), so the model may be referred to as a hybrid AF-CS model. The AF fields are defined over all of space $\boldsymbol{r}$, whereas the CS fields depend on $\boldsymbol{r}$ as well as the chain contour position, s. Each term in the Hamiltonian has a simple physical interpretation. The logarithmic terms on the second line create the appropriate number of homopolymer precursor chains, n_A or n_B, depending on species. The terms contain factors of $(\phi^*(\boldsymbol{r}, 0))^2$ which creates two polymer arms at the zero contour position. The third line of the Hamiltonian is responsible for propagating these arms forward in s using the appropriate chain statistics. In this work we consider flexible continuous Gaussian chains, which leads to the diffusive-type operator $\partial_s - \nabla^2$ that appears in the Hamiltonian. The statistical segment length can be set for each species via b_K, but we only consider

$b_A = b_B = 1$ in this work. While the chain is being propagated it experiences the relevant potential field w_A or w_B, which are related to the $w_\pm$ auxiliary fields via a simple linear transformation

$$w_A = w_+ - w_- \tag{5.3}$$

$$w_B = w_+ + w_- \tag{5.4}$$

After $N_K/2$ segments the chain is terminated via the first term in the last line. Because the polymer was initialized as a star with two arms, this creates a linear chain with total length N_K. Unless otherwise specified, we choose $N_A = N_B$. The final term in the Hamiltonian enables an A and a B polymer to link together at their chain ends and has an associated equilibrium constant K_b. In addition to creating the diblock, this terms also creates all higher order products as well, including triblock, tetrablock and so on. Finally, the first two terms in the model represent the non-bonded interactions between polymer segments in the model. The first introduces a Flory-Huggins interaction between A and B segments parameterized by χ and the second enforces incompressibility at a segment number density $\rho_0 = (n_A N_A + n_B N_B)/V$, where V is the total volume of the system. It is possible to remove the AF fields and replace the first two terms in the model with fourth order terms in the CS fields, to create a "pure" CS model [42,43], however previous work has found the hybrid model more easily simulated numerically [70]. Although we have presented the model here based on physical arguments, it is possible to derive it rigorously from an AF model which is demonstrated in the literature [42]. Correspondingly, it is possible to show that every product is accounted for correctly by performing a perturbation expansion of the CS fields.

As a final note it is worth discussing the relationship between the model parameters and experimentally controllable parameters. In the model, polymer segments are defined

to have equal volume, so the volume fraction of a given segment type (A or B) is $\psi_K = n_K N_K / V$. Two model parameters are related to temperature: χ and K_b. For polyolefins, the chi parameter can typically be fit to an expression of the form

$$\chi = C_1 + C_2/T \tag{5.5}$$

where T is temperature and C_1 and C_2 are constants fit from scattering data.

The equilibrium constant follows the relation

$$K_b = \exp\left(\frac{\epsilon_b - s_b k_B T}{k_B T}\right) \tag{5.6}$$

where k_B is Boltzmann's constant, ϵ_b is the enthalpy of reaction, and s_b is the entropy of reaction. We assume for simplicity that both ϵ_b and s_b are independent of temperature.

The model presented above can be applied to any experimental system for which there is a known temperature dependence for χ and K_b. In this work, rather than specialize to specific chemistries we instead make an approximation to examine general trends. We assume that χ is inversely proportional to temperature ($C_1 = 0$ in eq 5.5) and that the entropy of reaction $s_b = 0$. With these approximations, χ and $h = \ln(K_b)$ are both inversely proportional to temperature and their ratio is independent of temperature. This allows us to use χ as an inverse temperature scale and h/χ as a chemistry-dependent property that controls how strong bonding is compared to phase segregation [118, 119].

As a final note, it is convention in unreactive block copolymers to specify χN rather than χ as it is the combined grouping that controls phase behavior for linear chains. This is no longer true in the telechelic model considered here, as the reaction can only occur at end groups. Changing N_A or N_B changes the concentration of these end groups, breaking the universal phase behavior for fixed χN. Nevertheless, to match convention we will

use the combined grouping χN_A and $h/\chi N_A$ and fix $N_A = 100$. Although this reduces the generality of the results presented here, it is well understood how changing N affects phase behavior and reaction equilibrium based on previous literature results [118].

We now turn to physical observables that can be computed via field operators. The first of these is the segment density of the A or B species:

$$\tilde{\rho}_K(\boldsymbol{r}) = \int ds\, \phi_K^*(\boldsymbol{r}, s)\phi_K(\boldsymbol{r}, s) \tag{5.7}$$

a similar quantity that only considers the end segments of a chain can also be defined as an end density

$$\tilde{\rho}_{K,e}(\boldsymbol{r}) = \phi_K(\boldsymbol{r}, N_K/2) \tag{5.8}$$

Finally an operator that shows the local density of bonds is defined via

$$\tilde{\rho}_b(\boldsymbol{r}) = \phi_A(\boldsymbol{r}, N_A/2)\phi_B(\boldsymbol{r}, N_B/2) \tag{5.9}$$

These operators give important information about the spatial distribution of segments in the system. We are also concerned with bulk properties as well, including the total number of bonds

$$n_b = \left\langle \int d\boldsymbol{r}\, \phi_A(\boldsymbol{r}, N_A)\phi_B(\boldsymbol{r}, N_B) \right\rangle \tag{5.10}$$

and number of unreacted ends of a given species in the system

$$n_{K,e} = \left\langle \int d\boldsymbol{r}\, \phi_K(\boldsymbol{r}, N_K) \right\rangle \tag{5.11}$$

A useful quantity to consider is the conversion of end groups, which is defined as

$$\alpha_K = \frac{2n_K - n_{K,e}}{2n_K} = \frac{n_b}{2n_K} \tag{5.12}$$

The conversion of end groups for species A and B are related because only AB type bonds can form:

$$\frac{\alpha_A \psi_A}{N_A} = \frac{\alpha_B \psi_B}{N_B} \tag{5.13}$$

The internal stress of a blend can also be computed via field operator. Such an operator is familiar in AF representations, and has a similar form in the CS model. The full derivation of such an operator can be found in the supporting information of a recent publication by Fredrickson and Delaney [123], so we present the final result:

$$\tilde{\boldsymbol{\sigma}} = \sum_{K \in \{A,B\}} \int d\boldsymbol{r} \int ds\, \phi_K(\boldsymbol{r}, s) \nabla\nabla \phi_K^*(\boldsymbol{r}, s) \tag{5.14}$$

A final important operator is the chemical potential, which is required to construct phase coexistence regions. For a given species the excess chemical potential is

$$\mu_{K,\mathrm{ex}} = -\ln\left(\frac{1}{V}\int d\boldsymbol{r}\, (\phi_K^*(\boldsymbol{r}, 0))^2\right) \tag{5.15}$$

This chemical potential is in excess of the ideal gas chemical potential.

The previously discussed operators give average information about the reaction equilibrium, such as the conversion, but we would also like to know the distribution of products in the system, including how much of each type of block copolymer is formed. Unfortunately, there is not a known operator using the CS fields that can be used to compute the number of each type of reaction product. It is possible, however, to compute the number of chains of a given species in an AF model of a grand canonical ensemble. The

effective Hamiltonian for an AF model of the telechelic blend presented here is

$$\begin{aligned} H_{\mathrm{AF}}[w_+, w_-] = \frac{\rho_0}{\chi} \int d\boldsymbol{r}\, (w_-(\boldsymbol{r}))^2 - \rho_0 \int d\boldsymbol{r}\, w_+(\boldsymbol{r}) - \sum_{j=1}^{\infty} z_{A_j B_j} V Q_{A_j B_j}[w_+, w_-] \\ - \sum_{j=1}^{\infty} \left(z_{A_j B_{j-1}} V Q_{A_j B_{j-1}}[w_+, w_-] + z_{A_{j-1} B_j} V Q_{A_{j-1} B_j}[w_+, w_-] \right) \\ - \sum_{j=1}^{\infty} \left(z_{A_j B_j, r} V Q_{A_j B_j, r}[w_+, w_-] \right) \end{aligned} \tag{5.16}$$

and the number of each product can be computed via

$$n_{A_j B_k} = \langle z_{A_j B_k} V Q_{A_j B_k}[w_+, w_-] \rangle \tag{5.17}$$

The first two terms of the effective Hamiltonian are equivalent to the CS model and represent Flory interactions and incompressibility. The remaining terms contain activities z and single chain partition functions $Q[w_+, w_-]$ for all the possible products that can be formed. The activities and single chain partition functions are also used to compute the number of each product. The products can be classified into three types: linear chains that are composed of an equal number of A and B chains and are terminated by one A chain and one B chain, linear chains with one excess A or B chain and that are doubly A or B terminated, and ring polymers, which must have an equal number of A and B chains. One can demonstrate that the activity of each type of chain can be related to the activity of the A and B homopolymers, z_A and z_B, and the equilibrium constant K_b via

$$z_{A_i B_j} = \begin{cases} (2z_A)^i (2z_B)^j K_b^{i+j-1} & i = j, \text{linear} \\ \frac{1}{2} (2z_A)^i (2z_B)^j K_b^{i+j-1} & |i - j| = 1 \\ \frac{1}{2j} (2z_A)^i (2z_B)^j K_b^{i+j} & i = j, \text{ring} \end{cases} \tag{5.18}$$

the cases of this equation represent the different types of products discussed previously. The first two cases which represent different types of linear chains are nearly identical, only differing by a factor of 2. The products that are doubly A terminated or doubly B terminated are head-tail symmetric, so their activity carries a factor of $\frac{1}{2}$ to account for this degeneracy. Similarly for ring polymers there is a factor of $\frac{1}{2j}$ that accounts for the rotational symmetry of the molecule. There is also an additional factor of K_b that accounts for the extra bond in a ring compared to a linear chain.

Although we have obtained the activities of each product, we still require the activities of the homopolymers and also the values of the single chain partition functions to compute the number of each product. The homopolymer activities can be computed from the chemical potential determined from canonical ensemble simulations with the CS model since $z_A = \exp(\mu_A)$. All that remains then is to compute the ensemble average single chain partition function value for each chain. This would normally be prohibitively expensive since there are an infinite number of chains. We circumvent this issue by only considering products of up to 14 homopolymers. One can evaluate how much of the mass is accounted for with this truncation by comparing the total number of polymers from the original CS canonical simulation and comparing it to the number of products computed from the AF approach. In all cases in this work, the error is less than half a percent unless otherwise noted.

The distribution calculation in this work is further accelerated by the fact that we limit ourselves to self-consistent field theory calculations and only must evaluate each Q at the final saddle point value. We discuss details of the numerical SCFT method in the following section. For the disordered phase, numerical simulations are not required and the single chain partition function can be computed analytically under SCFT. Additionally, in the disordered phase the activity of the A and B homopolymers can be related to the system composition analytically. We can then analytically compute the distribution

of products in the disordered phase, neglecting rings, which yields

$$\alpha_K = \frac{1 + \frac{1}{2}K_b\left(\frac{\psi_A}{N_A} + \frac{\psi_B}{N_B}\right) - \sqrt{1 + K_b\left(\frac{\psi_A}{N_A} + \frac{\psi_B}{N_B}\right) + \frac{1}{4}K^2\left(\frac{\psi_A}{N_A} - \frac{\psi_B}{N_B}\right)^2}}{\frac{\psi_K}{N_K}K_b} \tag{5.19}$$

$$\psi_{A_jB_{j-1}} = (1-\alpha_A)^2(\alpha_A\alpha_B)^{j-1}\psi_A\left(\frac{jN_A + (j-1)N_B}{N_A}\right) \tag{5.20}$$

$$\psi_{A_{j-1}B_j} = (1-\alpha_B)^2(\alpha_A\alpha_B)^{j-1}\psi_B\left(\frac{(j-1)N_A + jN_B}{N_B}\right) \tag{5.21}$$

$$\psi_{A_jB_j} = 2(1-\alpha_A)(1-\alpha_B)(\alpha_A\alpha_B)^{j-1}\alpha_A\psi_A\frac{N_A + N_B}{N_A} \tag{5.22}$$

eq 5.19 gives the conversion of species A or B in the disordered phase while eqs 5.20–5.22 give the volume fraction of the different types of products that can be formed. The three types of products include A-terminated chains, B-terminated chains, and chains terminated with one A and one B macromonomer. Note that SCFT does not account for rings. One can show via an infinite summation that the volume fraction add to one analytically, indicating that we have properly accounted for all products. The compositions are consistent with a probabilistic interpretation of the product distribution. In the disordered state the system is well mixed, so the probability that an A chain end is reacted is α_A and the probability that it is unreacted is $(1-\alpha_A)$. The probability that an A macromonomer has two unreacted ends is then $(1-\alpha_A)^2$, which is proportional to the amount of unreacted homopolymer in the blend, consistent with eq 5.20. To form an AB diblock requires an A macromonomer with one unreacted end and one reacted end, generating the weight $2\alpha_A(1-\alpha_A)$, where the factor of two accounts for the indistinguishability of the two ends. The reacted end must be linked to a B block, which then has its other end unreacted which is associated with a factor of $(1-\alpha_B)$. The volume fraction of an AB diblock should then be proportional to $2\alpha_A(1-\alpha_A)(1-\alpha_B)$ which is also consistent with eq 5.22. One can extend this logic to higher order products

such as an ABA triblock and find that the expected factor of $(1-\alpha_A)^2\alpha_A\alpha_B$ is properly accounted for in eq 5.20.

5.2.1 Numerical Self Consistent Field Theory

Numerical self-consistent field theory is an approximation to the full model in which we only consider a single saddle point configuration that satisfies the equations

$$\frac{\delta H}{\delta w(\boldsymbol{r})} = \frac{\delta H}{\delta \phi_K^*(\boldsymbol{r})} = \frac{\delta H}{\delta \phi_K(\boldsymbol{r})} = 0 \tag{5.23}$$

The free energy of the system is equal to the value of the effective Hamiltonian evaluated at these saddle point field configurations.

To obtain the saddle point fields, we use a previously developed algorithm [70]. The simulations are conducted in orthorhombic unit cells with periodic boundary conditions. The phases considered in this work are disordered liquid (DIS), lamellae (LAM), hexagonally-packed cylinders (HEX), BCC spheres (BCC), and double gyroid network (GYR). It is possible that other phases such as Frank-Kasper sphere packings may occur, but we do not consider them here. The three dimensional phases, BCC and GYR, were spatially discretized using a 64^3 mesh while the two dimensional HEX phase was discretized with a 64 by 108 grid and the one dimensional LAM phase used 64 grid points. In all calculations the polymer contour was discretized with 11 sample points on a Chebyshev grid along the range $[0, N_K/2]$ for each polymer. All calculations were run until first variation of the Hamiltonian was less than 10^{-7} with respect to all fields. A variable cell shape algorithm was employed to obtain stress free configurations [93], but using the CS stress operator presented earlier. All calculations were run until the stress was less than 10^{-6}.

5.2.2 Gibbs Ensemble

For the blend system considered here, it is possible to separate into multiple phases. Using Gibbs phase rule it is possible to demonstrate that a maximum of two phases can be formed, as there are two starting macromonomers and every other component is formed via reaction from these. To determine binodals of phase coexistence we use the Gibbs ensemble approach pioneered by Panagiotopoulos in the context of particle simulations [124,125]. The Gibbs ensemble approach was later adapted to field theoretic simulations by Riggleman and coworkers [126], and eventually specialized to SCFT of incompressible blends by Mester and coauthors [127,128]. We employ the Gibbs ensemble method of Mester in this work. In a Gibbs ensemble, the system is divided into two subsystems with each containing a different phase. The temperature, number of polymers, and the total volume of the system are fixed. We adjust the composition and volume of each subsystem to equalize the osmotic pressure and chemical potential between the two subsystems, subject to the mass and volume conservation constraints of the total system. This approach only requires one calculation per temperature along each binodal, in contrast to other approaches such as common tangent or grand canonical ensemble that require many calculations [129].

5.3 Results and Discussion

5.3.1 Weak bonding

We first examine a case where bonding is weak compared to phase separation and set $h/\chi N_A = 0.5$. Figure 5.1 shows the phase in the space of χN_A, which is proportional to inverse temperature, and volume fraction of A segments ψ_A. The phase diagram is dominated by a region of phase coexistence between an A-rich disordered liquid and a

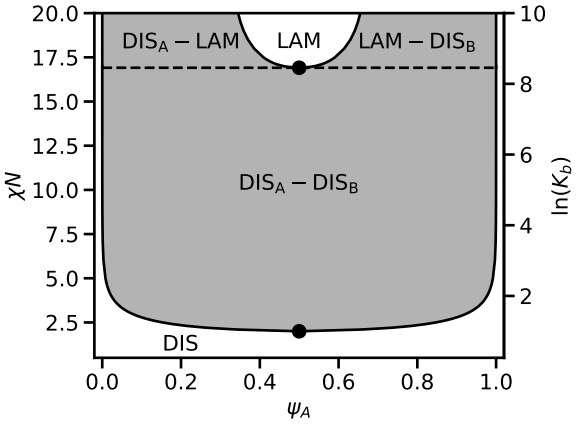

Figure 5.1: Phase diagram for a binary blend of heterobonding telechelic homopolymers at $h/\chi N = 0.5$. Shaded regions indicated two phase coexistence, while white areas indicate a single phase. Critical points are indicated with solid dots.

B-rich disordered liquid. This is very reminiscent of an unreactive homopolymer binary blend, and the critical point in the reactive system is quite close to that of the unreactive system ($\chi N = 2.0$, $\psi_A = 0.5$). At sufficiently high χN a region emerges where the lamellar phase is stable, which is flanked by regions of coexistence with disordered phases. Because the ratio of $h/\chi N$ is fixed, increasing χN also increases the equilibrium constant, favoring block copolymer product formation.

To better understand the phase behavior, it is useful to examine the reaction equilibrium in the blend. Figure 5.2 shows the conversion of species A as χN is varied at fixed total composition $\psi_A = 0.5$. Because the system is symmetric, at this composition $\alpha_A = \alpha_B$, so we only plot one. The figure shows that below the critical point near $\chi N = 2$ the conversion is quite low ($\mathcal{O}(10^{-3})$), but increases with increasing χN. This trend reverses at the critical point, however, and increasing χN decreases the conversion in the system up until $\chi N = 16.9$. We attribute this to the increasing strength of phase segregation in this region. The conversion decreases because as χN increases there are fewer and fewer B chains present in the A-rich domain with which A chains can react. Finally, at $\chi N = 16.9$ the lamellar phase forms and there is a sudden increase in the con-

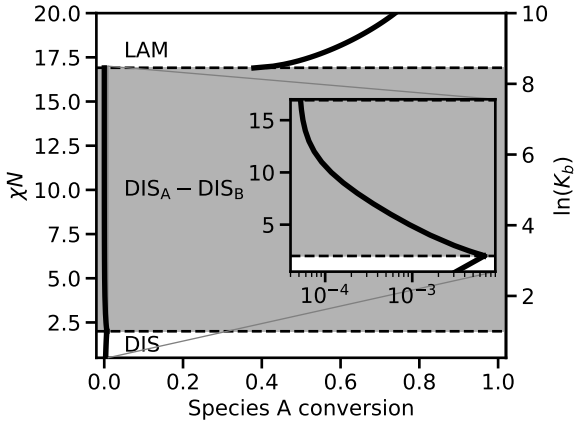

Figure 5.2: Conversion of species A, α_A, at $h/\chi N = 0.5$ and $\psi_A = 0.5$. The shading and text labels indicate the stable phase(s).

version. The equilibrium constant K_b has increased enough that it is now energetically favorable to remix the two liquids so that they can form block copolymers which then self assemble into a lamellar structure. There is still a significant amount of homopolymer in the mixture, but it can segregate to the interior of the A and B domains while the block copolymers act like surfactants at the interface.

Just past the critical point, domain spacing of the lamellar phase is quite large ($8\,R_g$) compared to a lamellar domain formed from pure AB diblocks ($3.9\,R_g$), as shown in Figure 5.3. For volume fraction of A less than 0.35 or greater than 0.65 the system undergoes phase separation between the lamellar phase and a disordered phase. The disordered phase is composed almost entirely of the majority component of the system, and contains almost purely homopolymers and almost no block copolymer. Rather than swell the lamellar domain with all the excess homopolymer that exists because of stoichiometry, it is instead favorable to eject it into a separate phase and maintain a less swollen lamellar phase. Because our calculations invoke a mean field approximation, there are no Helfrich repulsions that would allow unbinding for highly swollen lamellae [130, 131].

Further increasing χN above 17 leads to further increased conversion and depletion

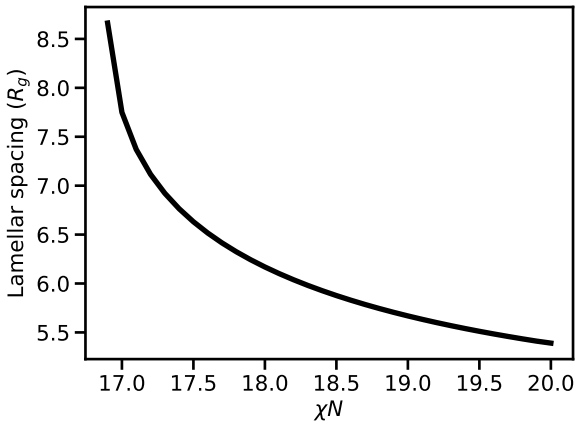

Figure 5.3: Domain spacing of the lamellar phase as a function of χN at $h/\chi N = 0.5$ and $\psi_A = 0.5$.

of the remaining homopolymer in the system. This causes the domain size to decrease, as there is less homopolymer to swell the system. We truncate this phase diagram at $\chi N = 20$, but it is possible that other phases can form at even higher values of χN. The conversion provides a simple scalar description of the reaction equilibrium, but does not provide information on what types of block copolymers are present in the system. In Figure 5.4 we plot the distribution of products at $\psi = 0.5$ and $\chi N = 17$ and $\chi N = 20$.

At $\chi N = 17$ the distribution is dominated by AB diblock and the individual homopolymers, with triblocks and the tetrablock also making meaningful contributions to the total volume of the system. Higher order block copolymers quickly become irrelevant, however. At $\chi N = 20$ the distribution is significantly broadened and the amount of homopolymer is reduced by 80% from $\chi N = 17$. The average length product is also shifted to longer block copolymers as well. Note that the products considered in Figure 5.4 only account for 93% of the mass, the remainder of which is composed of longer BCPs.

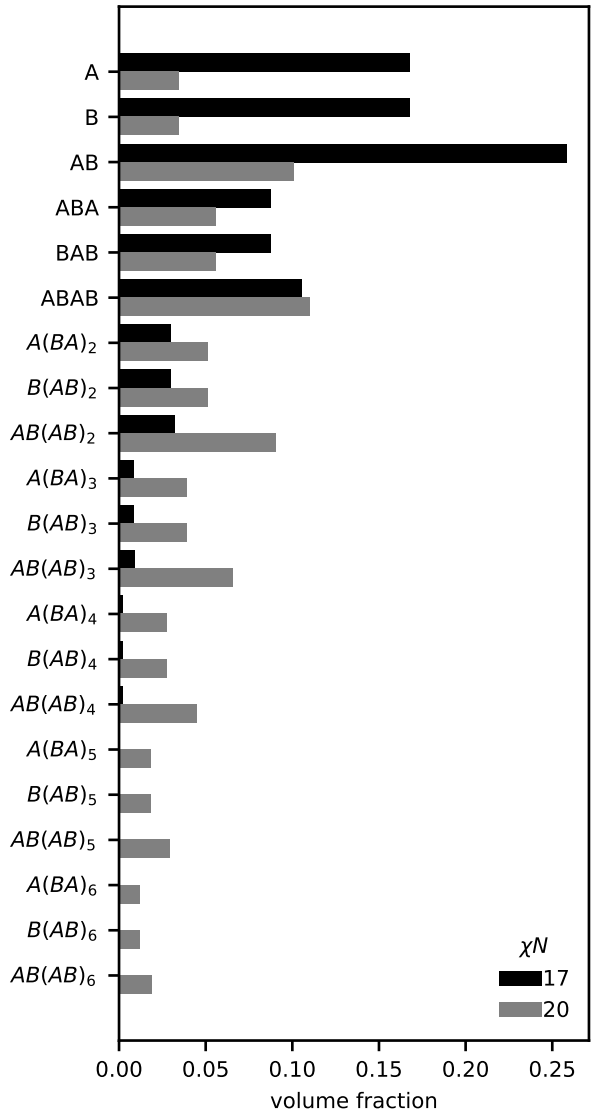

Figure 5.4: Distribution of products in the lamellar phase at $h/\chi N = 0.5$ and $\psi_A = 0.5$ and $\chi N = 17$ or $\chi N = 20$.

5.3.2 Strong bonding

We now consider a case where the equilibrium constant is large compared to segregation strength and set $h/\chi N = 2$, where phase boundaries are plotted in Figure 5.5. Contrary to the weak bonding case, there is no large co-existence region between disordered phases. Instead, the phase diagram is dominated by regions of microphases, separated by narrow channels of coexistence. At the edges of the phase diagram there are significant regions of coexistence between microphases and a disordered phase. Similar to the weak bonding case, it is favorable to eject excess homopolymer to avoid significantly swelling the domain. It is also possible that other sphere phases such as FCC, HCP, or Frank-Kasper phases could be present in this area, but we do not consider them in this work. While the relative position of the stable region for each microphase is similar to that of unreactive block copolymers, there are some notable differences, including the fact the BCC phase becomes unstable above $\chi N = 10.5$ and is replaced with a two phase window between DIS and HEX. The shape of the order-disorder transition is also quite different from unreactive block copolymers and has a cusp in the center of the phase diagram, indicating that at $\psi_A = 0.5$ the mixture has a higher (χN_{ODT}) than at $\psi_A = 0.33$ or $\psi_A = 0.66$. Before addressing the shape of the ODT, it is useful to examine the reaction equilibrium again.

Figure 5.6 shows the conversion of species A with varying χN at $\psi_A = 0.5$, analogous to Figure 5.2 for weak bonding. For strong bonding, the conversion of species A increases quite quickly with increasing χN so that at $\chi N = 2$ (the unreactive homopolymer blend critical point), $\alpha_A = 0.1$. At this level of conversion there is enough BCP present to compatibilize the A and B homopolymers and maintain a single disordered phase. Further increasing χN continues to increase the conversion until it reaches near completion. Near the order disorder transition at $\chi N = 7.45$ the conversion in the disordered phase has

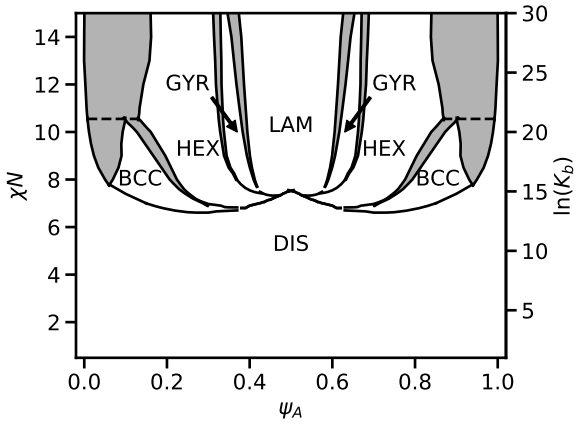

Figure 5.5: Phase diagram for a binary blend of heterobonding telechelic homopolymers at $h/\chi N = 2.0$. Shaded regions indicate two phase coexistence while white regions indicate a single phase is present.

reached nearly 100%. Crossing into the lamellar phase continues this trajectory and the conversion stays near unity. One can repeat this exercise at other values of ψ_A to find that the minority species is near 100% conversion at the ODT for all compositions.

Based on this information, we might approximate the system as being composed of all BCP or BCP plus a single excess homopolymer component depending on stoichiometry. Using this assumption, we can rationalize the shape of the ODT based on the stoichiometry of the system. For $\psi_A = 0.5$, stoichiometry allows for $\alpha = 1$ for both species, so that extremely long AB repeating block copolymers can be formed. At $\psi_A = 2/3$, the stoichiometry would allow for formation of all ABA triblocks as there are two A chains present for each B chain. At $\psi_A = 1/3$, the inverse is true, allowing formation of all BAB triblocks. Finally, at $\psi_A = 0$ and $\psi_A = 1$ the system is composed entirely of B or A homopolymer, respectively. We can then approximate various parts of the ODT using mixtures of these different components. In Figure 5.7 we use the random phase approximation [4] (RPA) to plot the approximate ODT for the fully reactive telechelic blend, as well as for binary blends of homopolymers, triblocks, and the AB repeating polymer.

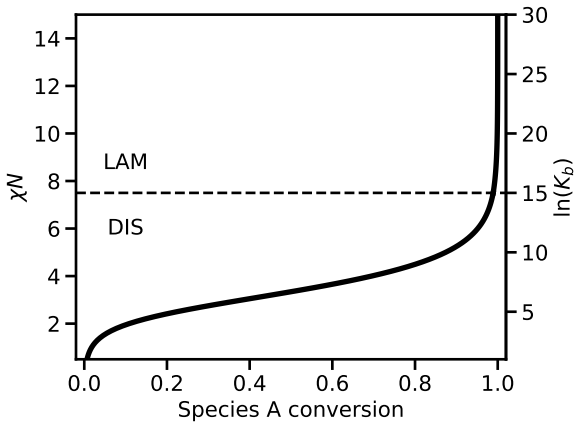

Figure 5.6: Conversion of species A, α_A, at $h/\chi N = 2.0$ and $\psi_A = 0.5$. The text labels and dashed line indicate the stable phase.

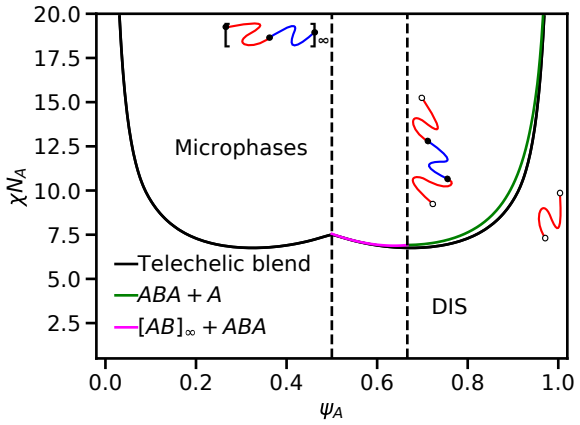

Figure 5.7: Order-disorder transitions computed via RPA for the telechelic blend system at $h/\chi N = 2$ (black), an unreactive binary blend of ABA triblock and A homopolymer (green), and an unreactive blend of ABA triblock with infinitely repeating (AB) multiblock (magenta).

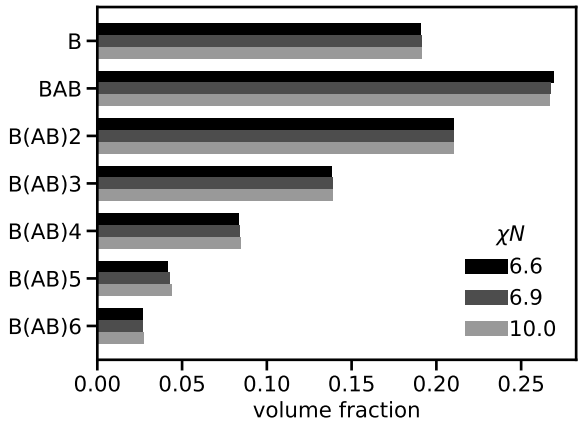

Figure 5.8: Distribution of products found in the disordered phase of the telechelic blend at $\psi_A = 2/3$ and $\alpha_B = 0.99$.

The unreactive binary blends match reasonably closely to the fully reactive telechelic system. This is somewhat surprising because the telechelic system is composed of a wide array of different block copolymer products. In Figure 5.8 we plot the full distribution of products at $\psi_A = 0.68$ and $\chi N = 6.6$, 6.9, or 10.0. At $\chi N = 6.6$ the system is still in the disordered phase whereas at the two higher χN values the HEX phase is stable. In all cases, triblock polymers make up less than 30% of the volume despite the stoichiometry allowing for near complete formation of triblocks. Homopolymers remain a significant contribution at $\approx$ 19% of the volume and higher order block copolymers that are B-terminated make up the remainder. Although the crude model of a triblock mixed with homopolymer matches the ODT for the telechelic blend closely, it does not represent the actual distribution of products.

We are also able to evaluate the distribution of products at $\psi_A = 0.5$ and $\chi N = 7$, which is just below the ODT. Considering products with a length of up to 50 macromonomers accounts for only 25% of the mass in the system, revealing that the system is dominated by very long block copolymers.

As a final comparison to the weak bonding case, we plot the domain spacing of the

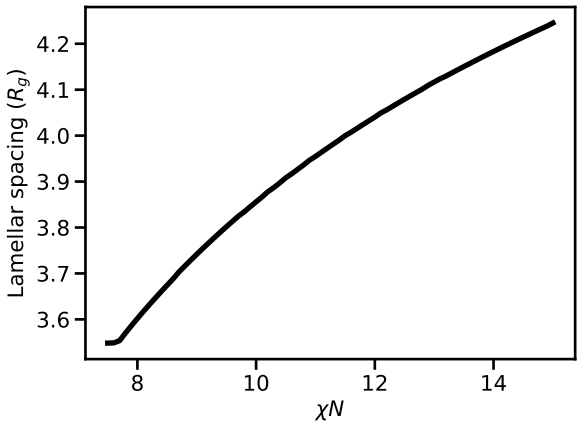

Figure 5.9: Domain spacing of the lamellar phase as a function of χN at $h/\chi N = 2.0$ and $\psi_A = 0.5$.

lamellar phase at $\psi_A = 0.5$, shown in Figure 5.9. For high bond strength the domain spacing increases with increasing χN, which is the opposite trend of what occurs at weak bonding. Additionally, the magnitude of change in the domain spacing is much smaller at strong bonding compared to weak bonding. We can attribute the difference between the two regimes to the mechanisms that cause the domain spacing to change. At weak bonding the domain size was largely affected by the conversion in the system and the amount of unreacted homopolymer that was present to swell the system. At strong bonding, the conversion is nearly unity in the lamellar phase as shown in Figure 5.6. This means there is little to no homopolymer present to swell the system and the previous mechanism is no longer relevant. Instead the brush physics at the lamellar interface dominates and as χN increases, the chains want to stretch away from the interface, leading to increased domain spacing.

5.3.3 Intermediate bonding

Thus far we have considered two opposite limits of relative strength of bonding compared to segregation strength. We now consider the transition between the two and

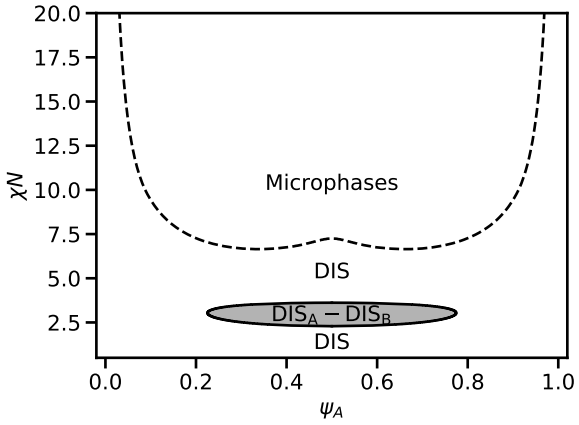

Figure 5.10: Phase diagram for a binary blend of heterobonding telechelic homopolymers at $h/\chi N = 1.5$. Shaded regions indicate two phase coexistence while white regions indicate a single phase is present.

examine an intermediate bond strength of $h/\chi N = 1.5$, for which the phase diagram is illustrated in Figure 5.10. The phase diagram shows features from both the weak bonding and strong bonding phase diagrams. For $2 < \chi N < 4$ it is possible to phase separate into two disordered liquids similar to the weak bonding case. This region has both UCST and LCST character, and closes for $\chi N > 4$, and a single disordered liquid becomes stable. As χN is further increased the system undergoes another transition, but this time into microphases. We do not perform full numerical SCFT investigation of this region, but the random phase approximation reveals that the disordered phase has instabilities at non-zero k vector, indicating formation of microphases. Furthermore, the shape of the phase boundary is high reminiscent of that from $h/\chi N = 2$ and we expect very similar stability windows.

To understand this complex phase portrait, we again turn to the reaction equilibrium. Figure 5.11 shows the conversion of species A at $\psi_A = 0.5$ for varying χN. As in previous cases, conversion increases with increasing χN. At $\chi N \approx 2.25$ the conversion of species A is $\alpha_A \approx 0.07$, corresponding to approximately 10% volume fraction of copolymer. This is insufficient quantity of homopolymer to prevent phase separation, but is enough to delay

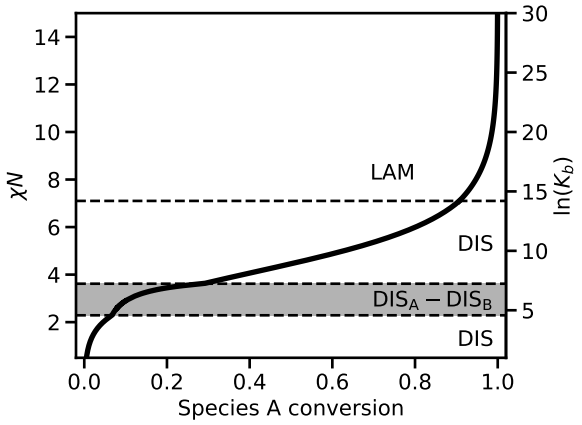

Figure 5.11: Conversion of species A, α_A, at $h/\chi N = 1.5$ and $\psi_A = 0.5$. The text labels and dashed line indicate the stable phase(s).

phase separation from the unreactive critical point of $\chi N = 2$. As χN is further increased above 2.25, the conversion continues to increase, in contrast to the weak bonding case where conversion started to decrease upon phase separation. In this intermediate bonding case the phase segregation near the critical point is not very strong and the A rich phase is composed of at least 20% component B. The equilibrium constant is also sufficiently large so that forming BCP products is still favored, and conversion continues to increase. Careful examination of the conversion reveals that the phase separation does slightly depress conversion compared to a hypothetical scenario of a well mixed single phase, but this effect is rather weak.

As χN is increased through the two phase window, eventually enough copolymer is formed to recompatibilize the two phases at $\chi N \approx 3.6$. The conversion at this point is $\alpha_A \approx 0.27$, which corresponds to a combined homopolymer volume fraction of 52%. This is consistent with previous theoretical studies of A homopolymer + B homopolymer + AB diblock that found that approximately 45% volume fraction of diblock copolymer was sufficient to compatibilize homopolymers [132], when the homopolymer had half the length of the diblock as in this study. For $\chi N > 3.6$ the conversion plot strongly resembles

that of the strong bonding case, and eventually the blend microphase separates into a lamellar phase. The trends in lamellar domain spacing also mimic that of the strong bonding case, and domain spacing increases monotonically with increasing χN.

The phase behavior at this intermediate value of $h/\chi N$ is indicative of being near a Lifshitz point, where microphase separation, macrophase separation, and a single disordered phase meet at a single point. It is known from unreactive polymer blends that SCFT fails dramatically near the Lifshitz point and fluctuations stabilize bicontinuous microemulsions [64, 65]. We expect such fluctuations effects to also be present in this system, but do not speculate further on their effect. In principle it is possible to include fluctuation effects in our model via a field theoretic simulation, but we leave such efforts for future work.

5.3.4 Unequal macromonomer lengths

Up to this point we have only considered blends where the two homopolymers are of equal length. We next consider the case where the B polymer is half as long as the A homopolymer, $N_B/N_A = 0.5$. Upon breaking the symmetry of the two polymers, the symmetry of the phase diagram is correspondingly broken. Figure 5.12 shows the RPA spinodal curves for $N_B/N_A = 0.5$ and $h/\chi N = 2$. Analogous to the strong bonding case for symmetric polymers, the phase diagram has a two lobe structure with a cusp in the middle. The cusp occurs at $\phi_A = 2/3$ which is the proper composition to form repeating AB block copolymers. Numerical SCFT calculations reveal that for $\phi_A < 0.5$ the lamellar phase is stable, with a coexistence region with a disordered phase also present. This is to be expected, as the analogous unreactive system consists of a BAB triblock that has an equal number of total A and B segments, blended with a homopolymer. A similar system of a symmetric AB diblock blended with B homopolymer also produced a region

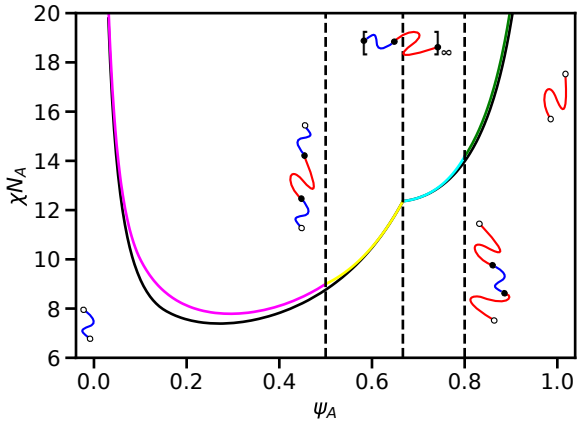

Figure 5.12: Order-disorder transitions computed via RPA for the telechelic blend system with $N_B/N_A = 0.5$ (black), and multiple unreactive binary blends, including: ABA triblock and A homopolymer (green), ABA triblock with infinitely repeating (AB) multiblock (cyan), BAB triblock with infinitely repeating (AB) multiblock (yellow), and BAB triblock with B homopolymer (magenta).

of LAM stability as well as LAM and DIS coexistence [129, 133].

5.4 Comparison with experiments

One of the earliest experimental investigations of the phase behavior of telechelic blends is due to Russell and coworkers [111]. They used small-angle x-ray scattering (SAXS) to study blends of telechelic polyisoprene and polystyrene that were end-functionalized with amino and acid groups, respectively. The acid groups considered were carboxylic acid and sulfonic acid. Supramolecular bonds can form when an acid protonates an amino group, which induces an ionic bond. Bulk polyisoprene and polystyrene have dielectric constants near 3, so it is very unfavorable for unpaired ions to exist. For the bonds to dissociate, the reverse proton transfer must occur so that the neutral amine and acid can separate from one another. Evidence for the partial conversion of acid and base to paired ions was found by FT-IR in later work by Iwasaki and coworkers [134].

The scattering data from amino-terminated polyisoprene blended with carboxylic-

acid-terminated polystyrene is consistent with the weak bonding picture presented in this work. The authors observed microphase formation at low temperature (high χ) and that upon heating the blend would undergo spinodal decomposition and macroscopically phase separate, analogous to decreasing χN in Figure 5.1. Additionally, the domain size of the microphase was found to significantly increase with increasing temperature (decreasing χN) consistent with weak-bonding domain size trends in Figure 5.3. The authors showed that the change in domain size was too large to be attributed to thermal expansion, so the change in domain size due to homopolymer swelling demonstrated in this work may play a role.

When the carboxylic acid groups were replaced with sulfonic acid groups, Russell and coworkers found qualitatively different behavior. The blend again formed a microphase at low temperature, but upon heating became disordered rather than undergoing spinodal decomposition. This is consistent with the strong-bonding phase behavior presented in Figure 5.5. Additionally, the domain spacing of the microphase had a much weaker dependence on temperature compared to the blend with carboxylic acid. The domain size slightly decreased with increasing temperature, consistent with the trends in domain size at strong bonding in Figure 5.9. The blend with sulfonic acid-functionalized polystyrene thus behaves like the strong bonding regime predicted in this work. Furthermore, sulfonic acid is a stronger acid than carboxylic acid, so effective equilibrium constant should be larger for the sulfonic acid-amine pairing. Finally, Russell and coauthors showed that if the length of the polystyrene polymers was increased, then the system would again macrophase separate at high temperature consistent with the intermediate-bonding phase diagram in Figure 5.10. This is consistent with previous theoretical investigations that showed that increased polymer length dilutes the concentration of end groups and leads to an effectively weaker equilibrium constant [118].

There have been multiple subsequent reports that utilize the same acid-amine chem-

istry as Russell and coworkers, but swap the isoprene monomer with a different chemical species, including ethylene oxide, isobutylene, and PDMS [134–136]. In addition to SAXS, these authors have performed FT-IR, proton NMR, TEM, and rheological measurements on their samples to provide further evidence for block copolymer formation from the starting homopolymers and the presence of an order-disorder transition. One group of authors was also able to estimate the approximate values of χN for which the ODT occurs which matches closely to the value we predict at equal composition in Figure 5.5 [135]. In all of the referenced papers, only equimolar blends of telechelic polymers were considered, so much of the phase space remains unexplored.

In addition to the acid base supramolecular interactions, there have been investigations of telechelic polymers that interact through hydrogen bonding [137, 138]. These investigations are not as extensive as the previously discussed work, but were able to show evidence of microphase formation via SAXS and TEM. Unfortunately there is not enough temperature dependent data to compare these works with the bonding strength cases considered here.

5.5 Conclusions

We have demonstrated that a wide variety of phase behavior can be achieved with binary blends of heterobonding telechelic homopolymers. By properly tuning the relative strength of the bonding equilibrium constant to the segregation strength it is possible to make the system behave like an unreactive homopolymer blend or block copolymer melts. Although some of the microphase stability windows have unconventional shapes, these stability windows can be rationalized by considering the stoichiometry of the system. Additionally, the microphases that are formed from the telechelic blend can have highly variable domain sizes and differing dependence on temperature depending on the

relative strength of bonding and phase separation. The models presented here are able to quantitatively predict all these phenomena and are consistent with previous experiments. We hope CS-SCFT will be used to further guide experimental investigation of supramolecular blends.

Chapter 6

Reversible Star Polymer Networks in Solution

6.1 Introduction

Polymer networks are fundamental platform for many important modern materials, including rubber tires, artificial tissues, and adsorbents. In recent years, polymer networks that are formed from reversible bonds have become a topic of interest. This is in part due to novel materials properties, such as self-healing [116], as well as biologically-motivated observations of such phenomenon [110]. Much of our understanding of polymer networks is due to initial theories by Flory [51] and Stockmayer [50], who performed pioneering work with simple mathematical models. They were able to show that at a particular extent of reaction, the average size of a polymer cluster diverges, indicating the onset of gelation and the formation of a macroscopic sized molecule. Notably, there are a number of deficiencies with Flory theory, mainly that it neglects the formation of loop and ring structures, and does not account for excluded volume or other interactions between polymer segments. Finally, it is fundamentally a mean-field theory that neglects

the role of composition fluctuations that are important in polymer solutions. There have been a number of efforts to correct for these phenomena in permanent networks, which often invoke field-based methods. One example is work by Lubensky and Isaacson who used an n-vector model and applied the $n \to 0$ formalism of de Gennes [139, 140]. They were able to use analytical approximations to study dilute gels and compute correlation lengths, but could not evaluate phase separation or the concentrated regime. Another example by Panyukov and Rabin used replica field theory to predict structure factors and elastic properties in a permanent gel [141]. They were also limited to approximate analytical techniques, however.

Theoretical studies of reversible gels are less common, however, one notable example is work by Edwards and Freed who developed field based models of polymer vulcanization using coherent states (CS) [103]. This work has largely gone unnoticed, however, especially compared to other field models introduced by Edwards [3]. In this work we return to the CS models developed by Edwards to study reversible polymer networks in solution and examine both gelation and phase separation. These two phenomena often occur simultaneous in polymer and colloid solutions, leading to confusion on their relationship. With the models considered here we are able to interrogate the equilibrium behavior without kinetic limitations, and also include effects of excluded volume, rings, and fluctuations. We start at the mean field level and show that a reduced set of parameters can be defined from the fundamental parameters of reaction equilibrium constant, polymer concentration, and solvent quality to yield a universal phase diagram. We then pursue approximate analytical calculations to include fluctuations and show that the universal phase diagram is disrupted. Finally we turn to numerical simulations that relax the previous approximations to fully understand the effect of rings and loops and the relationship between percolation and phase separation.

6.2 Model and Methods

A hybrid AF-CS model for a canonical ensemble of reversibly end bonding star homopolymers in implicit solvent is

$$Z(n,V,T) = \frac{Z_0}{D_w D_\phi} \int \mathcal{D}w \int \mathcal{D}(\phi,\phi^*) e^{-H[w,\phi,\phi^*]} \tag{6.1}$$

$$\begin{aligned} H[w,\phi,\phi^*] = {} & \frac{1}{2\beta u_0} \int d\boldsymbol{r}\ (w(\boldsymbol{r}))^2 - n \ln \left(\frac{1}{V} \int d\boldsymbol{r}\ (\phi_0^*(\boldsymbol{r}))^f\, e^{-i\Gamma * w(\boldsymbol{r})} \right) \\ & + \sum_{j=0}^{N_{\text{arm}}} \int d\boldsymbol{r}\, \phi_j^*(\boldsymbol{r}) \phi_j(\boldsymbol{r}) - \sum_{j=1}^{N_{\text{arm}}} \int d\boldsymbol{r}\, \phi_j^*(\boldsymbol{r}) e^{-i\Gamma * w(\boldsymbol{r})} \int d\boldsymbol{r}'\, \Phi(\boldsymbol{r}-\boldsymbol{r}') \phi_{j-1}(\boldsymbol{r}) \\ & - \int d\boldsymbol{r}\, \phi_{N_{\text{arm}}}(\boldsymbol{r}) - \frac{\lambda_b}{2} \int d\boldsymbol{r} \int d\boldsymbol{r}' \phi_{N_{\text{arm}}}(\boldsymbol{r}) \Phi_b(\boldsymbol{r}-\boldsymbol{r}') \phi_{N_{\text{arm}}}(\boldsymbol{r}') \end{aligned} \tag{6.2}$$

$$D_w = \int \mathcal{D}w \exp \left(\frac{1}{2\beta u_0} \int d\boldsymbol{r}\, (w(\boldsymbol{r}))^2 \right) \tag{6.3}$$

$$\begin{aligned} D_\phi = \int \mathcal{D}(\phi,\phi^*) \exp \Bigg(& \sum_{j=0}^{N_{\text{arm}}} \int d\boldsymbol{r}\, \phi_j^*(\boldsymbol{r}) \phi_j(\boldsymbol{r}) \\ & - \sum_{j=1}^{N_{\text{arm}}} \int d\boldsymbol{r}\, \phi_j^*(\boldsymbol{r}) e^{-i\Gamma * w(\boldsymbol{r})} \int d\boldsymbol{r}'\, \Phi(\boldsymbol{r}-\boldsymbol{r}') \phi_{j-1}(\boldsymbol{r}) \Bigg) \end{aligned} \tag{6.4}$$

where Z is the partition function, with Z_0 an ideal gas partition function, n the number of homopolymer chains, V the system volume and T temperature. In this model, polymer segments interact via a Gaussian potential of mean force

$$u(\boldsymbol{r}) = u_0 \Gamma(\boldsymbol{r}) = \frac{u_0}{(2\pi a^2)^{3/2}} \exp \left(-\frac{|\boldsymbol{r}|^2}{2a^2} \right) \tag{6.5}$$

This is equivalent to a contact interaction between segments, but with the segment density smeared over a Gaussian packet. This smearing is required to make the model

UV convergent and appears via the expression

$$\Gamma * w(\boldsymbol{r}) = \int d\boldsymbol{r}'\, \Gamma(\boldsymbol{r} - \boldsymbol{r}')w(\boldsymbol{r}') \tag{6.6}$$

The interacting system is captured via the effective Hamiltonian H which is a functional of the field $w(\boldsymbol{r})$ that varies over space, $\boldsymbol{r}$, as well as a set of CS fields $\phi_j(\boldsymbol{r})$ and $\phi_j^*(\boldsymbol{r})$ that also vary over space, but have an additional index that indicates a contour position along a polymer arm. Each polymer is composed of f arms that each have N_{arm} beads that are linked together with Hookian springs. The entire polymer then has $N_{\text{tot}} = fN_{\text{arm}} + 1$ total beads. For the ϕ_j and ϕ_j^* fields, $j = 0$ corresponds to the central bead, while $1 \leq j \leq N_{\text{arm}}$ indicate beads in the arms. Because all arms are identical, we do not need separate CS fields for each arm.

Each term in the effective Hamiltonian has a simple physical interpretation. The first term that is quadratic in w represents the pairwise interaction between beads via the potential of mean force. It is associated with the thermal energy $\beta = 1/k_BT$ as well as the interaction strength u_0, which can be interpreted as the solvent quality. The second term creates n beads that will be the center of the star polymers. It has f factors of ϕ_0^* which each generate an arm that will grow out from the center bead. Finally $\exp(-i\Gamma * w)$ allows the bead to interact with other beads through the potential of mean force. Here we have invoked the smearing function Γ which is a normalized Gaussian function, as well as i the complex unit. The second line of the Hamiltonian is responsible for propagating polymer arms. The second term creates a bond between the $j-1$ and j beads via the normalized bond transition probability Φ, then creates the j bead via the bead weight term $\exp(-i\Gamma * w)$. The arms are terminated as free ends via the first term on the third line of eq 6.2, which terminates the arms after N_{arm} beads. The final term in the Hamiltonian creates reversible bonds between chain ends. These bonds carry an activity

λ_b and are associated with the bond transition probability Φ_b. Notably, these bonds can be either intra-molecular or inter-molecular allowing the creation of both networks and molecules with loops. One can show through perturbation theory that this model correctly generates all possible reaction products with proper weighting. As written, the supramolecular linkages can have a different linker type than the covalent bonds, however, for the remainder of this work we assume they are identical Hookian springs

$$\Phi(\boldsymbol{r}) = \Phi_b(\boldsymbol{r}) = \left(\frac{3}{2\pi b^2}\right)^{3/2} \exp\left(-\frac{3|\boldsymbol{r}|^2}{2b^2}\right) \tag{6.7}$$

where b is the root mean square mean bond length in the non-interacting system.

Before advancing further, it is convenient re-scale some parameters to define dimensionless groups. We make the substitution $w = W/N_{\text{tot}}$ and re-scale $\boldsymbol{r}$ by a factor of $R_g = \sqrt{b^2 N_{\text{tot}}/6}$. The fields are invariant to scalings of $\boldsymbol{r}$ and the scaling to w is exactly canceled by the Jacobian factor from D_w. These scalings yield three dimensionless groups that will define the behavior of the system. The first is a dimensionless chain concentration $C = nR_g^3/V$, the second a dimensionless interaction strength $B = \beta u_0 N_{\text{tot}}^2/R_g^3$ and thirdly a dimensionless equilibrium constant $K = \lambda_b/R_g^3$. A factor of R_g^3 has also been absorbed into ϕ_j. In these new parameters, the model Hamiltonian is

$$\begin{aligned} H[W,\phi,\phi^*] = \frac{1}{2B}\int d\boldsymbol{r}\ (W(\boldsymbol{r}))^2 - CV\ln\left(\frac{1}{V}\int d\boldsymbol{r}\ (\phi_0^*(\boldsymbol{r}))^f\, e^{-i\Gamma * W(\boldsymbol{r})/N_{\text{tot}}}\right) \\ + \sum_{j=0}^{N_{\text{arm}}}\int d\boldsymbol{r}\,\phi_j^*(\boldsymbol{r})\phi_j(\boldsymbol{r}) - \sum_{j=1}^{N_{\text{arm}}}\int d\boldsymbol{r}\,\phi_j^*(\boldsymbol{r}) e^{-i\Gamma * W(\boldsymbol{r})/N_{\text{tot}}}\int d\boldsymbol{r}'\,\Phi(\boldsymbol{r}-\boldsymbol{r}')\phi_{j-1}(\boldsymbol{r}) \\ - \int d\boldsymbol{r}\,\phi_{N_{\text{arm}}}(\boldsymbol{r}) - \frac{K}{2}\int d\boldsymbol{r}\int d\boldsymbol{r}'\phi_{N_{\text{arm}}}(\boldsymbol{r})\Phi_b(\boldsymbol{r}-\boldsymbol{r}')\phi_{N_{\text{arm}}}(\boldsymbol{r}') \end{aligned} \tag{6.8}$$

With the model defined we now present field operators that can be used to interrogate

physical properties of the system. The local density of segments in the system can be computed according to

$$\tilde{\rho}(\boldsymbol{r}) = C\frac{(\phi_0^*(\boldsymbol{r}))^f\, e^{-i\Gamma * W(\boldsymbol{r})/N_{\rm tot}}}{\int d\boldsymbol{r}\ (\phi_0^*(\boldsymbol{r}))^f\, e^{-i\Gamma * W(\boldsymbol{r})/N_{\rm tot}}} + \sum_{j=1}^{N_{\rm arm}} \int d\boldsymbol{r}\, \phi_j^*(\boldsymbol{r}) e^{-i\Gamma * W(\boldsymbol{r})/N_{\rm tot}} \int d\boldsymbol{r}'\, \Phi(\boldsymbol{r}-\boldsymbol{r}')\phi_{j-1}(\boldsymbol{r}) \tag{6.9}$$

The local density of unreacted chain ends is

$$\tilde{\rho}_e(\boldsymbol{r}) = \phi_{N_{\rm arm}}(\boldsymbol{r}) \tag{6.10}$$

and the local density of bonds is

$$\tilde{\rho}_b(\boldsymbol{r}) = \frac{K}{2}\int d\boldsymbol{r}'\phi_{N_{\rm arm}}(\boldsymbol{r})\Phi_b(\boldsymbol{r}-\boldsymbol{r}')\phi_{N_{\rm arm}}(\boldsymbol{r}') \tag{6.11}$$

Each of these local densities can be averaged over space to obtain bulk values for the density of segments, bonds, and unreacted chain ends. One convenient observable to track is the conversion of end groups η which is defined as

$$\eta = \frac{fn - n_e}{fn} = \frac{2n_b}{fn} \tag{6.12}$$

where n_e and n_b are the total number of unreacted ends and bonds, respectively. These quantities can be determined by integrating the appropriate local density operator over all of space.

Other important operators are the chemical potential μ and pressure Π, which have

the operators

$$\beta\tilde{\mu}_{\rm ex} = -\ln\left(\int d\boldsymbol{r}\ (\phi_0^*(\boldsymbol{r}))^f\, e^{-i\Gamma * W(\boldsymbol{r})/N_{\rm tot}}\right) \tag{6.13}$$

$$\begin{aligned}\beta R_g^3\tilde{\Pi}_{\rm ex} = &\frac{i}{N_{\rm tot}}\int d\boldsymbol{r}\int d\boldsymbol{r}'\,\tilde{\rho}(\boldsymbol{r})\Gamma(\boldsymbol{r}-\boldsymbol{r}')\left(\frac{1}{2}-\frac{a^2}{3}\nabla^2\right)W(\boldsymbol{r}')\\ &+\sum_{j=1}^{N_{\rm arm}}\int d\boldsymbol{r}\int d\boldsymbol{r}'\,\phi_j^*(\boldsymbol{r})e^{-i\Gamma * W(\boldsymbol{r})/N_{\rm tot}}\Phi(\boldsymbol{r}-\boldsymbol{r}')\left(\frac{b^2}{6}\nabla^2\right)\phi_{j-1}(\boldsymbol{r}')\\ &-\int d\boldsymbol{r}\int d\boldsymbol{r}'\,\phi_{N_{\rm arm}}(\boldsymbol{r})\Phi_b(\boldsymbol{r}-\boldsymbol{r}')\left(\frac{b^2}{6}\nabla^2\right)\phi_{N_{\rm arm}}(\boldsymbol{r}')\end{aligned} \tag{6.14}$$

These operators are given in excess to the ideal gas contribution.

6.3 Results and Discussion

6.3.1 Mean Field

We first analyze the model at a mean field level where we invoke a saddle point approximation. It is assumed that there exist a set of field configurations that completely dominate the functional integrals in eq 6.1. The saddle point fields must satisfy the equations

$$\left.\frac{\delta H}{\delta W}\right|_{W_s,\phi_{j,s},\phi_{j,s}^*} = \left.\frac{\delta H}{\delta \phi}\right|_{W_s,\phi_{j,s},\phi_{j,s}^*} = \left.\frac{\delta H}{\delta \phi^*}\right|_{W_s,\phi_{j,s},\phi_{j,s}^*} = 0 \tag{6.15}$$

We can trivially evaluate the free energy under the saddle point approximation as

$$\beta F = -\ln(Z) \approx -\ln(Z_0) - \ln(\exp(-H[W_s,\phi_s,\phi_s^*])) \tag{6.16}$$

for the model considered here this yields

$$\frac{\beta R_g^3 F_{\mathrm{MF}}}{V} = C\ln(C) - C + \frac{1}{2}BC^2 + fC\ln(1-\eta_{\mathrm{MF}}) + \frac{1}{2}\eta_{\mathrm{MF}} fC \tag{6.17}$$

where we have used Sterling's approximation to evaluate the ideal gas partition function. We have also invoked the mean field conversion η_{MF} which can be computed as

$$\eta_{\mathrm{MF}} = \frac{2fCK + 1 - \sqrt{1+4fCK}}{2fCK} \tag{6.18}$$

With the free energy in hand we can compute other important physical quantities including the pressure Π and chemical potential μ

$$\beta R_g^3 \Pi_{\mathrm{MF}} = \beta R_g^3 \left(\frac{\partial F}{\partial V}\right)_{n,T} = C + \frac{1}{2}BC^2 - \frac{1}{2}\eta_{\mathrm{MF}} fC \tag{6.19}$$

$$\beta\mu_{\mathrm{MF}} = \beta\left(\frac{\partial F}{\partial n}\right)_{V,T} = \ln(C) + BC + f\ln(1-\eta_{\mathrm{MF}}) \tag{6.20}$$

Using the chemical potential and pressure we can identify if phase separation is possible as well as the equilibrium concentrations of the phase separated system. The phase diagram would seemingly depend on four parameters: f, C, B, and K as each of these appears in the expressions for Π and μ either directly or indirectly via η. A careful examination of the pressure and chemical potential reveals, however, that the parameter space can be reduced by appropriately grouping variables. The pressure can be multiplied by B without affecting the thermodynamics, which reveals that $B\beta R_g^3\Pi$ only depends on f, BC, and η via eq 6.19. Similarly, the chemical potential can be shifted by a constant $\ln(B)$ without affecting the thermodynamics. Eq 6.20 reveals that $\beta\mu + \ln(B)$ only depends on f, BC, and η as well. Finally we must consider η, which depends on the combined grouping fCK. We can rewrite this group as $f(BC)(K/B)$, which shows that

η depends on two of the same parameters, f and BC as well as a third quantity K/B. These three groups can be used to define the phase diagram in the smallest number of parameters.

In Figure 6.1 we present one such phase diagram for $f = 3$. The grey curve denotes the binodal in the system, whereas the white region is the interior of the spinodal. We will discuss derivation of the spinodal later. The background of the figure is colored according to the conversion at each point in phase space. Finally, the dotted black line indicates the Flory gel point which is computed according to:

$$\alpha_{\text{gel}} = \frac{1}{f-1} \tag{6.21}$$

Here α represents the probability that an arm is reacted to another polymer that will propagate to create a larger molecule. In the mean-field limit of SCFT, loops cannot be formed and $\eta = \alpha$, however for fluctuating systems, the presence of loops will disrupt this equality as loops do not help form a larger molecule. The figure shows that at small values of K/B the system will not undergo phase separation for any concentration of polymer. The system can still undergo gelation for sufficiently concentrated solutions, however. As K/B is increased above 10, a two phase region occurs. Notably, the spinodal for this region lies entirely in the gel regime. This has important implications for experimental polymers, as the system will first try to percolate before undergoing phase separation. This may significantly hamper the dynamics of phase separation if a network has already formed. Because the bonds are reversible, at infinite time scales the system will be able to fully phase separate, but short time scales may be significantly impacted. The physical interpretation for this region is that the equilibrium constant is sufficiently large such that the system wants to form a gel, however, the concentration is low enough that the polymers would have to stretch excessively to reach one another to maintain a

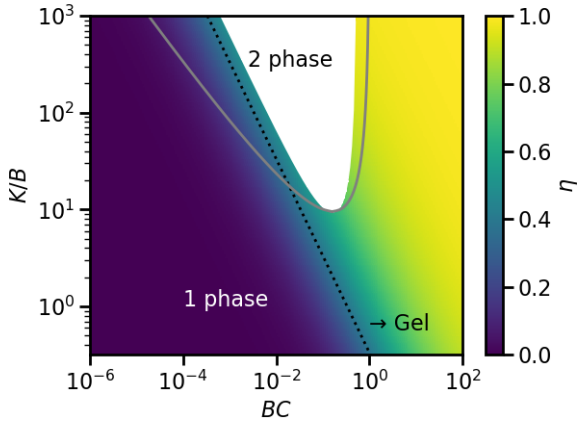

Figure 6.1: Universal mean-field phase diagram for end-linking star polymers with $f = 3$ arms. The binodal is indicated with the grey curve whereas the spinodal region is indicated with white. The black line is the gel transition. The background of the plot is colored according to the conversion of end groups η.

homogeneous solution. Instead, the system phase separates into a concentrated polymer phase that can easily form a gel and a phase where polymers are sufficiently diluted that they do not try to form a network.

The previous explanation invokes the equilibrium constant K and chain concentration C, but did not address the dimensionless interaction strength B. The parameter B can also be interpreted as the solvent quality as it contains the potential of mean force strength u_0. In this model the bead-bead interactions are purely repulsive and B must be non-negative, so we only consider theta solvents and good solvents. As the the solvent quality increases, the polymer chains will undergo coil expansion and the arms of the star will stretch out. This increases the pervaded volume of each molecule and the number of molecules that each polymer can interact with will increase. The grouping BC thus represents this effective concentration that is increased by solvent quality. On the other hand, when solvent quality is high, the polymer would rather be surrounded by solvent molecules than other polymer segments. This means that forming a supramolecular bond will be energetically disadvantageous for large B. As such, the effective bond strength in

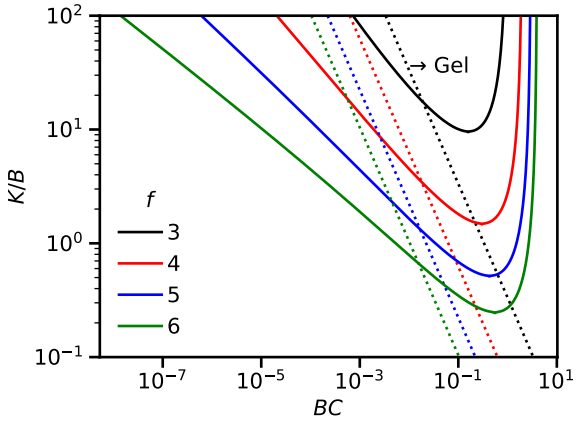

Figure 6.2: Mean-field phase diagram for end-linking star polymers for a variety of number of arms. The binodal is indicated with solid lines while dotted lines indicate the gel transition.

the phase diagram is K/B, as large B will decrease the favorability of bond formation.

Finally, we address the effect of the number of arms, as Figure 6.1 is valid only for $f = 3$. In Figure 6.2 we plot the binodals and gel transition curves for a variety of number of arms. As the number of arms is increased, the binodal shifts to lower values of K/B as do the gel transition curves. For larger number of arms it easier to undergo gelation as a smaller conversion is required to percolate the system, so smaller values of K (or C) are required for gelation. Similarly, increased f expands the regime in which gelation is favorable, but not possible due to insufficient polymer concentration, so the binodal regions shift to lower K as well. Although not shown on the in Figure 6.2, the spinodal for each value of f lies completely in the gel region.

While this mean field analysis provides a neat picture of phase separation and gelation, there are a number of problems with it. Firstly, it neglects the presence of any rings or loops in the system and assumes that only tree-like products are possible [122]. Such a picture of gelation is unphysical as it requires diverging concentrations of polymers for macroscopic sized gels. Additionally, the mean field predictions neglects all concentration fluctuations in the system which will certainly affect both the reaction equilibrium and

phase separation. In the next section we pursue an approximate analytical approach to investigate the effect of fluctuations.

6.3.2 Random Phase Approximation

The random phase approximation (RPA) assumes that the system fluctuates around the saddle point and that the magnitude of these fluctuations are small. This allows expansion of the Hamiltonian around the saddle point state and truncation at Gaussian order, yielding a set of functional integrals that can be performed analytically. Execution of this approach yields the RPA approximation to the free energy

$$F_{\mathrm{RPA}} = F_{\mathrm{MF}} + \frac{V}{2(2\pi)^d}\int d\boldsymbol{k}\, \ln\left(\hat{\Delta}(\boldsymbol{k})\left(1 + BC\hat{\Gamma}(\boldsymbol{k})\hat{\Gamma}(-\boldsymbol{k})\hat{J}(\boldsymbol{k})\right)\right) \tag{6.22}$$

$$\hat{J}(\boldsymbol{k}) = \frac{1}{N_{\mathrm{tot}}} + f\hat{g}_D(\boldsymbol{k}) + f\frac{(f-1)\hat{h}_D(k)^2 + \eta_{\mathrm{MF}}\hat{\Phi}_b(\boldsymbol{k})\left(\frac{1}{N_{\mathrm{tot}}} + \hat{h}_D(\boldsymbol{k})\right)\left(\frac{1}{N_{\mathrm{tot}}} + \left(1 + 2(f-1)\hat{\Phi}(k)^{N_{\mathrm{arm}}}\right)\hat{h}_D(k)\right)}{\hat{\Delta}(\boldsymbol{k})} \tag{6.23}$$

$$\hat{\Delta}(\boldsymbol{k}) = 1 - \eta_{\mathrm{MF}}(f-1)\hat{\Phi}_b(\boldsymbol{k})\left(\hat{\Phi}(\boldsymbol{k})\right)^{2N_{\mathrm{arm}}} \tag{6.24}$$

$$\hat{g}_D(\boldsymbol{k}) = \frac{2}{N_{\mathrm{tot}}^2}\sum_{j=1}^{N_{\mathrm{arm}}}(N_{\mathrm{arm}} + 1 - j)\left(\hat{\Phi}(\boldsymbol{k})\right)^j \tag{6.25}$$

$$\hat{h}_D(\boldsymbol{k}) = \frac{1}{N_{\mathrm{tot}}}\sum_{j=1}^{N_{\mathrm{arm}}}\left(\hat{\Phi}(\boldsymbol{k})\right)^j \tag{6.26}$$

Notably, in the case of no reactions $\eta_{\mathrm{MF}} = 0$, eq 6.22 recovers the RPA free energy for a solution of homopolymer stars, as expected. For reactive systems, there are two additional terms that make important contributions to the free energy. The first is associated with the term Δ which acts as a normalization term based on proximity to the mean field gel point. At the mean field gel point $\Delta(0) = 1$ and the RPA correction

to the free energy would seemingly diverge as eq 6.22 contains $\ln(\Delta)$. There is another term in the free energy correction J that accounts for correlations between chains that is proportional to Δ^{-1} and keeps the free energy finite at and beyond the gel point. In particular J includes correlations between arms of the star both on the same molecule as well as from supramolecular interactions with different molecules, both of which are characterized by $h_D(k)$. The final contribution to J is from interactions between beads on the same arm, which are associated with $g_D(k)$.

The free energy expression is predicated on expansion around a single homogeneous phase, and one can use the free energy to determine the stability limits of the phase to obtain the spinodal. This analysis yields the same results as computing the structure factor with Gaussian fluctuations. One can show that any instability in the free energy will start at $k = 0$, indicating macroscopic phase separation. The condition for such an instability to occur is

$$1 - \eta_{\mathrm{MF}}(f-1) + BC(\eta_{\mathrm{MF}}+1) \leq 0 \tag{6.27}$$

which corresponds to the spinodal region in Figure 6.1. We can also use the free energy to obtain other operators of interest, including the reaction conversion, pressure, and chemical potential

$$\begin{aligned}\eta_{\mathrm{RPA}} = \eta_{\mathrm{MF}} \\ &+ \frac{\eta_{\mathrm{MF}}(1-\eta_{\mathrm{MF}})}{fC(1+\eta_{\mathrm{MF}})(2\pi)^d}\left(\int d\boldsymbol{k}\, \frac{(f-1)\hat{\Phi}_b(\boldsymbol{k})\hat{\Phi}(\boldsymbol{k})^{2N_{\mathrm{arm}}}(1+BC\hat{\Gamma}(\boldsymbol{k})^2(N_{\mathrm{tot}}^{-1}+f\hat{g}_D(\boldsymbol{k})))}{\hat{\Delta}(1+BC\hat{\Gamma}(\boldsymbol{k})^2\hat{J}(\boldsymbol{k}))}\right. \\ &\left. - \int d\boldsymbol{k}\, \frac{fBC\hat{\Gamma}(\boldsymbol{k})^2\hat{\Phi}_b(\boldsymbol{k})(\frac{1}{N_{\mathrm{tot}}}+\hat{h}_D(\boldsymbol{k}))(\frac{1}{N_{\mathrm{tot}}}+(1+2(f-1)\hat{\Phi}(\boldsymbol{k})^{N_{\mathrm{arm}}})\hat{h}_D(\boldsymbol{k}))}{\hat{\Delta}(1+BC\hat{\Gamma}(\boldsymbol{k})^2\hat{J}(\boldsymbol{k}))}\right)\end{aligned} \tag{6.28}$$

$$\beta R_g^3 \Pi_{\mathrm{RPA}} = \beta R_g^3 \Pi_{\mathrm{MF}} - \frac{1}{2}(\eta_{\mathrm{RPA}} - \eta_{\mathrm{MF}}) f C - \frac{1}{2(2\pi)^d} \int d\boldsymbol{k} \left(\ln\left(\hat{\Delta}(1 + BC\hat{\Gamma}(k)^2 \hat{J}(\boldsymbol{k})) \right) - \frac{BC\hat{\Gamma}(k)^2 \hat{J}(\boldsymbol{k})}{1 + BC\hat{\Gamma}(k)^2 \hat{J}(\boldsymbol{k})} \right) \tag{6.29}$$

$$\beta \mu_{\mathrm{RPA}} = \beta \mu_{\mathrm{MF}} - \frac{f}{2}(\eta - \eta_{\mathrm{MF}}) + \frac{1}{2(2\pi)^d} \int d\boldsymbol{k} \, \frac{B\hat{\Gamma}(\boldsymbol{k})^2 \hat{J}(\boldsymbol{k})}{1 + BC\hat{\Gamma}(\boldsymbol{k})^2 \hat{J}(\boldsymbol{k})} \tag{6.30}$$

There are two contributions to the fluctuation correction to η that are of opposite sign. The first increases η and accounts for the possible formation of intramolecular bonds, which is associated with $\hat{\Phi}_b \hat{\Phi}^{2N_{\mathrm{arm}}}$. Intramolecular bonds must form rings, and are thus not accounted for in mean field theory. The other fluctuation correction is responsible for excluded volume interactions between arms, which disfavors product formation as reacting stars together will increase unfavorable interactions due to proximity. It is important to note that η_{RPA} no longer depends only on the groupings BC and K/B as there is a bare C that appears in the coefficient to the fluctuation correction. This indicates that the universal mean field phase diagram will be disrupted by fluctuations. Finally, we note that the fluctuation corrections are both proportional to $\eta_{\mathrm{MF}}(1 - \eta_{\mathrm{MF}})$. When the mean field conversion is near unity, the fluctuation corrections will be significantly smaller than η_{MF}, however when η_{MF} is small the corrections will be of similar order. We can take this logic to the extreme and examine $C \to 0$ where η_{MF} is very small. This yields

$$\lim_{C \to 0} \eta_{\mathrm{RPA}} = \frac{K(f-1)}{(2\pi)^d} \int d\boldsymbol{k} \, \hat{\Phi}_b(\boldsymbol{k}) \left(\hat{\Phi}(\boldsymbol{k}) \right)^{2N_{\mathrm{arm}}} \tag{6.31}$$

Eq 6.31 shows that at small C the conversion saturates to a finite value. This is in contrast to the mean field case where η goes to zero for small C. The k integral in eq 6.31 is associated with the probability of two arms from the same molecule linking together due to the $2N_{\mathrm{arm}}$ factors of Φ and the single factor of Φ_b. This is to be expected as at very dilute concentrations the only type of bond formation should be intramolecular. The k

integral is further multiplied by $f-1$ and K which makes sense as increasing the number of arms or equilibrium constant should further favor bond formation. Unfortunately we also see the first failure of the RPA method here. In the small C limit, η_{RPA} is not bounded from above and can reach arbitrarily large values for large K despite the conversion η by definition being limited to the range $[0,1]$. Unfortunately, this issue limits the utility of the RPA approach around the dilute branch of the binodal. Nevertheless, we continue with our discussion of RPA corrections to other physical quantities before moving to alternative analysis modes.

The RPA corrections to the pressure and chemical potential follow forms similar to an unreactive solution of star polymers, but with the reaction corrected correlation function replacing the unreactive version. There are also corrections due to the conversion as seen in the terms proportional to $\eta_{\mathrm{RPA}}-\eta_{\mathrm{MF}}$. As previously discussed, RPA makes unphysical predictions for the conversion at large K and small C, which will propagate to the RPA corrected pressure and chemical potential. While in principle we could use the RPA chemical potential and pressure to compute corrections to the binodal, we do not do so due to the unphysical values of conversion that can appear.

As discussed previously, RPA only considers fluctuations to Gaussian order. One explanation for the unphysical predictions of RPA is that higher order fluctuations would partially cancel the contributions from Gaussian fluctuations and maintain physical values of the conversion. In principle one could perform one-loop calculations [122, 142] to evaluate this hypothesis. Rather than further pursue this analytical approach, we instead turn to numerical approaches.

6.4 Field Theoretic Simulations

The standard numerical approach for simulation of complex-valued field theories such as the one presented in eq 6.2 is to use the complex Langevin (CL) method [16, 29, 30]. This approach exactly samples the probability distribution consistent with Hamiltonian and includes fluctuations at all orders. Previous authors have presented algorithms to conduct CL-based FTS for AF theories [16] and pure CS theories of continuous Gaussian polymers [42]. We extend these algorithms to the hybrid AF-CS theory with discrete bead-spring polymers used here. The fields are evolved in fictitious time according to the stochastic differential equations

$$\partial_t W(\boldsymbol{r},t) = -\lambda_w \frac{\delta H}{\delta W(\boldsymbol{r},t)} + \eta_w(\boldsymbol{r},t) \tag{6.32}$$

$$\partial_t \phi_j(\boldsymbol{r},t) = -\lambda_{\phi_j} \frac{\delta H}{\delta \phi_j^*(\boldsymbol{r},t)} + \eta_{j,1}(\boldsymbol{r},t) + i\eta_{j,2}(\boldsymbol{r},t) \tag{6.33}$$

$$\partial_t \phi_j^*(\boldsymbol{r},t) = -\lambda_{\phi_j} \frac{\delta H}{\delta \phi_j(\boldsymbol{r},t)} + \eta_{j,1}(\boldsymbol{r},t) - i\eta_{j,2}(\boldsymbol{r},t) \tag{6.34}$$

The first term on the right hand side of each equation is referred to as the force as it is a deterministic term based on the variation of the Hamiltonian. It carries a positive constant mobility λ_w or λ_ϕ. Each equation also carries a noise term that obey

$$\langle \eta_w(\boldsymbol{r},t)\rangle = 0 \tag{6.35}$$

$$\langle \eta_{j,p}(\boldsymbol{r},t)\rangle = 0 \tag{6.36}$$

$$\langle \eta_w(\boldsymbol{r},t)\eta_w(\boldsymbol{r}',t')\rangle = 2\lambda_w \delta(\boldsymbol{r}-\boldsymbol{r}')\delta(t-t') \tag{6.37}$$

$$\langle \eta_w(\boldsymbol{r},t)\eta_{j,p}(\boldsymbol{r}',t')\rangle = 0 \tag{6.38}$$

$$\langle \eta_{j,p}(\boldsymbol{r},t)\eta_{k,q}(\boldsymbol{r}',t')\rangle = \lambda_\phi \delta_{j,k}\delta_{p,q}\delta(\boldsymbol{r}-\boldsymbol{r}')\delta(t-t') \tag{6.39}$$

while any noise that has these means and variances can be used, we exclusively use Gaussian white noise in this work.

To conduct a numerical simulation, the time variable must be discretized. Based on previous work, we use a semi-implicit scheme [21, 26, 42, 101] where the linear part of the force is treated implicitly while all non-linear contributions are treated explicitly. Substituting in the proper expressions for the force yields the scheme

$$W^{l+1}(\boldsymbol{r}) - W^{l}(\boldsymbol{r}) = -\lambda_w \Delta t \left(\frac{W^{l+1}(\boldsymbol{r})}{B} - iC + iC \int d\boldsymbol{r}'\, \Gamma(\boldsymbol{r}-\boldsymbol{r}')\tilde{\rho}^{l}(\boldsymbol{r}') \right) + R^{l}_{w}(\boldsymbol{r}) \tag{6.40}$$

$$\begin{aligned} \phi_0^{l+1}(\boldsymbol{r}) - \phi_0^{l}(\boldsymbol{r}) = &-\lambda_\phi \Delta t \left(\phi_0^{l+1}(\boldsymbol{r}) - fC \frac{(\phi_0^{*l}(\boldsymbol{r}))^{f-1} e^{-i\Gamma * W^{l+1}(\boldsymbol{r})}}{\frac{R_g^3}{V} \int d\boldsymbol{r}\, (\phi_0^{*l}(\boldsymbol{r}))^{f} e^{-i\Gamma * W^{l+1}(\boldsymbol{r})}} \right) \\ &+ R^{l}_{0,1}(\boldsymbol{r}) + iR^{l}_{0,2}(\boldsymbol{r}) \end{aligned} \tag{6.41}$$

$$\begin{aligned} \phi_j^{l+1}(\boldsymbol{r}) - \phi_j^{l}(\boldsymbol{r}) = &-\lambda_\phi \Delta t \left(\phi_j^{l+1}(\boldsymbol{r}) - e^{-i\Gamma * W^{l+1}(\boldsymbol{r})} \int d\boldsymbol{r}'\, \Phi(\boldsymbol{r}-\boldsymbol{r}') \phi_{j-1}^{l+1}(\boldsymbol{r}') \right) \\ &+ R^{l}_{j,1}(\boldsymbol{r}) + iR^{l}_{j,2}(\boldsymbol{r}) \end{aligned} \tag{6.42}$$

$$\phi_{N_{\text{arm}}}^{*l+1}(\boldsymbol{r}) - \phi_{N_{\text{arm}}}^{*l}(\boldsymbol{r}) = -\lambda_\phi \Delta t \left(\phi_{N_{\text{arm}}}^{*l+1}(\boldsymbol{r}) - 1 \right) + R^{l}_{N_{\text{arm}},1}(\boldsymbol{r}) - iR^{l}_{N_{\text{arm}},2}(\boldsymbol{r}) \tag{6.43}$$

$$\begin{aligned} \phi_j^{*l+1}(\boldsymbol{r}) - \phi_j^{*l}(\boldsymbol{r}) = &-\lambda_\phi \Delta t \left(\phi_j^{*l+1}(\boldsymbol{r}) - \int d\boldsymbol{r}'\, \Phi(\boldsymbol{r}-\boldsymbol{r}') \phi_{j+1}^{*l+1}(\boldsymbol{r}') e^{-i\Gamma * W^{l+1}(\boldsymbol{r}')} \right) \\ &+ R^{l}_{j,1}(\boldsymbol{r}) - iR^{l}_{j,2}(\boldsymbol{r}) \end{aligned} \tag{6.44}$$

here superscript l indicates a discrete time index and Δt is the time step. The continuous-time noise terms η have been replaced with discrete-time noise R which follow similar

statistics

$$\langle R_w^l(\boldsymbol{r})\rangle = 0 \tag{6.45}$$

$$\langle R_{j,p}^l(\boldsymbol{r})\rangle = 0 \tag{6.46}$$

$$\langle R_w^l(\boldsymbol{r})R_w^m(\boldsymbol{r}'')\rangle = 2\lambda_w \Delta t \delta(\boldsymbol{r}-\boldsymbol{r}')\delta_{l,m} \tag{6.47}$$

$$\langle R_w^l(\boldsymbol{r})R_{j,p}^m(\boldsymbol{r}'')\rangle = 0 \tag{6.48}$$

$$\langle R_{j,p}^l(\boldsymbol{r})R_{k,q}^m(\boldsymbol{r}'')\rangle = \lambda_\phi \Delta t \delta_{j,k}\delta_{p,q}\delta(\boldsymbol{r}-\boldsymbol{r}')\delta_{l,m} \tag{6.49}$$

With the numerical scheme fully defined, we first apply it to an unreactive solution of star polymers. This model can be represented with both AF and CS models and serves as a validation to the CS approach. Unfortunately, initial results show that the CS model does not reproduce the AF result, indicating a problem with the sampling scheme. Figure 6.3 shows one example of this mismatch. CL-FTS were conducted in a three dimensional cubic box with side length $3.2\,R_g$. Space was discretized with 16^3 grid points and periodic boundary conditions were employed. The polymers had $f = 3$ and $N_{\text{arm}} = 9$ and dimensionless concentration $C = 10$. The mobility parameters were set to $\lambda_w = 1$ and $\lambda_{\phi_j} = 0.1$ for all j. The time step was $\Delta t = 0.01$ and simulations were run for two million iterations.

In principle the simulations should produce identical results as they utilize the same numerical discretizations and the models are analytically equivalent. For small values of B the agreement is reasonably good and the averages computed with each method are within the error bar of each other. As B is increased above 1, however, the CS averages begin to diverge from AF for both the pressure and the chemical potential. There is likely a problem in the sampling of the CS fields ϕ and ϕ^* or an error in implementation of the method. Further investigation is necessary to conduct meaningful FTS. Because

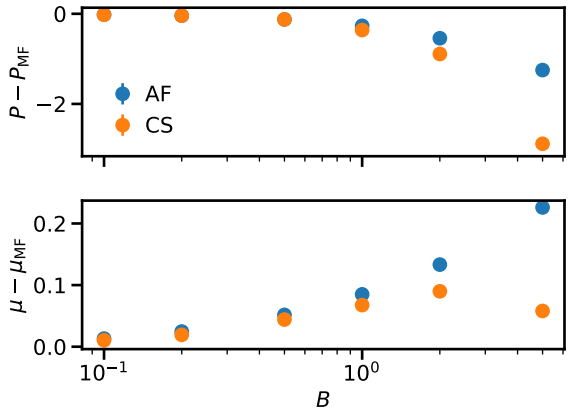

Figure 6.3: Fluctuation correction to pressure (top) and chemical potential (bottom) for a solution of three arm homopolymer stars over a range of interaction strengths B. Blue points indicate results from AF simulations while orange points were obtained from CS simulations.

of this sampling error, we do not conduct FTS for reactive star polymers.

6.5 Conclusions

We have constructed a coherent states models of reactive homopolymer stars in solution and applied approximate analytical analysis techniques to interrogate phase behavior and gelation. At the mean-field level this model reproduces the Flory-Stockmayer result for gelation. In this particular bonding scheme, the system can phase separate into a polymer-lean supernatant and a polymer rich gel, but spinodal decomposition can only occur after gelation. RPA calculations were used to examine fluctuations about the mean field state, which revealed competing corrections to the reaction equilibrium. RPA was shown to produce unphysical results for dilute concentrations and large equilibrium constant, likely due to missing higher order corrections. Attempts at exactly evaluating fluctuation corrections with numerical simulations have thus far been unsuccessful.

Chapter 7

Conclusions and Outlook

I have demonstrated here how to efficiently conduct field theoretic simulations (FTS) and self-consistent field theory (SCFT) calculations for both auxiliary field (AF) and coherent states (CS) field theory models. In the case of SCFT, linear response kernels can be used to create semi-implicit algorithms that stabilize fictitious dynamics search algorithms so that they converge under a broad range of numerical parameter values [17]. This stability does not translate to speed, however. When tune correctly, predictor-corrector algorithms can converge significantly faster than first order methods that use linearly response information, even though the predictor-corrector methods are far less stable. Finally, for calculations of highly symmetric systems, and Anderson mixing [18] approach can be used that is as efficient as predictor-corrector algorithms.

For FTS, semi-implicit algorithms perform well in disordered phases, where an accurate linear response kernel can be computed. Predictor-corrector algorithms that use linear response information are both the most stable and most accurate in disordered phases. For ordered systems such as polymer microphases, adaptive time stepping is crucial to achieving a stable algorithm, and can allow access to physical parameter ranges that have been considered intractable. These insights are already being employed in the

Fredrickson group to more efficiently conduct FTS of polymers. Unfortunately, there remain unresolved issues, including the unphysical saddle point problem outlined here. These unphysical saddle points appear to be a property of extending field theory models into the complex plane. Although not discussed here, there is also a known issue in FTS termed the "core repulsion" problem where at strong interaction strengths, CL sampling produces incorrect results. The unphysical saddle point problem is also exacerbated at strong interaction strengths, but it is unclear if the two problems are related. Nevertheless, it is still possible to obtain physically meaningful insights from FTS and SCFT as long as one is aware of these issues.

We first applied the SCFT approach to linear, comb-like, and bottlebrush diblock copolymers. We were able to construct a universal phase diagram for these architectures using the idea of conformational symmetry and relating it to architectural parameters. This phase diagram includes the Frank-Kasper A15 and σ tetrahedrally close-packed sphere phases, which had not been previously demonstrated for all the architectures considered here. We also performed calculations using very large polymers with side chains as long as thirty beads and grafting densities as high as two. These molecules behaved like combs rather than bottle brushes, despite experimental analogs displaying strong bottlebrush behavior [37]. We rationalize this discrepancy via the mean-field approximation of SCFT and comment on the current limitations preventing observation of bottlebrush behavior in SCFT.

We then shifted our focus to supramolecular polymers that undergo reversible reactions. The power of CS models was demonstrated via the ability to compute phase diagrams that include three dimensional microphases and simultaneously examine the reaction equilibrium. We showed that exotic phase behavior can be obtained with binary blends of heterobonding telechelic homopolymers, but we were also able to rationalize these trends via the stoichiometry and reaction equilibrium. As a final task we attempted

to study network formation and phase separation in solutions of end-linking star polymers. At the mean-field level the models considered here are consistent with classical Flory-Stockmayer theory and analytical approximations to the fluctuations indicate that the model also captures effects from loops. Unfortunately, numerical simulations have thus far produced results that are inconsistent with known results from unreactive polymer models, so the fully fluctuating network picture could not be examined. We hope that future work may overcome these obstacles and conduct FTS for these network systems.

Appendix A

FTS Algorithm Details

A.1 Forces for diblock copolymer melt

To conduct SCFT or FTS calculations one must evaluate the forces, $\delta H[w]/\delta w(\boldsymbol{r})$. For the diblock model considered here the forces are

$$\frac{\delta H[w_+, w_-]}{\delta w_+(\boldsymbol{r})} = \frac{2C}{2\zeta N + \chi N} w_+(\boldsymbol{r}) + iC\Gamma * (\tilde{\rho}_A(\boldsymbol{r}) + \tilde{\rho}_B(\boldsymbol{r})) - \frac{2iC\zeta N}{2\zeta N + \chi N} \tag{A.1}$$

$$\frac{\delta H[w_+, w_-]}{\delta w_-(\boldsymbol{r})} = \frac{2C}{\chi N} w_-(\boldsymbol{r}) + C\Gamma * (\tilde{\rho}_B(\boldsymbol{r}) - \tilde{\rho}_A(\boldsymbol{r})) \tag{A.2}$$

The density operators $\tilde{\rho}_A(\boldsymbol{r})$ and $\tilde{\rho}_B(\boldsymbol{r})$ both have implicit functional dependence on the fields w_+ and w_-. They are computed from the propagator according to

$$\tilde{\rho}_A(\boldsymbol{r}) = \frac{1}{Q[w_+, w_-]} \int_0^f ds\, q_c(\boldsymbol{r}, 1-s) q(\boldsymbol{r}, s) \tag{A.3}$$

$$\tilde{\rho}_B(\boldsymbol{r}) = \frac{1}{Q[w_+, w_-]} \int_f^1 ds\, q_c(\boldsymbol{r}, 1-s) q(\boldsymbol{r}, s) \tag{A.4}$$

where $q_c(\boldsymbol{r}, s)$ is the conjugate propagator to $q(\boldsymbol{r}, s)$ and represents the field-based random walk statistics of the polymer starting from the opposite end as q. The conjugate

propagator is computed according to the equations

$$q_c(\boldsymbol{r}, 0) = 1 \tag{A.5}$$

$$\partial_s q_c(\boldsymbol{r}, s) = \nabla^2 q_c(\boldsymbol{r}, s) - w(\boldsymbol{r}, 1-s) q_c(\boldsymbol{r}, s) \tag{A.6}$$

Note that these equations are nearly identical to the equations for q from the main text, but the contour dependence of w has changed from s to $1 - s$. The definition for w is given in the main text.

The semi-implicit algorithms such as SI1 and ETD1 considered in this work rely on a linearization of the forces

$$\begin{aligned}\frac{\delta H[w_+, w_-]}{\delta w_+(\boldsymbol{r})} &= c_+ * w_+(\boldsymbol{r}) + \mathcal{O}(w_+^2) \\ \frac{\delta H[w_+, w_-]}{\delta w_+(\boldsymbol{r})} &= c_- * w_-(\boldsymbol{r}) + \mathcal{O}(w_-^2)\end{aligned}$$

For the diblock copolymer considered here the correlation functions are

$$\begin{aligned}\hat{c}_+(k) &= \frac{2C}{2\zeta N + \chi N} + C\Gamma(k)^2 \left(\hat{g}_D(k^2 f) + 2\hat{h}_D(k^2 f)\hat{h}_D(k^2(1-f)) + \hat{g}_D(k^2(1-f))\right) \\ \hat{c}_-(k) &= \frac{2C}{\chi N} - C\Gamma(k)^2 \left(\hat{g}_D(k^2 f) - 2\hat{h}_D(k^2 f)\hat{h}_D(k^2(1-f)) + \hat{g}_D(k^2(1-f))\right)\end{aligned}$$

with the Debye-like functions defined as

$$\begin{aligned}\hat{g}_D(x) &= \frac{2}{x^2}\left(x + e^{-x} - 1\right) \\ \hat{h}_D(x) &= \frac{1}{x}\left(1 - e^{-x}\right)\end{aligned}$$

Using these correlation functions semi-implicitly is only stabilizing if they are positive

definite. The function c_+ satisfies this, but c_- does not, so we make the truncation

$$\hat{c}_-(k) = \frac{2C}{\chi N} \tag{A.7}$$

A.2 Complex Langevin algorithm error scaling

We show numerically that the algorithms considered in this work have the expected error scaling. We use the data from Figure 2.6 and compute the error relative to a reference "exact" solution. Unfortunately no analytical exact solution is available, so we instead use the average of the chemical potential values computed from the EMPEC2, PO2 and ETDRK2 algorithms at $\Delta t = 10^{-3}$. We denote this approximate "exact" value as $\bar{\mu}_{\text{ex}}$. The EMPEC2, PO2 and ETDRK2 algorithms should have the best error scaling and $\Delta t = 10^{-3}$ is the smallest time step considered, so the errors relative to the exact value should be smallest for the values used to compute $\bar{\mu}_{\text{ex}}$. The deviation between the estimated value of chemical potential and $\bar{\mu}_{\text{ex}}$ are shown in Figure A.1. The original estimates for the chemical potential all have uncertainty due to the stochastic nature of the simulation. This uncertainty is quantified by the standard error of the mean, which for all data points is less than $5.1 * 10^{-5}$. This uncertainty level is indicated via a horizontal gray dashed line in Figure A.1. Below this line the calculated error is not significant compared to the uncertainty in the chemical potential.

For the EM1 and SI1 algorithms the error relative to $\bar{\mu}_{\text{ex}}$ is always above the uncertainty line and the data shows a clear first order relation between the error and the time step Δt as expected. For the ETD1 method there is also evidence of first order scaling for data points with $\Delta t \geq 10^{-2}$, but for smaller Δt values the error falls below the uncertainty line and the trend breaks. For the second order methods it is much more difficult to discern trends because most of the data lies under the uncertainty line where

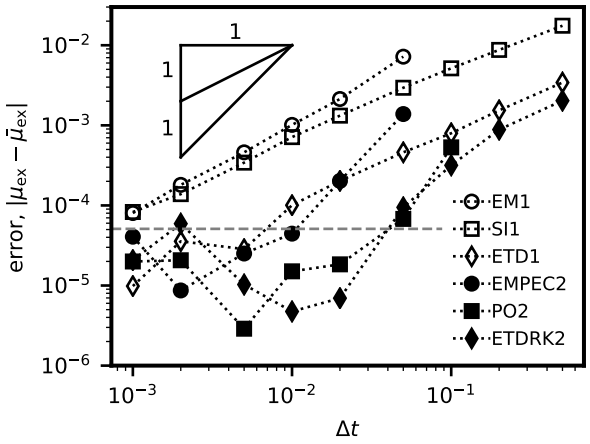

Figure A.1: Error in CL estimate for chemical potential μ_{ex} versus time step for a disordered melt at $\chi N = 10$. The reference value for μ_{ex} is the average of the EMPEC2, PO2 and ETDRK2 values at $\Delta t = 10^{-3}$. The horizontal dashed gray line indicates the approximate standard error of the mean for μ_{ex}.

it is not significant. For the EMPEC2 data the three points in $10^{-2} \leq \Delta t \leq 5 * 10^{-2}$ fit a second order error scaling law, but only there are only three data points in the trend. We expect that decreasing the uncertainty of μ_{ex} should lead to clear second order scaling trends, but the computational cost increases by orders of magnitude to achieve this, so we do not further pursue it.

A.3 Divergent trajectories

A complex Langevin simulation can become divergent when the fields attain values of IEEE 754-defined +INF, -INF or NAN. To better understand these events, we monitored the instantaneous value of the fields over time. The w_+ field was Wick rotated so that it is purely real at the saddle point, and we refer to it as iw_+ to be consistent with the model presented in the main text. Figure A.2 shows the largest magnitude of any element over the spatial grid for each field. The real and imaginary part of each field has a typical value it fluctuates around until the end of the simulation where the real part of

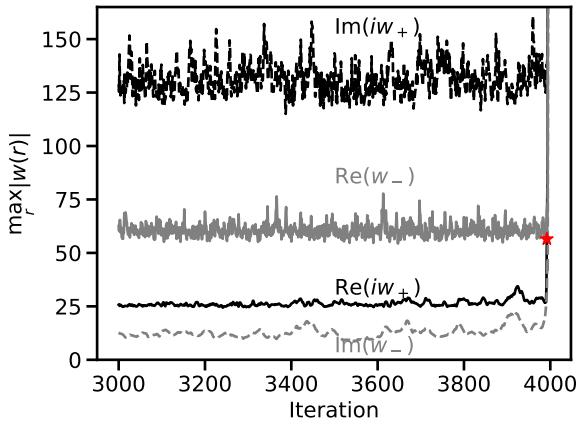

Figure A.2: Maximum absolute value of each component of the fields over a single trajectory. The simulation was conducted at $\chi N = 30$, $\zeta N = 100$, $C = 20$ in a cubic box of size $V = 9^3\, R_g^3$ with $M = 48^3$. The ETDRK2 algorithm was used with $\Delta t = 0.1$.

the iw_+ field and the imaginary part of the w_- field both have a maximum value that grows exponentially quickly. We further probe what occurs here by visualizing the fields near the end of the trajectory. A two dimensional slice of each field from iteration 3992 (indicated with a red star in Figure A.2) is shown in Figure A.3. The real parts of each field show patterns typical of the double gyroid phase. The imaginary part of iw_+ and the real part of w_- both also show local noise, which is to be expected because noise is applied to these two parts of the field during a CL step. Finally, the real part of iw_+ and the imaginary part of w_- both show large negative values in the upper left corner of the image. The color scale is set in order to have some detail in other parts of the image, but there is large negative spike of values in the upper left corner for these two parts of the fields. Further investigation reveals that these two field components are also experiencing local forces in the upper left corner that are pushing the fields to further negative values. Apparently the trajectory is on a path of exponential growth of a local negative value in $\mathrm{Re}(iw_+)$ and $\mathrm{Im}(w_-)$. As a final note, this local spike in the field seems to be located on the interface between the A domain and the B domain.

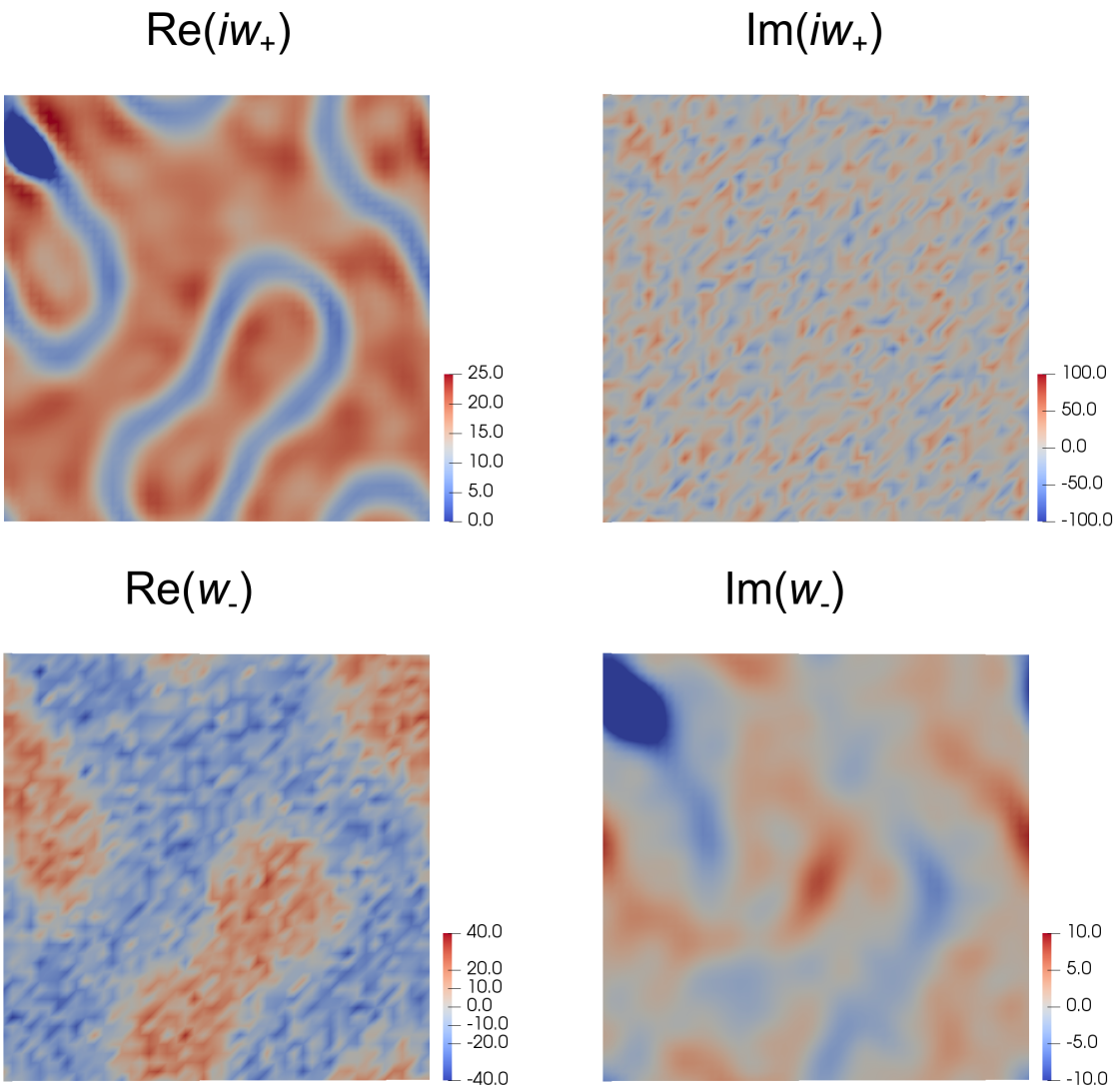

Figure A.3: Two dimensional slice of each of the fields from iteration 3992 in Figure A.2 (indicated with a red star).

A.4 Basin escape and unphysical, non-ergodic trajectories

A second failure mode for CL trajectories is also possible. Rather than diverging, it is possible for the fields to leave the basin of attraction for the local saddle point of interest (in our case the double gyroid structure) and enter a basin of attraction for a different saddle point because there are numerous saddle points present. One possible occurrence of this phenomena observed in these studies is a transition from the double gyroid phase to the hexagonally perforated lamellar phase. Such transitions between two different microphases are usually rare and are quite obvious when visualizing densities or examining the trajectory of operators. Simulations where a transition between phases occurs should typically be disregarded. It is also possible, however, for the fields to transition into a basin of attraction for an *unphysical* saddle point. Such saddle points are characterized by non-zero imaginary components for field operators, such as the density or Hamiltonian. These saddle points are termed "unphysical" because operators must average to purely real values in physical systems. Figure A.4 shows the Hamiltonian and excess chemical potential operators in a CL simulation where multiple unphysical basins are sampled. The imaginary part of the Hamiltonian initially fluctuates around zero, but after approximately 1000 units of CL time, there is a sharp transition and $\mathrm{Im}(H)$ begins to fluctuate around a negative value. Three more transitions occur throughout the simulation. For all data presented in the main text, trajectories that sampled unphysical basins were ignored. The unphysical basin phenomenon was not observed in the disordered phase at $\chi N = 10$.

Visualizing the fields again provides useful information. Figure A.5 shows a two dimensional slice of each component of the fields from the end of the simulation. In $\mathrm{Re}(iw_+)$ there are two "defects" on the interface between the A and B domains. These

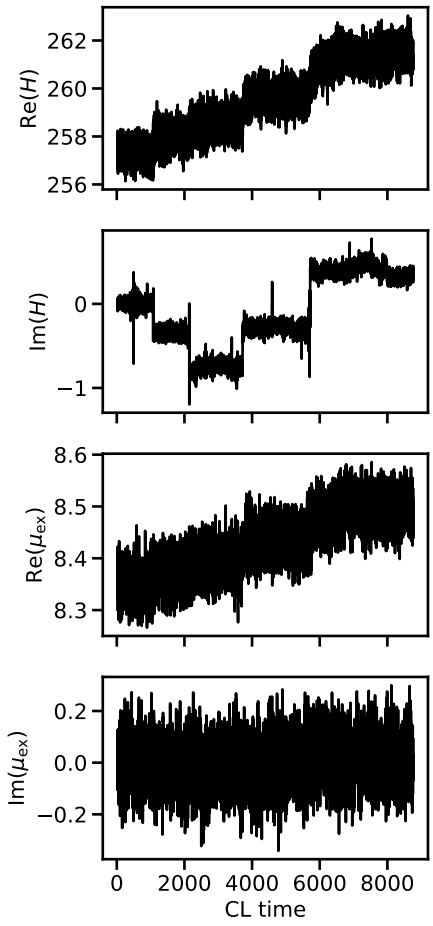

Figure A.4: Hamiltonian, H, and chemical potential, μ_{ex}, operator values over a single trajectory. This trajectory samples a number of unphysical states where the Hamiltonian does not have average zero imaginary component. The simulation was conducted at $\chi N = 30$, $\zeta N = 100$, $C = 20$ in a cubic box of size $V = 9^3\, R_g^3$ with $M = 48^3$. The EM1ADT algorithm was used with $\Delta t = 0.005$.

defects are characterized by a large positive spike surrounded by a shell of large negative values. There are also signs of the defects in $\mathrm{Im}(iw_+)$, however one of them is a large spike of negative values while the other is a large spike of positive values. There are additional defects in the fields that are not shown in the slice, but examining all of them reveals that there are three defects with a positive spike in $\mathrm{Im}(iw_+)$, while there are two with a negative spike in $\mathrm{Im}(iw_+)$. Examining other trajectories that sample unphysical trajectories allows one to correlate the shift in the mean value of $\mathrm{Im}(H)$ with the number and sign of the defects present. Thus one can infer that each of the transitions present in Figure A.4 indicates a formation (or relaxation) of one of these defects. Notably it is possible for two defects with opposite sign to form and for there to be no shift in $\mathrm{Im}(H)$, however visualizing the density should always allow one to identify defects and realize that one is in an unphysical state. The imaginary part of the excess chemical potential continues to fluctuate around zero and is seemingly far less sensitive to these defects as compared to the Hamiltonian as seen in Figure A.4. The real part of the chemical potential drifts over the simulation, possibly due to the defects.

A final question remains of whether these defects represent actual saddle points with attractive basins or if they are simply a fluctuation induced state that relaxes back to the physical saddle point when noise is turned off. Figure A.6 shows the converged fields obtained from applying an SCFT relaxation starting from the fields in Figure A.5. Although SCFT typically is conducted with the restriction of purely real fields, in this case we start from complex fields and retain the real and imaginary parts through the entire calculation. As Figure A.6 shows, the defect structure is preserved, indicating that the defects represent an alternative unphysical saddle point to the double gyroid structure. If the same relaxation is performed, but setting the imaginary component of both fields to zero, then the fields instead relax to the physical saddle point with no defects. This indicates that these unphysical saddle points can only be encountered when

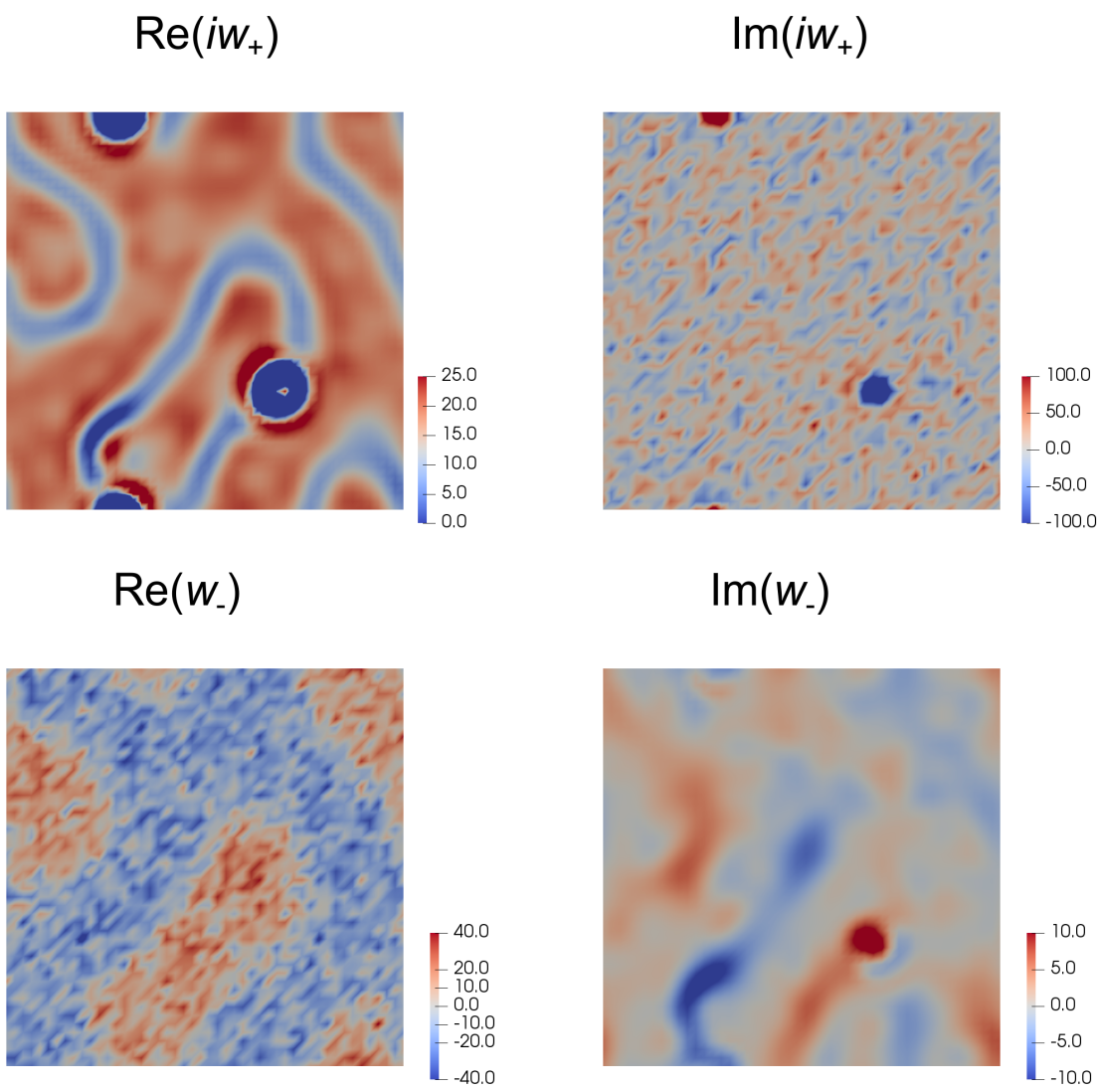

Figure A.5: Two dimensional slice of all the fields at the end of the trajectory in Figure A.4.

the fields are complexified. In SCFT we typically only consider real-valued fields (with appropriate Wick rotations for those that are purely imaginary at the saddle point) so it is impossible to encounter these unphysical saddle points.

A.5 A toy model for CL

To better understand the two failure modes previously presented, we construct a simple toy model. Furthermore, since the iw_+ field showed stronger signatures of the problems, we focus on it. The dynamics governing the iw_+ field in the full diblock model are

$$\partial_t iw_+(\boldsymbol{r},t) = \frac{-2C}{2\zeta N+\chi N} iw_+(\boldsymbol{r},t) + C\Gamma * (\tilde{\rho}_A(\boldsymbol{r}) + \tilde{\rho}_B(\boldsymbol{r})) - \frac{2C\zeta N}{2\zeta N+\chi N} + i\eta(\boldsymbol{r},t) \quad \text{(A.8)}$$

where the noise term $i\eta(\boldsymbol{r},t)$ is purely imaginary if the field is Wick rotated, as in eq A.8. The density operators, $\tilde{\rho}_A$ and $\tilde{\rho}_B$, both have functional dependence on both the iw_+ and w_- fields. The simplified dynamics we consider is instead:

$$\partial_t w(t) = -\frac{1}{a} w(t) + e^{-w(t)} - 1 + i\eta(t) \quad \text{(A.9)}$$

The field w now no longer has any spatial dependence, but the force retains a similar form to the full diblock polymer model. There is a term that is linear in w with parameter a that plays a role similar to the compressibility parameter ζN in the diblock model. The density operators have been replaced with a simple exponential function that is analogous to a density operator for a point particle rather than a polymer. Finally there is a constant, field independent term and a purely imaginary noise. We next extend w to complex values $w = x + iy$, which yields a two dimensional system of first order differential equations:

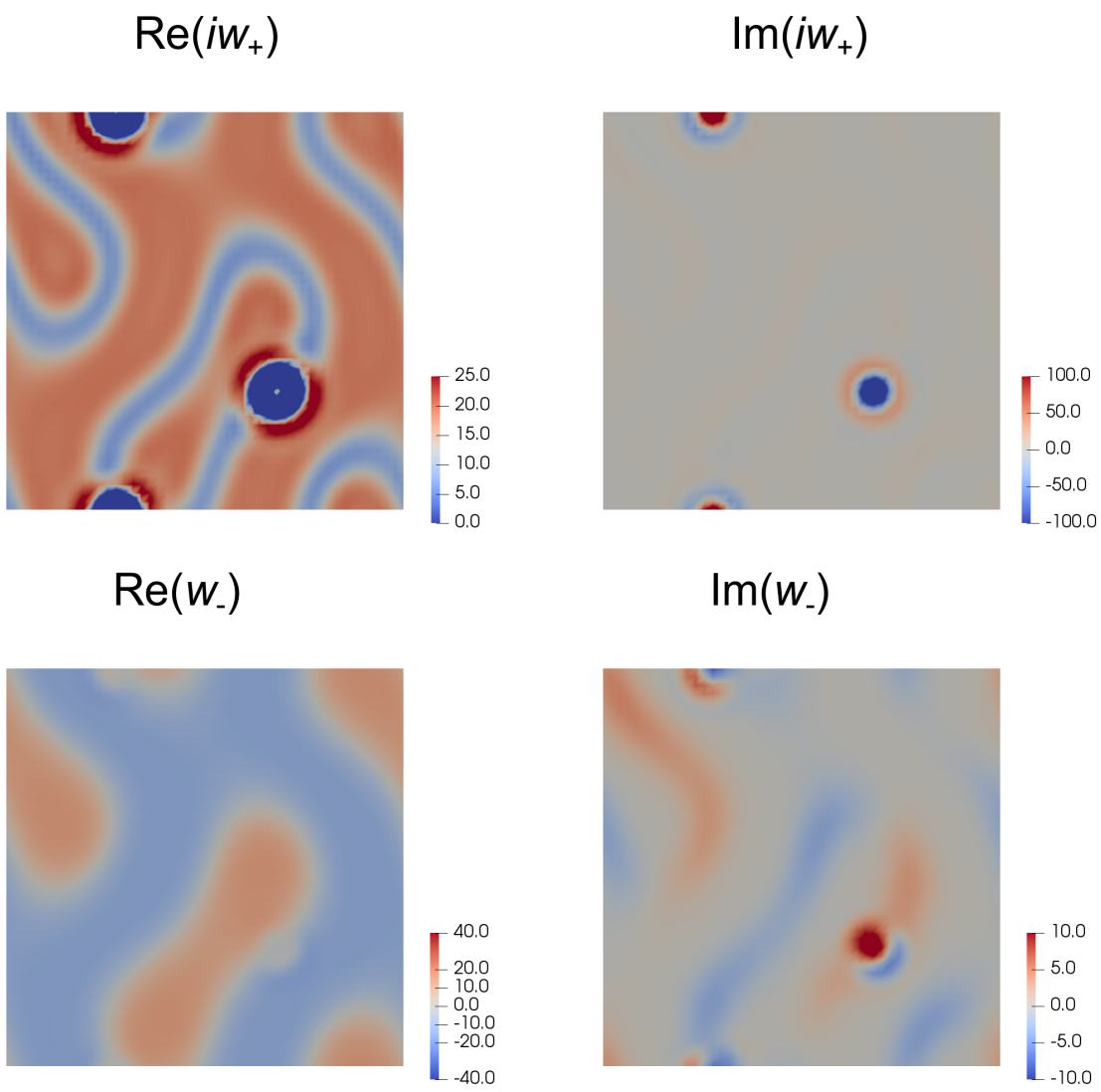

Figure A.6: Fields from Figure A.5 after being relaxed to the SCFT saddle point

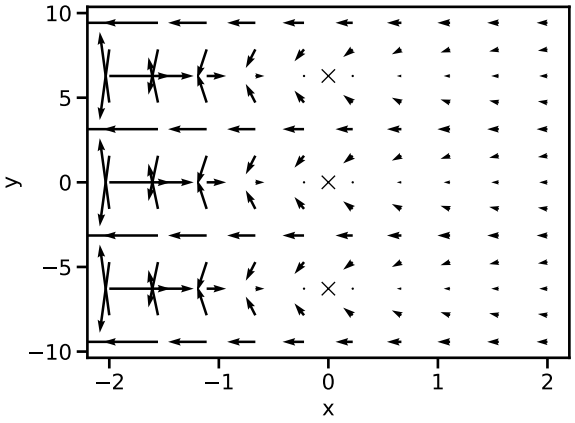

Figure A.7: Force field for the toy model at $a \to \infty$. The X marks indicate fixed points for the dynamics.

$$\partial_t x(t) = -\frac{1}{a}x(t) + e^{-x(t)}\cos(y) - 1 \tag{A.10}$$

$$\partial_t y(t) = -\frac{1}{a}y(t) - e^{-x(t)}\sin(y) + \eta(t) \tag{A.11}$$

The force profile for this system when the noise is turned off is shown in Figure A.7 ($a \to \infty$) and Figure A.8 ($a = 10$).

Figure A.7 shows that there are multiple fixed points present: a real, physical fixed point at $(0, 0)$, and imaginary, unphysical fixed points at $(0, n2\pi)$, where n is any non-zero integer. These points are marked with an X. These unphysical fixed points can have either positive or negative imaginary component, in analogy with the complex saddle points seen in the full diblock model. They also have their own basins of attraction.

There are trajectories present that have the real part of w diverge to negative infinity. These trajectories are located at $y = k\pi$, where k is any odd integer, and divide the basins of attraction between saddle points. These trajectories are analogous to the divergent trajectories seen in the diblock model, so the toy model seemingly captures the two failure

modes diagnosed with full CL simulations. One can understand why the failures occur. A CL calculation is typically initialized from a physical SCFT saddle point, in this case $(0, 0)$. The noise present in the system will move the current phase space position to $y \neq 0$, which then creates a force on x that pushes it to negative values. A large enough noise fluctuation can lead to $y \approx \pm\pi$, which creates an exponentially diverging force on x to negative infinity. The divergent trajectories have zero width and any fluctuation to either side places the system on a trajectory that is bounded but with very large force, which requires an extremely small time step to integrate accurately and avoid disaster. This reveals why the adaptive time stepping method is so effective. Most of the time the forces are of similar size, but occasionally a strong fluctuation places the system close to the divergent trajectory. Fixed time step algorithms will diverge in a few iterations because the forces are so large. The adaptive time steppers, however, will dramatically decrease the time step when these large forces occur, leading to accurate integration and sufficient time for fluctuations to occur to remove the fields from the divergent trajectory and return to close to the saddle point.

Another possible trajectory is a fluctuation that crosses the divergent trajectory into one of the non-physical basins. There is nothing in the adaptive time stepper to prevent this, and the ADT algorithms also suffer this problem.

As a final consideration we examine the force profile, but for $a = 10$. This is analogous to moving from an incompressible system to a system with finite compressibility. As can be seen from the equations, decreasing a leads to a stronger attractive force to the physical saddle point at $(0, 0)$. The force field has been disrupted and positions of the unphysical saddle points have shifted. The divergent trajectories are also disrupted and instead of going to negative infinity will eventually return to the physical saddle point. In the process, they can still sample very large negative values, however. These factors indicate that more-compressible systems may be easier to simulate than the incompressible

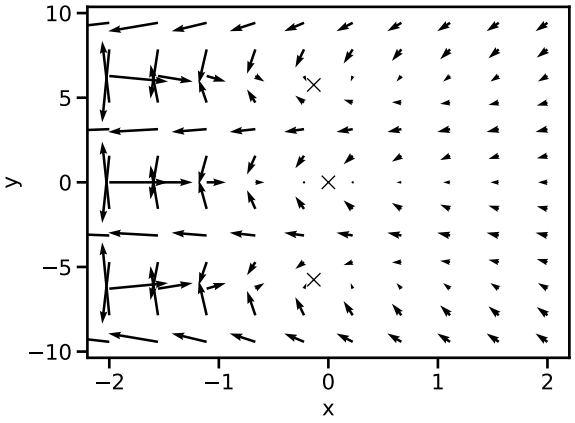

Figure A.8: Force field for the toy model at $a = 10$

variants.

A.6 Literature Summary

Table A.1: Summary of publications that compare different algorithms for SCFT simulations. MDE solver is the algorithm used to solve the modified diffusion equation for the chain propagator. A summary of these algorithms can be found elsewhere [24, 25, 70].

First author	Year	Field updater	MDE solver
Ceniceros [17]	2004	EM1	RK2
		SI1	RK2
Thompson [18]	2004	AM	RK2
		simple mixing	RK2
Cochran [19]	2006	SI1	CGF4
Matsen [22]	2009	AM	spectral
Jiang [23]	2010	SI1	spectral
		SI1	SMEP
Stasiak [24]	2011	AM	RK2
		AM	CGF4
		AM	RQM4
		AM	spectral
Audus [25]	2013	ETD1	RK2
		ETD1	CGF4
		ETD1	RQM4

Table A.2: Summary of publications that compare different algorithms for CL simulations. MDE solver is the algorithm used to solve the modified diffusion equation for the chain propagator. A summary of these algorithms can be found elsewhere [25].

First author	Year	Field updater	MDE solver
Lennon [21]	2008	EM1	CGF4
		SI1	CGF4
		PO2	CGF4
Audus [25]	2013	ETD1/EMPEC2	RK2
		ETD1/EMPEC2	CGF4
		ETD1/EMPEC2	RQM4
Villet [7]	2014	EM1	RQM4
		SI1	RQM4
		PO2	RQM4
		ETD1	RQM4
Düchs [26]	2014	EM1	RK2
		SI1	RK2
		ETD1	RK2
		EMPEC2	RK2
		PO2	RK2
		ETDPEC2	RK2

Appendix B

Bottlebrush SCFT Computational Details

B.1 Phase Diagram Details

We compute phase diagrams by calculating the free energy of candidate phases for different model parameters such as the Flory-Huggins interaction (χ), architecture, and volume fraction parameters. For discrete comb-like and bottlebrush copolymers, a limited set of points in the f_A and ϵ phase space were available. From these points we constructed a Delaunay triangulation to create a mesh over the entire phase space. Linear interpolation was then used to estimate the free energy over each triangle. Phase boundaries were computed by finding the intersection of the free energy surfaces.

While performing these calculations, we found that finer spatial resolutions were necessary to accurately resolve the free energies at high χN because both the domain spacing and segregation strength increase considerably. We utilize the primitive cell for some phases, which allows us to use fewer plane waves without accuracy loss. We show the resolutions and cell types used for different phases in Table B.1. Lequieu et al. previously

	Phase	Resolution	Cell Type
Comb	FCC	$64 \times 64 \times 64$	Cubic
Comb	BCC	$64 \times 64 \times 64$	Cubic
Comb	HEX	64×64	Primitive
Comb	A15	$64 \times 64 \times 64$	Cubic
Comb	σ	$128 \times 128 \times 64$	Orthorhombic
Linear	FCC	$64 \times 64 \times 64$	Cubic
Linear	BCC	$64 \times 64 \times 64$	Cubic
Linear	HEX	64×64	Primitive
Linear	A15	$64 \times 64 \times 64$	Cubic
Linear	σ	$128 \times 128 \times 64$	Orthorhombic
Bottlebrush	FCC	$32 \times 32 \times 32$	Primitive
Bottlebrush	BCC	$32 \times 32 \times 32$	Primitive
Bottlebrush	HEX	64×64	Primitive
Bottlebrush	A15	$64 \times 64 \times 64$	Cubic
Bottlebrush	σ	$192 \times 192 \times 96$	Orthorhombic

Table B.1: Resolutions and cell type used in study

showed that the primitive cell results produced identical results to conventional unit cells with smaller numbers of plane waves [92].

We used a higher number of plane waves for the bottlebrush polymer σ phases due to the increased size of the cells. We investigated higher resolutions for A15 (96^3) and BCC (64^3) and found negligible differences in both the free energies and phase boundaries.

B.2 Shifting order-disorder phase transition

We notice in Figure 3.5 that Case Study 2b) exhibits a shifting order-disorder phase transition in the phase diagram. Here we have taken an asymmetric bottlebrush at $f_A \approx 0.141$ with the same architecture as Figure 3.5. We keep all parameters other than $b_{sc,B}$ fixed, and we observe the order-disorder phase transition shifts as the statistical segment of the chain length increases. This shows that increasing conformation asymmetry between the side chains shifts the order-disorder transition boundary.

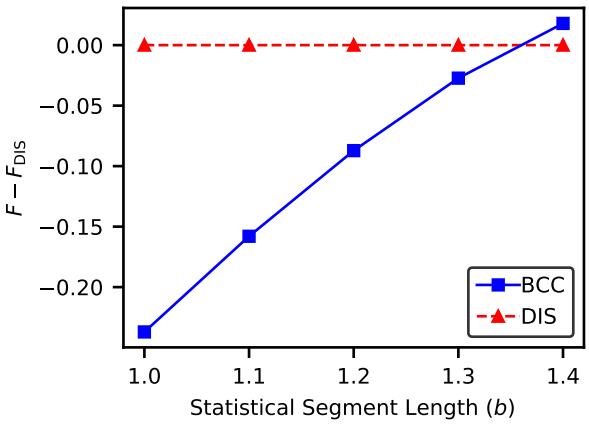

Figure B.1: Free energy of $f_A \approx 0.141$ with varying statistical segment length of BCC and DIS

Bibliography

[1] Glenn H. Fredrickson. *The Equilibrium Theory of Inhomogeneous Polymers*. International series of monographs on physics (Oxford, England) ; 134. Clarendon Press, Oxford; New York, 2006.

[2] Glenn H. Fredrickson and Kris T. Delaney. Field-theoretic simulations: An emerging tool for probing soft material assembly. *MRS Bull.*, 43(5):371–378, 2018.

[3] S F Edwards. The statistical mechanics of polymers with excluded volume. *Proc. Phys. Soc., London*, 85(4):613–624, apr 1965.

[4] Ludwik Leibler. Theory of microphase separation in block copolymers. *Macromolecules*, 13(6):1602–1617, 1980.

[5] Alfredo Alexander-Katz, André G. Moreira, Scott W. Sides, and Glenn H. Fredrickson. Field-theoretic simulations of polymer solutions: Finite-size and discretization effects. *J. Chem. Phys.*, 122(1):014904, 2005.

[6] Zhen-Gang Wang. Fluctuation in electrolyte solutions: The self energy. *Phys. Rev. E*, 81:021501, Feb 2010.

[7] Michael C. Villet and Glenn H. Fredrickson. Efficient field-theoretic simulation of polymer solutions. *J. Chem. Phys.*, 141(22):224115, 2014.

[8] Eleni Panagiotou, Kris T. Delaney, and Glenn H. Fredrickson. Theoretical prediction of an isotropic to nematic phase transition in bottlebrush homopolymer melts. *The Journal of Chemical Physics*, 151(9):094901, 2019.

[9] Kris T. Delaney and Glenn H. Fredrickson. Recent developments in fully fluctuating field-theoretic simulations of polymer melts and solutions. *J. Phys. Chem. B*, 120(31):7615–7634, 2016. PMID: 27414265.

[10] Kris T. Delaney and Glenn H. Fredrickson. Theory of polyelectrolyte complexation–complex coacervates are self-coacervates. *J. Chem. Phys.*, 146(22):224902, 2017.

[11] Eugene Helfand. Theory of inhomogeneous polymers: Fundamentals of the gaussian randomwalk model. *The Journal of Chemical Physics*, 62(3):999–1005, 1975.

[12] K. M. Hong and J. Noolandi. Theory of inhomogeneous multicomponent polymer systems. *Macromolecules*, 14(3):727–736, 1981.

[13] M. W. Matsen and M. Schick. Stable and unstable phases of a diblock copolymer melt. *Phys. Rev. Lett.*, 72:2660–2663, Apr 1994.

[14] K. Ø. Rasmussen and G. Kalosakas. Improved numerical algorithm for exploring block copolymer mesophases. *J. Polym. Sci., Part B: Polym. Phys.*, 40(16):1777–1783, 2002.

[15] G. Tzeremes, K. Ø. Rasmussen, T. Lookman, and A. Saxena. Efficient computation of the structural phase behavior of block copolymers. *Phys. Rev. E*, 65:041806, Apr 2002.

[16] V Ganesan and G. H Fredrickson. Field-theoretic polymer simulations. *Europhys. Lett.*, 55(6):814–820, sep 2001.

[17] H. Ceniceros and G. Fredrickson. Numerical solution of polymer self-consistent field theory. *Multiscale Model. Simul.*, 2(3):452–474, 2004.

[18] R. B. Thompson, K. O/. Rasmussen, and T. Lookman. Improved convergence in block copolymer self-consistent field theory by anderson mixing. *J. Chem. Phys.*, 120(1):31–34, 2004.

[19] Eric W. Cochran, Carlos J. Garcia-Cervera, and Glenn H. Fredrickson. Stability of the gyroid phase in diblock copolymers at strong segregation. *Macromolecules*, 39(7):2449–2451, 2006.

[20] Amit Ranjan, Jian Qin, and David C. Morse. Linear response and stability of ordered phases of block copolymer melts. *Macromolecules*, 41(3):942–954, 2008.

[21] Erin M. Lennon, George O. Mohler, Hector D. Ceniceros, Carlos J. García-Cervera, and Glenn H. Fredrickson. Numerical solutions of the complex langevin equations in polymer field theory. *Multiscale Model. Simul.*, 6(4):1347–1370, 2008.

[22] M. W. Matsen. Fast and accurate scft calculations for periodic block-copolymer morphologies using the spectral method with anderson mixing. *Eur. Phys. J. E*, 30(4):361, 2009.

[23] Kai Jiang, Yunqing Huang, and Pingwen Zhang. Spectral method for exploring patterns of diblock copolymers. *J. Comput. Phys.*, 229(20):7796–7805, 2010.

[24] P. Stasiak and M. W. Matsen. Efficiency of pseudo-spectral algorithms with anderson mixing for the scft of periodic block-copolymer phases. *Eur. Phys. J. E*, 34(10):110, Oct 2011.

[25] Debra J. Audus, Kris T. Delaney, Hector D. Ceniceros, and Glenn H. Fredrickson. Comparison of pseudospectral algorithms for field-theoretic simulations of polymers. *Macromolecules*, 46(20):8383–8391, 2013.

[26] Dominik Düchs, Kris T. Delaney, and Glenn H. Fredrickson. A multi-species exchange model for fully fluctuating polymer field theory simulations. *J. Chem. Phys.*, 141(17):174103, 2014.

[27] Daan Frenkel and Berend Smit. *Understanding molecular simulation : from algorithms to applications*. Computational science series ; 1. Academic Press, San Diego, 2nd edition. edition, 2002.

[28] Mark W. Matsen and Thomas M. Beardsley. Field-theoretic simulations for block copolymer melts using the partial saddle-point approximation. *Polymers*, 13(15), 2021.

[29] Giorgio Parisi. On complex probabilities. *Physics Letters B*, 131(4):393–395, 1983.

[30] John R. Klauder and Sean Lee. Improved complex langevin method for (2+1)-dimensional lattices. *Phys. Rev. D*, 45:2101–2104, Mar 1992.

[31] Michael C. Villet and Glenn H. Fredrickson. Numerical coarse-graining of fluid field theories. *J. Chem. Phys.*, 132(3):034109, 2010.

[32] Gert Aarts, Frank A. James, Erhard Seiler, and Ion-Olimpiu Stamatescu. Adaptive stepsize and instabilities in complex langevin dynamics. *Physics Letters B*, 687(2):154, 2010.

[33] Nan Xie, Weihua Li, Feng Qiu, and An-Chang Shi. phase formed in conformationally asymmetric ab-type block copolymers. *ACS Macro Letters*, 3(9):906–910, 2014.

[34] Wenbo Jiang, Yicheng Qiang, Weihua Li, Feng Qiu, and An-Chang Shi. Effects of chain topology on the self-assembly of ab-type block copolymers. *Macromolecules*, 51(4):1529–1538, 2018.

[35] Yicheng Qiang, Weihua Li, and An-Chang Shi. Stabilizing phases of block copolymers with gigantic spheres via designed chain architectures. *ACS Macro Letters*, 9(5):668–673, 2020.

[36] M. Brett Runge and Ned B. Bowden. Synthesis of high molecular weight comb block copolymers and their assembly into ordered morphologies in the solid state. *Journal of the American Chemical Society*, 129(34):10551–10560, 2007. PMID: 17685524.

[37] Samuel J Dalsin, Thomas G Rions-Maehren, Marissa D Beam, Frank S Bates, Marc A Hillmyer, and Mark W Matsen. Bottlebrush block polymers: Quantitative theory and experiments. *ACS Nano*, 9(12):12233–12245, 2015.

[38] Alice B. Chang and Frank S. Bates. Impact of architectural asymmetry on frankkasper phase formation in block polymer melts. *ACS Nano*, 14(9):11463–11472, 2020. PMID: 32820895.

[39] Morgan W. Bates, Joshua Lequieu, Stephanie M. Barbon, Ronald M. Lewis, Kris T. Delaney, Athina Anastasaki, Craig J. Hawker, Glenn H. Fredrickson, and Christopher M. Bates. Stability of the a15 phase in diblock copolymer melts. *PNAS*, 116(27):13194, 2019.

[40] Scott T. Milner. Chain architecture and asymmetry in copolymer microphases. *Macromolecules*, 27(8):2333–2335, 1994.

[41] Ekaterina B. Zhulina, Sergei S. Sheiko, Andrey V. Dobrynin, and Oleg V. Borisov. Microphase segregation in the melts of bottlebrush block copolymers. *Macromolecules*, 53(7):2582, 2020.

[42] Xingkun Man, Kris T. Delaney, Michael C. Villet, Henri Orland, and Glenn H. Fredrickson. Coherent states formulation of polymer field theory. *J. Chem. Phys.*, 140(2):024905, 2014.

[43] Glenn H. Fredrickson and Kris T. Delaney. Coherent states field theory in supramolecular polymer physics. *J. Chem. Phys.*, 148(20):204904, 2018.

[44] Zoltan Mester, Aruna Mohan, and Glenn H. Fredrickson. Macro- and microphase separation in multifunctional supramolecular polymer networks. *Macromolecules*, 44(23):9411–9423, 2011.

[45] G Holden, N.R. Legge, R. Quirk, and H.E. Schroeder. *Thermoplastic elastomers*. Hanser Publishers ; Hanser/Gardner Publications, Munich ; New York : Cincinnati, 2nd ed.. edition, 1996.

[46] Jeffrey T. Koberstein, Irena Gancarz, and Thomas C. Clarke. The effects of morphological transitions on hydrogen bonding in polyurethanes: Preliminary results of simultaneous dscftir experiments. *Journal of Polymer Science Part B: Polymer Physics*, 24(11):2487–2498, 1986.

[47] W.P. Yang, C.W. Macosko, and S.T. Wellinghoff. Thermal degradation of urethanes based on 4,4-diphenylmethane diisocyanate and 1,4-butanediol (mdi/bdo). *Polymer*, 27(8):1235 – 1240, 1986.

[48] Darren J. Martin, Gordon F. Meijs, Pathiraja A. Gunatillake, Simon J. McCarthy, and Gordon M. Renwick. The effect of average soft segment length on morphology and properties of a series of polyurethane elastomers. ii. saxs-dsc annealing study. *Journal of Applied Polymer Science*, 64(4):803–817, 1997.

[49] Ivaylo Dimitrov, Barbara Trzebicka, Axel H.E. Mller, Andrzej Dworak, and Christo B. Tsvetanov. Thermosensitive water-soluble copolymers with doubly responsive reversibly interacting entities. *Progress in Polymer Science*, 32(11):1275 – 1343, 2007.

[50] Walter H. Stockmayer. Theory of molecular size distribution and gel formation in branchedchain polymers. *The Journal of Chemical Physics*, 11(2):45–55, 1943.

[51] Paul J. Flory. *Principles of polymer chemistry / Paul J. Flory.* The George Fisher Baker non-resident lectureship in chemistry at Cornell University. Cornell University Press, Ithaca, N.Y, 1953.

[52] Dietrich Stauffer, Antonio Coniglio, and Mireille Adam. Gelation and critical phenomena. In Karel Dušek, editor, *Polymer Networks*, pages 103–158, Berlin, Heidelberg, 1982. Springer Berlin Heidelberg.

[53] Glenn H. Fredrickson. Dynamics and rheology of inhomogeneous polymeric fluids: A complex langevin approach. *The Journal of Chemical Physics*, 117(14):6810–6820, 2002.

[54] Pierre-Gilles de Gennes. *Scaling concepts in polymer physics / Pierre-Gilles de Gennes.* Cornell University Press, Ithaca, N.Y, 1979.

[55] S F Edwards. The theory of polymer solutions at intermediate concentration. *Proc. Phys. Soc., London*, 88(2):265–280, jun 1966.

[56] F Schmid. Self-consistent-field theories for complex fluids. *J. Phys.: Condens. Matter*, 10(37):8105–8138, sep 1998.

[57] M W Matsen. The standard gaussian model for block copolymer melts. *J. Phys.: Condens. Matter*, 14(2):R21–R47, dec 2001.

[58] An-Chang Shi. Self-consistent field theory of inhomogeneous polymeric systems: A variational derivation. *Adv. Theory Simul.*, 2(4):1800188, 2019.

[59] Glenn H. Fredrickson, Venkat Ganesan, and Franois Drolet. Field-theoretic computer simulation methods for polymers and complex fluids. *Macromolecules*, 35(1):16–39, 2002.

[60] Douglas J. Grzetic, Kris T. Delaney, and Glenn H. Fredrickson. Field-theoretic study of salt-induced order and disorder in a polarizable diblock copolymer. *ACS Macro Lett.*, 8(8):962–967, 2019.

[61] T. M. Beardsley and M. W. Matsen. Fluctuation correction for the order-disorder transition of diblock copolymer melts. *J. Chem. Phys.*, 154(12):124902, 2021.

[62] Yuri O. Popov, Jonghoon Lee, and Glenn H. Fredrickson. Field-theoretic simulations of polyelectrolyte complexation. *J. of Polym. Sci. B: Polym. Phys.*, 45(24):3223, 2007.

[63] Jonghoon Lee, Yuri O. Popov, and Glenn H. Fredrickson. Complex coacervation: A field theoretic simulation study of polyelectrolyte complexation. *J. Chem. Phys.*, 128(22):224908, 2008.

[64] Dominik Düchs, Venkat Ganesan, Glenn H. Fredrickson, and Friederike Schmid. Fluctuation effects in ternary ab + a + b polymeric emulsions. *Macromolecules*, 36(24):9237, 2003.

[65] Bart Vorselaars, Russell K. W. Spencer, and Mark W. Matsen. Instability of the microemulsion channel in block copolymer-homopolymer blends. *Phys. Rev. Lett.*, 125:117801, Sep 2020.

[66] Russell K. W. Spencer and Mark W. Matsen. Coexistence of polymeric microemulsion with homopolymer-rich phases. *Macromolecules*, 54(3):1329, 2021.

[67] Yi-Xin Liu, Kris T. Delaney, and Glenn H. Fredrickson. Field-theoretic simulations of fluctuation-stabilized aperiodic bricks-and-mortar mesophase in miktoarm star block copolymer/homopolymer blends. *Macromolecules*, 50(16):6263, 2017.

[68] M. W. Matsen and R. B. Thompson. Equilibrium behavior of symmetric aba triblock copolymer melts. *J. Chem. Phys.*, 111(15):7139–7146, 1999.

[69] Akash Arora, Jian Qin, David C. Morse, Kris T. Delaney, Glenn H. Fredrickson, Frank S. Bates, and Kevin D. Dorfman. Broadly accessible self-consistent field theory for block polymer materials discovery. *Macromolecules*, 49(13):4675–4690, 2016.

[70] Daniel L. Vigil, Carlos J. Garca-Cervera, Kris T. Delaney, and Glenn H. Fredrickson. Linear scaling self-consistent field theory with spectral contour accuracy. *ACS Macro Letters*, 8(11):1402–1406, 2019.

[71] Alfredo Alexander-Katz and Glenn H. Fredrickson. Diblock copolymer thin films: A field-theoretic simulation study. *Macromolecules*, 40(11):4075–4087, 2007.

[72] P. Stasiak and M. W. Matsen. Monte carlo field-theoretic simulations for melts of symmetric diblock copolymer. *Macromolecules*, 46(19):8037–8045, 2013.

[73] T. M. Beardsley, R. K. W. Spencer, and M. W. Matsen. Computationally efficient field-theoretic simulations for block copolymer melts. *Macromolecules*, 52(22):8840–8848, 2019.

[74] M. W. Matsen. Field theoretic approach for block polymer melts: Scft and fts. *J. Chem. Phys.*, 152(11):110901, 2020.

[75] S.M. Cox and P.C. Matthews. Exponential time differencing for stiff systems. *J. Comput. Phys.*, 176(2):430 – 455, 2002.

[76] W. P. Petersen. A general implicit splitting for stabilizing numerical simulations of itô stochastic differential equations. *SIAM J. Numer. Anal.*, 35(4):1439–1451, 1998.

[77] Kris T. Delaney and Glenn H. Fredrickson. Polymer field-theory simulations on graphics processing units. *Comput. Phys. Commun.*, 184(9):2102–2110, 2013.

[78] François Drolet and Glenn H. Fredrickson. Combinatorial screening of complex block copolymer assembly with self-consistent field theory. *Phys. Rev. Lett.*, 83:4317–4320, Nov 1999.

[79] Zuojun Guo, Guojie Zhang, Feng Qiu, Hongdong Zhang, Yuliang Yang, and An-Chang Shi. Discovering ordered phases of block copolymers: New results from a generic fourier-space approach. *Phys. Rev. Lett.*, 101:028301, Jul 2008.

[80] Weiquan Xu, Kai Jiang, Pingwen Zhang, and An-Chang Shi. A strategy to explore stable and metastable ordered phases of block copolymers. *J. Phys. Chem. B*, 117(17):5296–5305, 2013. PMID: 23551204.

[81] Yu-Chieh Hsu, Ching-I Huang, Weihua Li, Feng Qiu, and An-Chang Shi. Micellization of linear a-b-(b-alt-c)n multiblock terpolymers in a-selective solvents. *Polymer*, 54(1):431–439, 2013.

[82] Gregory M. Grason, B. A. DiDonna, and Randall D. Kamien. Geometric theory of diblock copolymer phases. *Phys. Rev. Lett.*, 91:058304, Jul 2003.

[83] Sangwoo Lee, Michael J. Bluemle, and Frank S. Bates. Discovery of a frank-kasper sigma phase in sphere-forming block copolymer melts. *Science*, 330(6002):349–353, 2010.

[84] Adam E Levi, Joshua Lequieu, Jacob D Horne, Morgan W Bates, Jing M Ren, Kris T Delaney, Glenn H Fredrickson, and Christopher M Bates. Miktoarm stars via grafting-through copolymerization: Self-assembly and the star-to-bottlebrush transition. *Macromolecules*, 52(4):1794–1802, 2019.

[85] Jarosław Paturej, Sergei S. Sheiko, Sergey Panyukov, and Michael Rubinstein. Molecular structure of bottlebrush polymers in melts. *Science Advances*, 2(11), 2016.

[86] Peter D. Olmsted and Scott T. Milner. Strong-segregation theory of bicontinuous phases in block copolymers. *Phys. Rev. Lett.*, 72:936–939, Feb 1994.

[87] Peter D. Olmsted and Scott T. Milner. Strong-segregation theory of bicontinuous phases in block copolymers. *Phys. Rev. Lett.*, 74:829–829, Jan 1995.

[88] A. E. Likhtman and A. N. Semenov. Theory of microphase separation in block copolymer/homopolymer mixtures. *Macromolecules*, 30(23):7273–7278, 1997.

[89] William FM Daniel, Joanna Burdyńska, Mohammad Vatankhah-Varnoosfaderani, Krzysztof Matyjaszewski, Jarosław Paturej, Michael Rubinstein, Andrey V Dobrynin, and Sergei S Sheiko. Solvent-free, supersoft and superelastic bottlebrush melts and networks. *Nature Materials*, 15(2):183–189, 2016.

[90] M. W. Matsen. Effect of architecture on the phase behavior of ab-type block copolymer melts. *Macromolecules*, 45(4):2161, 2012.

[91] M. Doi and S.F. Edwards. *The theory of polymer dynamics*. International series of monographs on physics ; 73. Oxford University Press, 1986.

[92] Joshua Lequieu, Timothy Quah, Kris T Delaney, and Glenn H Fredrickson. Complete photonic band gaps with nonfrustrated abc bottlebrush block polymers. *ACS Macro Letters*, 9(7):1074–1080, 2020.

[93] Jean-Louis Barrat, Glenn H. Fredrickson, and Scott W. Sides. Introducing variable cell shape methods in field theory simulations of polymers. *The Journal of Physical Chemistry B*, 109(14):6694–6700, 2005. PMID: 16851752.

[94] L. J. Fetters, D. J. Lohse, D. Richter, T. A. Witten, and A. Zirkel. Connection between polymer molecular weight, density, chain dimensions, and melt viscoelastic properties. *Macromolecules*, 27(17):4639–4647, 1994.

[95] Glenn H. Fredrickson, Andrea J. Liu, and Frank S. Bates. Entropic corrections to the flory-huggins theory of polymer blends: Architectural and conformational effects. *Macromolecules*, 27(9):2503–2511, 1994.

[96] K. Kim, A. Arora, R. M. Lewis, M. Liu, W. Li, A.-C. Shi, K. D. Dorfman, and F. S. Bates. Origins of low-symmetry phases in asymmetric diblock copolymer melts. *Proc. Natl. Acad. Sci. U. S. A.*, 115:847–854, 2018.

[97] K. Kim, M. W. Schulze, A. Arora, R. M. Lewis, A. Hillmyer, K. D. Dorfman, and F. S. Bates. Thermal processing of diblock copolymer melts mimics metallurgy. *Science*, 356:520–523, 2017.

[98] M. Liu, W. Li, F. Qiu, and A.-C. Shi. Stability of the frank-kasper σ-phase in *babc* linear tetrablock terpolymers. *Soft Matter*, 12:6412–6421, 2016.

[99] Heyi Liang, Zhen Cao, Zilu Wang, Sergei S. Sheiko, and Andrey V. Dobrynin. Combs and bottlebrushes in a melt. *Macromolecules*, 50(8):3430–3437, 2017.

[100] Ying Jiang and Jeff Z. Y. Chen. Self-consistent field theory and numerical scheme for calculating the phase diagram of wormlike diblock copolymers. *Phys. Rev. E*, 88:042603, Oct 2013.

[101] Daniel L. Vigil, Kris T. Delaney, and Glenn H. Fredrickson. Quantitative comparison of field-update algorithms for polymer scft and fts. *Macromolecules*, 2021.

[102] Hector D. Ceniceros. Efficient order-adaptive methods for polymer self-consistent field theory. *J. Comput. Phys.*, 386:9–21, 2019.

[103] Sam F. Edwards and Karl F. Freed. Cross linkage problems of polymers i. the method of second quantization applied to the cross linkage problem of polymers. *J. Phys. C: Solid State Phys.*, 3(4):739, 1970.

[104] Akash Arora, David C. Morse, Frank S. Bates, and Kevin D. Dorfman. Accelerating self-consistent field theory of block polymers in a variable unit cell. *J. Chem. Phys.*, 146(24):244902, 2017.

[105] David Gottlieb and Steven A. Orszag. *Numerical Analysis of Spectral Methods : Theory and Applications*. Regional conference series in applied mathematics ; 26. Society for Industrial and Applied Mathematics, Philadelphia, 1977.

[106] C. W. Clenshaw and A. R. Curtis. A method for numerical integration on an automatic computer. *Numerische Mathematik*, 2(1):197–205, Dec 1960.

[107] Maurice L. Huggins. Solutions of long chain compounds. *The Journal of Chemical Physics*, 9(5):440–440, 1941.

[108] Paul J. Flory. Thermodynamics of high polymer solutions. *The Journal of Chemical Physics*, 10(1):51–61, 1942.

[109] Weichao Shi, Andrew L. Hamilton, Kris T. Delaney, Glenn H. Fredrickson, Edward J. Kramer, Christos Ntaras, Apostolos Avgeropoulos, Nathaniel A. Lynd, Quentin Demassieux, and Costantino Creton. Aperiodic bricks and mortar mesophase: a new equilibrium state of soft matter and application as a stiff thermoplastic elastomer. *Macromolecules*, 48(15):5378–5384, 2015.

[110] Tyler S Harmon, Alex S Holehouse, Michael K Rosen, and Rohit V Pappu. Intrinsically disordered linkers determine the interplay between phase separation and gelation in multivalent proteins. *eLife*, 6:e30294, nov 2017.

[111] T. P. Russell, R. Jerome, P. Charlier, and M. Foucart. The microstructure of block copolymers formed via ionic interactions. *Macromolecules*, 21(6):1709–1717, 1988.

[112] J. Huh, H.J. Park, K.H. Kim, K.H. Kim, C. Park, and W.H. Jo. Giant thermal tunability of the lamellar spacing in block-copolymer-like supramolecules formed from binary-end-functionalized polymer blends. *Adv. Mater.*, 18(5):624, 2006.

[113] Kathleen E. Feldman, Matthew J. Kade, E. W. Meijer, Craig J. Hawker, and Edward J. Kramer. Phase behavior of complementary multiply hydrogen bonded end-functional polymer blends. *Macromolecules*, 43(11):5121–5127, 2010.

[114] Wayne C. Yount, David M. Loveless, and Stephen L. Craig. Small-molecule dynamics and mechanisms underlying the macroscopic mechanical properties of coordinatively cross-linked polymer networks. *J. Am. Chem. Soc.*, 127(41):14488, 2005. PMID: 16218645.

[115] J Ruokolainen, R Mkinen, M Torkkeli, T Makela, R Serimaa, G ten Brinke, O Ikkala, and R Makinen. Switching supramolecular polymeric materials with multiple length scales. *Science*, 280(5363):557, 1998.

[116] Philippe Cordier, Franois Tournilhac, Corinne Souli-Ziakovic, and Ludwik Leibler. Self-healing and thermoreversible rubber from supramolecular assembly. *Nature*, 451(7181):977–980, 2008.

[117] June Huh and Won Ho Jo. Theory on phase behavior of triblocklike supramolecules formed from reversibly associating end-functionalized polymer blends. *Macromolecules*, 37(8):3037–3048, 2004.

[118] Edward H. Feng, Won Bo Lee, and Glenn H. Fredrickson. Supramolecular diblock copolymers: a field-theoretic model and mean-field solution. *Macromolecules*, 40(3):693–702, 2007.

[119] Won Bo Lee, Richard Elliott, Kirill Katsov, and Glenn H. Fredrickson. Phase morphologies in reversibly bonding supramolecular triblock copolymer blends. *Macromolecules*, 40(23):8445–8454, 2007.

[120] R. Elliott and Glenn H. Fredrickson. Supramolecular assembly in telechelic polymer blends. *The Journal of Chemical Physics*, 131(14):144906, 2009.

[121] Aruna Mohan, Richard Elliot, and Glenn H. Fredrickson. Field-theoretic model of inhomogeneous supramolecular polymer networks and gels. *The Journal of Chemical Physics*, 133(17):174903, 2010.

[122] Daniel J Amit. *Field Theory, The Renormalization Group and Critical Phenomena*. WORLD SCIENTIFIC, 2nd edition, 1993.

[123] Glenn H. Fredrickson and Kris T. Delaney. Direct free energy evaluation of classical and quantum many-body systems via field-theoretic simulation. *Proceedings of the National Academy of Sciences*, 119(18):e2201804119, 2022.

[124] Athanassios Z. Panagiotopoulos. Direct determination of phase coexistence properties of fluids by monte carlo simulation in a new ensemble. *Molecular Physics*, 61(4):813–826, 1987.

[125] A.Z. Panagiotopoulos, N. Quirke, M. Stapleton, and D.J. Tildesley. Phase equilibria by simulation in the gibbs ensemble. *Molecular Physics*, 63(4):527–545, 1988.

[126] Robert A. Riggleman and Glenn H. Fredrickson. Field-theoretic simulations in the gibbs ensemble. *The Journal of Chemical Physics*, 132(2):024104, 2010.

[127] Zoltan Mester, Nathaniel A. Lynd, and Glenn H. Fredrickson. Numerical self-consistent field theory of multicomponent polymer blends in the gibbs ensemble. *Soft Matter*, 9:11288–11294, 2013.

[128] Zoltan Mester, Nathaniel A. Lynd, Kris T. Delaney, and Glenn H. Fredrickson. Phase coexistence calculations of reversibly bonded block copolymers: A unit cell gibbs ensemble approach. *Macromolecules*, 47(5):1865–1874, 2014.

[129] M. W. Matsen. Phase behavior of block copolymer/homopolymer blends. *Macromolecules*, 28(17):5765–5773, 1995.

[130] W. Helfrich. Steric interaction of fluid membranes in multilayer systems. *Zeitschrift fr Naturforschung A*, 33(3):305–315, 1978.

[131] S. Milner and D. Roux. Flory theory of the unbinding transition. *Journal de Physique I*, 2(9):1741–1754, 1992.

[132] Daniel Broseta and Glenn H. Fredrickson. Phase equilibria in copolymer/homopolymer ternary blends: Molecular weight effects. *The Journal of Chemical Physics*, 93(4):2927–2938, 1990.

[133] M. W. Matsen. New fast scft algorithm applied to binary diblock copolymer/homopolymer blends. *Macromolecules*, 36(25):9647–9657, 2003.

[134] Katsuhiko Iwasaki, Akira Hirao, and Seiichi Nakahama. Morphology of blends of .alpha.,.omega.-diaminopolystyrene with .alpha.,.omega.-dicarboxypoly(ethylene oxide). *Macromolecules*, 26(8):2126–2131, 1993.

[135] Longhe Zhang, Lauren R. Kucera, Subramanyam Ummadisetty, Jacob R. Nykaza, Yossef A. Elabd, Robson F. Storey, Kevin A. Cavicchi, and R. A. Weiss. Supramolecular multiblock polystyrenepolyisobutylene copolymers via ionic interactions. *Macromolecules*, 47(13):4387–4396, 2014.

[136] Alejandro Güillen Obando, Yuwei Chen, and Zhe Qiang. A simple route to prepare supramolecular block copolymers using telechelic polystyrene/polydimethylsiloxane pairs. *Polymer International*, 71(4):470–477, 2022.

[137] Wolfgang H. Binder, Michael J. Kunz, and Elisabeth Ingolic. Supramolecular poly(ether ketone)polyisobutylene pseudo-block copolymers. *Journal of Polymer Science Part A: Polymer Chemistry*, 42(1):162–172, 2004.

[138] Adam Gooch, Chinemelum Nedolisa, Kelly A. Houton, Christopher I. Lindsay, Alberto Saiani, and Andrew J. Wilson. Tunable self-assembled elastomers using triply hydrogen-bonded arrays. *Macromolecules*, 45(11):4723–4729, 2012.

[139] T. C. Lubensky and Joel Isaacson. Field theory for the statistics of branched polymers, gelation, and vulcanization. *Phys. Rev. Lett.*, 41:829–832, Sep 1978.

[140] T. C. Lubensky and Joel Isaacson. Statistics of lattice animals and dilute branched polymers. *Phys. Rev. A*, 20:2130–2146, Nov 1979.

[141] Sergei Panyukov and Yitzhak Rabin. Statistical physics of polymer gels. *Physics Reports*, 269(1):1–131, 1996.

[142] Mehran Kardar. *Statistical Physics of Fields*. Cambridge University Press, 2007.